Alexandre Nuno Pereira Lopes

Master of Science in Physics

Multiple Source Photothermal Therapy with External Contrast Agents for the Treatment of Breast Cancer: A Viability Study

Thesis submitted in partial fulfilment
of the requirements for the degree of

Doctor of Philosophy in
Physics Engineering

Adviser:	José Paulo Moreira dos Santos, Full Professor, NOVA University Lisbon
Co-adviser:	Pedro Manuel Cardoso Vieira, Assistant Professor, NOVA University Lisbon

Examination Committee

Chair:	Maria Adelaide de Almeida Pedro de Jesus, Full Professor, FCT-NOVA
Rapporteurs:	António Miguel Lino Santos Morgado, Assistant Professor, University of Coimbra
	Manuel Adler Sanchez de Abreu, Invited Auxiliary Researcher, University of Lisbon
Members:	José Paulo Moreira dos Santos, Full Professor, FCT-NOVA
	João Manuel Rendeiro Cardoso, Assistant Professor, FCT-NOVA
	Paulo António Martins Ferreira Ribeiro, Assistant Professor, FCT-NOVA

FACULDADE DE
CIÊNCIAS E TECNOLOGIA
UNIVERSIDADE NOVA DE LISBOA

December, 2020

Alexandre Nuno Pereira Lopes

Master of Science in Physics

Multiple Source Photothermal Therapy with External Contrast Agents for the Treatment of Breast Cancer: A Viability Study

Thesis submitted in partial fulfilment
of the requirements for the degree of

Doctor of Philosophy in
Physics Engineering

Adviser:	José Paulo Moreira dos Santos, Full Professor, NOVA University Lisbon
Co-adviser:	Pedro Manuel Cardoso Vieira, Assistant Professor, NOVA University Lisbon

Examination Committee

Chair:	Maria Adelaide de Almeida Pedro de Jesus, Full Professor, FCT-NOVA
Rapporteurs:	António Miguel Lino Santos Morgado, Assistant Professor, University of Coimbra
	Manuel Adler Sanchez de Abreu, Invited Auxiliary Researcher, University of Lisbon
Members:	José Paulo Moreira dos Santos, Full Professor, FCT-NOVA
	João Manuel Rendeiro Cardoso, Assistant Professor, FCT-NOVA
	Paulo António Martins Ferreira Ribeiro, Assistant Professor, FCT-NOVA

FACULDADE DE
CIÊNCIAS E TECNOLOGIA
UNIVERSIDADE NOVA DE LISBOA

December, 2020

Multiple Source Photothermal Therapy with External Contrast Agents for the Treatment of Breast Cancer: A Viability Study

This document was created using the (pdf)LaTeX processor, based on the "novathesis" template[1], developed at the Dep. Informática of FCT-NOVA [2].
[1] https://github.com/joaomlourenco/novathesis [2] http://www.di.fct.unl.pt

Dedicado ao meu avô, ao meu pai, ao meu irmão e ao meu filho.

Acknowledgements

A lista de pessoas e instituições às quais quero agradecer é longa dado todo o percurso e às várias colaborações que me levaram até à conclusão deste projeto.

Em primeiro lugar queria agradecer aos meus orientadores, o Professor José Paulo Santos e Professor Pedro Vieira, por todo o apoio que me deram e pela oportunidade única que tive para trabalhar neste projeto. Foram instrumentais em todo o caminho desde 2015 quando os conheci, pelas conversas e troca de experiências tanto a nível profissional como a nível pessoal. Sem eles este trabalho não tinha acontecido. Muito obrigado!

Queria também agradecer à Fundação para a Ciência e Tecnologia pelo apoio financeiro que foi dado através do projeto DAEPHYS que me permitiu prosseguir e concluir este estudo científico.

Queria também agradecer aos amigos e companheiros de trabalho que fiz enquanto estive na Universidade Nova de Lisboa, à Ana Gabriel pela amizade primeiro, e também por todo o apoio que me deu na preparação dos fantomas e da sua caracterização, que foram cruciais para todo este trabalho. Ao Jorge, Luís, Patrícia, David, Pedro. Ao senhor Faustino, e à Ana Maria e à Luiza dos serviços de secretariado. Ao Pedro Morais e ao Rui Almeida um grande abraço!

Gostaria de agradecer ao pessoal do Laboratório de Ótica, Lasers e Sistemas, nomeadamente ao professor João Coelho, ao Ricardo Gomes, à Marta Castiñeras, ao Fernando Monteiro e ao David Alves, pela ajuda muito importante na caracterização dos fantomas e nas discussões de onde pudemos obter o protocolo mais adequado para a preparação das propriedades óticas dos fantomas e realização das experiências.

À professora Catarina Reis e à Joana Lopes da Faculdade de Farmácia da Universidade de Lisboa, por terem fornecido as nanopartículas que possibilitaram a realização deste trabalho.

I also would like to acknowledge Professor Simon Arridge and Dr Martin Schweiger at the University College of London for all the support, hospitality, and precious knowledge they shared to my work on the numerical simulation of photothermal experiments. It was invaluable. Additionally, I would like to thank Bjoern Eiben for our valuable discussions and support for my work, and all the guys at CMIC with whom I had the privilege to know.

Queria agradecer à minha orientadora de licenciatura e mestrado da Faculdade de

Ciências da Universidade de Lisboa, Doutora Helena Santos, por todo o apoio que me deu ao longo de quase meia década e pela confiança que me deu para iniciar o doutoramento. Obrigado!

Queria agradecer também a toda a malta do IGC fez ou faz parte do meu percurso desde que lá cheguei, em especial a todos do grupo dos esfomeados! Deste grupo há duas pessoas que se destacam pela positiva no apoio ao meu trabalho que desenvolvi para a Tese: o Gabriel Martins e o Zé Marques. Obrigado!

Aos meus amigos do Norte e do Sul, em especial ao: Zé, Bruno, Vera, Miguel, Eliana, Luís Pinto, Ana, Ornelas, David, Catarina, Agostinha... Amigos são para sempre, e apesar de não estar com alguns de vós há já algum tempo pelo confinamento, guardo por vocês todos um carinho muito especial.

À minha família: em especial à minha Mãe e Pai, Ana, Jorge e Daniela, Carolina, Francisca; vocês são imprescindíveis. À minha família *adotiva*: Odete, Aníbal, Cristina, Pedro, Margarida, Sílvia, Luís e Guilherme. Obrigado pelo vosso apoio!

Por fim, queria também agradecer à Alexandra e ao Artur. Este trabalho não teria acontecido sem vocês e o vosso apoio.

Muito obrigado!

"A model is a lie
that helps you see the truth."
– Howard Skipper

Abstract

In this thesis, photothermal therapy is assessed as a treatment for tumours deep inside the breast using near-infrared light and high absorbing external contrast agents, which deliver the heat damage at the desired location. With the advent of light-absorbing nanoparticles, there is a promising alternative to conventional breast cancer therapies limiting the damage given to healthy tissue at the skin surface and enhancing the thermal damage in cancer cells. There are some known limitations to this therapy, one of the most important being the strong attenuation of light in biological tissue. Several authors reported at best conflicting views on the therapy, with some claiming that indeed it is possible performing it successfully up to a few centimetres. In contrast, other authors claim that only at the surface these can be employed. The therapy's success depends on the optical properties and concentration of nanoparticles at the tumour location, but, to my knowledge, there were no definitive studies that effectively tackle this issue from the optics point of view. Hence, the studies developed in this thesis are in the pursuit of this issue. Three protocols were developed; one to measure the optical properties of tissue, another to produce optical phantoms with specific optical properties, and a numerical simulation protocol to further the therapy's effectiveness and possibly help design devices and treatment protocols.

Several experiments have been developed to validate these protocols, and their results have been compared with others already published. An INO® optical phantom with known absorption and scattering coefficients was characterized by two experimental setups: one developed by the company and another developed in this project. The results of these two characterisations were compared to validate the protocol to measure optical properties. The developed setup provides a reasonable estimate for the scattering properties with an associated uncertainty of 7%, while the company's associated uncertainty was at 2%. Regarding the absorption setup measurement apparatus, the uncertainty was in the same order of magnitude as the measured value for the developed apparatus. The company's apparatus also revealed a comparable uncertainty, thus, enhancing the difficulty of measuring such small absorption coefficient' values.

An optical phantom with a 9 mm thick inclusion placed at 5 mm from the surface was produced, and a photothermal experiment was conducted on it to test the other

protocols. Its irradiation lasted about 12 minutes. A thermocouple was placed at the interface between the inclusion and the phantom for temperature measuring. Two optical numerical models were implemented in this study, Monte Carlo and the diffusion approximation, coupled with the classical heat diffusion equation to estimate the temperature and compare with the experimental data. The Monte Carlo simulations outperformed the diffusion approximation. The average percentage difference of the Monte Carlo and diffusion approximation results compared to the experimental data was 4.5% and 61%. The Pearson correlation coefficient between these models' results and the experimental data was 0.98 and 0.95, respectively. Additionally, the Monte Carlo and diffusion approximation numerical models' radial profile studies indicated an adequate distribution of the former compared to what was expected from other studies.

Once the protocol of the numerical simulation was validated, a more realistic simulation was conducted where a compressed breast geometry was considered with the addition of skin, blood flow and a tumour 1 cm below the surface. A phantom with breast, skin and blood flow properties coupled to the bioheat transfer equation was still not studied in the community, to my knowledge. Additionally, several numerical irradiating schemes were considered to enhance the absorption of light in depth. The breast tissue was irradiated for two minutes in all of the irradiation schemes. The temperature in the skin was high enough to produce damage, but the temperature increase at the tumour was only 1 ^{o}C. This result contrasts clearly with other studies that show that at a depth of 2 centimetres, a temperature increase of at least 15 ^{o}C can be achieved at 60 seconds of illumination. One can conclude that photothermal therapy is indeed a treatment very sensitive to breast optical properties. Other solutions have to be considered for breast tissue of average optical properties to increase the effectiveness of in-depth photothermal therapy using light-absorbing nanoparticles.

Keywords: Photothermal therapy, hyperthermia, diffusion approximation,
Monte Carlo, gold nanoparticles, numerical protocols, thermal therapy, laser-induced thermal therapy

Resumo

Nesta tese, a terapia fototérmica é estudada em tumores no interior da mama usando luz no infravermelho próximo e agentes de contraste externos de alta absorção, que geram dano térmico no local desejado. Com a descoberta destas nanopartículas, há uma alternativa promissora às terapias convencionais para o tratamento do cancro de mama, limitando o dano causado ao tecido saudável na superfície da pele, aumentando o dano térmico nas células cancerígenas. Existem algumas limitações conhecidas para esta terapia, sendo uma das mais importantes a forte atenuação da luz no tecido biológico. Alguns autores retratam pontos de vista díspares sobre este tipo de terapia, afirmando que, de fato, é possível realizá-la com algum sucesso a poucos centímetros. Por outro lado, outros autores afirmam que apenas na superfície eles podem ser empregues com sucesso. O sucesso da terapia depende das propriedades ópticas do tecido e da concentração de nanopartículas no local do tumor, mas, no meu conhecimento, não existem estudos definitivos que abordem efetivamente essa questão do ponto de vista da óptica. Assim, os estudos desenvolvidos nesta dissertação exploram este tema. Três protocolos foram desenvolvidos; um para medir as propriedades ópticas do tecido, outro para produzir fantomas com propriedades ópticas específicas e um protocolo de modelação numérica para estudar o aumento da eficácia da terapia e possivelmente ajudar a desenhar dispositivos e formular protocolos terapêuticos.

Foram desenvolvidas várias experiências para validar esses protocolos e os seus resultados foram comparados com outros já publicados. Um fantoma óptico INO® com coeficientes de absorção e dispersão conhecidos foi caracterizado por dois aparatos experimentais: um desenvolvido pela empresa que o fabricou e outro desenvolvido neste projeto. Os resultados dos dois aparatos experimentais foram comparados para validar o protocolo da determinação de propriedades ópticas aqui reportado. O aparato experimental para determinar o coeficiente de dispersão desenvolvido neste projeto fornece uma estimativa razoável com uma incerteza associada de 7%, enquanto a incerteza associada determinada pelo aparato da empresa é 2%. A incerteza experimental do aparato desenvolvido para a medição do coeficiente de absorção é da mesma ordem de grandeza que o valor medido. A incerteza experimental reportada pela empresa também se revela comparável ao valor medido, o que por um lado expõe a dificuldade de medir pequenos

valores relativos ao coeficiente de absorção.

Um fantoma ótico foi produzido com uma região de alta absorção que tem uma espessura de 9 mm e que se situava a 5 mm de profundidade. O tratamento fototérmico foi aplicado a este fantoma por forma a testar os restantes protocolos. O período de irradiação durou 12 minutos. Um termopar foi colocado na interface entre a região de interesse e o fantoma para registar a temperatura. Para simular esta terapia foram considerados dois modelos numéricos. O Monte Carlo e aproximação de difusão retratavam separadamente a propagação da luz no tecido, que depois serviam como dados de entrada para a equação clássica de transferência de calor para calcular a temperatura de cada um dos modelos por forma a serem comparadas com as medições experimentais. Quando comparados com os dados experimentais, os resultados das simulações geradas por Monte Carlo superam os da aproximação de difusão. A diferença média percentual de Monte Carlo e a aproximação de difusão, comparados com os dados experimentais foram de 4.5% e de 61%, respectivamente. Foi calculado o coeficiente de correlação de Pearson entre os resultados computacionais dos dois modelos e os resultados experimentais e resultaram em 0.98 e 0.95, respectivamente. Foram também estudados os perfis radiais destes dois modelos computacionais. Estes mostraram que Monte Carlo gerava distribuições de energia adequados às distribuições de outros resultados já publicados.

Uma vez validado o protocolo de modelação numérica, foi desenvolvido um modelo mais realista onde o modelo de uma mama comprimida foi considerado que tinha no seu centro um tumor com nanopartículas com um centímetro de diâmetro. Neste fantoma também foram consideradas as propriedades adequadas de tecido mamário, juntamente com a inclusão da pele, circulação sanguínea e a equação de transferência de calor para tecidos biológicos. No meu conhecimento, estas considerações ainda não tinham sido estudadas pela comunidade. Vários aparatos de irradiação foram considerados por forma a testar o aumento de calor gerado pelas nanopartículas presentes no tumor. O tempo de irradiação foi dois minutos em todos. Pôde observar-se que a temperatura à superfície da pele era suficiente para gerar dano térmico mas o aumento de temperatura registado no tumor foi 1 ^{o}C. Este resultado contrasta claramente com outros estudos que mostram que a uma distância de dois centímetros se pode gerar um aumento de temperatura de 15 ^{o}C após 60 segundos de irradiação. Pôde concluir-se que este tratamento é muito sensível às propriedades óticas do tecido. Terão de ser consideradas outras soluções por forma a aumentar a eficácia deste tratamento em profundidade para o tratamento do cancro da mama.

Palavras-chave: Terapia fototérmica, hipertermia, aproximação de difusão, Monte Carlo, nanopartículas de ouro, protocolo numérico, terapia térmica, terapia térmica induzida por laser

Contents

List of Figures

List of Tables

Chapter 1

Introduction

Breast cancer is the most common type of cancer diagnosed in women worldwide (Organization 2015). The number of European women with this diagnosis was estimated as 464 thousand in 2013, and 131 thousand deceased due to the disease (Ferlay *et al.* 2013). The number of cases seems to have increased in 2018. According to Ferlay *et al.* (2018), around 523 thousand European women were diagnosed with breast cancer, 138 thousand deceased. These cases represent 28.2% of female cancer new occurrences and 16% of female death caused by cancer. The combined results imply almost a stagnation of this disease in Europe after the steep increase registered in the last decades (ECIS 2019). Therefore, breast cancer continues to present itself as a disease with a high impact on public health (Caplan 2014).

In a clinical frame of reference, breast cancer is not a single disease but can be categorised according to several histological, molecular, and functional status (Dai *et al.* 2015; Malhotra *et al.* 2010). Once its categorisation is defined, the oncologist may choose between different treatments to heal cancer patients. The knowledge and development areas to handle this disease are therapy, screening technology, palliative care, and prevention. Hence, a clinical strategy can be tailored specifically to each patient according to all four knowledge areas' diagnostic specificities. On the therapy side, the most common treatments are surgery, radiotherapy, hormone therapy, thermotherapy, cryotherapy or chemotherapy. A combination of these therapies may also be considered to increase treatment outcome.

Most of the currently applied therapies have significant disadvantages to the patient's health. Despite having high efficacy against cancer, unwanted outcomes such as (i) metastasis resulting from the surgical procedure, (ii) skin cancer, (iii) hair loss, (iv) overweight, (v) non-specific targeting to tumour cells, (vi) lack of appetite, – among many other – are typical unwelcome effects of such treatments (Alphandéry 2014).

Photothermal therapy (PTT) using near-infrared light is considered a viable and healthy alternative to these therapies in specific types of cancer (Abadeer and Murphy 2016). This therapy uses non-ionising (non-carcinogenic) radiation and is characterised by having low toxicity levels and high sensitivity, probing to almost all tissue molecules such as haemoglobin, lipids, water and other chromophores and external contrast agents. On the diagnosis side, near-infrared light allows for functional and metabolic imaging. In photothermal therapy, a higher intensity of this light is used, and a fraction of it is absorbed and converted into heat, which in turn can destroy malignant tissue through processes like coagulation or hyperthermia if the achieved temperature and time of exposure conditions at that site are met (Brunetaud *et al.* 1995). The tissues' natural optical attenuation is a limiting factor in this treatment since it makes light diffuse its way into the tissue. Hence, the higher the distance from the source to the tumour, the lower the light intensity and, consequently, fewer photons are converted into heat to destroy cancer cells. This attenuation of light imposes restrictions, and that is why this type of therapy is currently only being applied to treat skin cancer, in interstitial photothermal treatments or combined with other therapies(Abadeer and Murphy 2016; Hirsch *et al.* 2003; Jaque *et al.* 2014; Sajjadi *et al.* 2013).

With the advent of gold nanoparticles (GNP) in medicine, there is a promising opportunity to bypass this limitation. Their wavelength-tunable high absorbing properties make them optimal tools to increase the effectiveness of this therapy in depth. Some studies suggest that deep photothermal therapy aided with nanoparticles can be a viable alternative to breast cancer's typical treatments, but its effectiveness has not been tested to a full extent. Although it is reported to be limited up to a few centimetres (Cho *et al.* 2010; Hirsch *et al.* 2003), other studies suggest that this limit can be overcome by tailoring the therapy to the cancer properties (Baetke *et al.* 2015; Elliott *et al.* 2007; Reynoso *et al.* 2013).

This work aims to provide a proof-of-concept study to assess the viability of using photothermal therapy to fight breast cancer away from the skin surface, considering an optics standpoint. It includes using numerical methods to tailor the specific needs of the therapy, evaluate the appropriate parameters, including nanoparticle's density, number of sources, source power, and apply them using different methods to increase its effectiveness, especially deep inside tissue. Ultimately, it is hoped that photothermal therapy can be used to treat breast tumours in-depth to some degree, damaging the surrounding healthy tissue minimally and in combination with other techniques to reduce the need for more aggressive treatments and enhance the chance to obtain a positive outcome.

1.1 Contributions

The main contributions presented in this thesis are:

- The development of a protocol to simulate a multiple-source photothermal therapy. This protocol considers two different mathematical models to determine the fluence rate. It can use either Monte Carlo simulations or diffusion approximation and feed these results in the bioheat equation to determine the temperature and estimated damaged tissue.
- The development of a protocol to measure the optical properties of scattered dominated biological tissues. The attenuation and absorption coefficients are determined considering optically thin samples. A comparison performance test was made with an optical calibration phantom.
- The development of a protocol to produce a phantom that would mimic breast optical and thermal properties. This protocol focuses more on estimating the produced phantom's optical properties correctly since thermal properties do not change so much photothermal therapy's effectiveness as the former ones.

The work produced in this thesis has already contributed to the scientific community with a peer-reviewed original article (Lopes *et al.* 2019) and a conference paper (Lopes *et al.* 2016), which work was presented at that conference.

1.2 Thesis Outline

The remainder of this thesis is presented as follows. In chapter 2, an overview of the current state of the art in photothermal therapy is presented. Here, a brief introduction to the interaction between photons and tissue is presented, along with the most representative studies developed of in-depth photothermal experiments and numerical models using nanoparticles. Chapter 3 is divided into three main topics. The first of those describes a setup to determine some optical properties of biological tissue. The second presents a brief introduction to the production of optical phantoms and their characterisation. The third main topic is the simulation software used in this thesis. Chapter 4 presents a study to validate the therapy with numerical simulations and explore some methods to increase this therapy's effectiveness tailored to a specific diagnostic. Chapter 5 concludes this thesis.

Chapter 2

Background and State of the Art

chapter overview This chapter presents the theoretical background of optics and thermal properties and reviews the relevant literature on photothermal therapy covered in this thesis. It begins with a brief review on light-matter interaction, highlighting effects that matter produces on light due to the optical properties of tissue, and outlines radiative transport theory. An introduction to the matter-light interaction mechanisms, tissue damage control and a review in bioheat transfer follows. The last section will present nanoparticle-aided photothermal therapy's state of the art in three steps. First, the need to use external contrast agents as heat generators that increase the heat generation rate in a predefined region of interest is shown. Second, some light properties bypass, to some extent, the limitations of light attenuation deep inside tissue are presented. Third, the results on numerical methods of nanoparticle-aided photothermal therapy and the most representative studies and recent results in this subject are outlined and discussed.

2.1 Light-Matter Interactions

When light impinges on biological matter, two types of interaction categories can be distinguished and depicted by the effects that matter has on light and the effects that light has on matter. These are electromagnetic interactions between individual photons and electrons modelled by quantum physics and, to some extent, classical electrodynamics. Considering the effects that matter induces on light, at a macroscopic scale, these interactions between electrons and photons result in measurable quantities which depict the average interactions of a beam of photons *interacting* with a block of matter, by *e.g.*, scattering or absorption. This section will begin with an outline of refraction, reflection, scattering and absorption and their respective measurable attributes. The radiative transport equation, which considers light propagation on a macroscopic scale in biological tissue, follows.

2.1.1 Reflectance, Refraction and Transmittance

The interactions between visible and near-infrared light impinge unto biological matter are reflection, refraction, scattering and absorption.

Reflectance is a measurement of light intensity reflected from an object that usually has the same angle as the angle of incidence. Only a small fraction of light usually gets reflected and this light's fraction is dependent on the optical intensity, the refractive index and angle of incidence between the beam axis and the object's surface (Bohren and Huffman 1983).

A significant fraction of the light is not reflected and is refracted inside the object, usually moving in another slightly different direction if the two mediums' refractive index is different. The refractive index is considered a manifestation of scattering by the many molecules that comprise that medium. Mathematically, it can be represented by $n \equiv n' + in''$, where the real part of the refractive index n' determines the phase velocity $v = c/n'$, the imaginary part governs the wave attenuation as it propagates through the tissue, and c is the light speed. It is also proportional to the absorption coefficient: $\mu_a = 4\pi n''/\lambda$, λ being the photon's wavelength (Bohren and Huffman 1983).

In biomedical optics, the refractive index is proportional to the water content present in the tissue to a first approximation:

$$n' = n'_{dry} - (n'_{dry} - n'_{water})W \tag{2.1}$$

where W is a percentage of the water content of the tissue, $n'_{water} = 1.33$ is the waters' refractive index, and $n'_{dry} = 1.514$ is the refractive index of dry biological tissue. The values presented here were determined using several biological human tissue samples (Jacques 2013).

Transmittance T is the ratio of transmitted light intensity I [W] to the incident light intensity I_0 [W] through a sample, *i.e.*, the fraction that did not interact with it and is

defined as (Bohren and Huffman 1983):

$$T = \frac{I}{I_0} \tag{2.2}$$

Transmittance, reflectance, and refraction of light can be modelled by the Fresnel equations, although the latter is difficult to observe and measure in biological tissue due to scattering centres in tissue (Bohren and Huffman 1983).

2.1.2 Optical Scattering and Anisotropy

Elastic scattering of light is a process by which photons interact with particles of different refractive indices, changing their direction of propagation while maintaining their intrinsic energy (*i.e.*, wavelength). These particles are also known as scattering centres. Depending on the particles' size and the wavelength of the impinging photons, one can describe the scattering phenomena with different properties. Usually, this results in a relation between the scattering direction and the light intensity, which can be modelled by Rayleigh scattering if the photon's wavelength is larger than the particles' size or governed by Mie scattering if the wavelength is comparable or smaller. Mie scattering is the most common when considering the interaction between light in the near-infrared range of the electromagnetic spectrum from 0.7 to 0.9 μm and biological soft tissue. It leads to scattering of light, which is characterised by a predominant forward scattering anisotropy. Some of the leading causes of this scattering in soft tissue are the density of lipid membranes in cells, collagen fibres, the size of nuclei, or hydration status in the tissue. The size of these molecules can range from 0.1 μm to 10 μm (Gratton and Fantini 2007; Jacques 1996).

Three parameters can describe the scattering properties of tissues: (1) the scattering coefficient μ_s [mm^{-1}], which is defined as the inverse of the average photon path length between two successive scattering events; (2) the scattering phase function $\Theta(\theta) \equiv \Theta(\vec{s}, \vec{s'})$ which determines the angular distribution of scattered light intensity from the propagating direction $\vec{s}$ to $\vec{s'}$; and (3) the average cosine of the scattering angle θ, the so-called scattering anisotropy which is defined as (Binzoni *et al.* 2006; Gratton and Fantini 2007)

$$g \equiv \langle \cos\theta \rangle = \int_{4\pi} \Theta(\vec{s}, \vec{s'})(\vec{s}, \vec{s'}) d\omega \tag{2.3}$$

where $\Theta(\vec{s}, \vec{s'})d\omega$ is the probability of a photon incident from the $\vec{s}$ direction will leave in the $\vec{s'}$ direction of the differential unit of solid angle $d\omega$. Thus, the scattering anisotropy $g \in$ [-1,1] provides a measurement of the dominance of scattering direction. For breast tissue g >0.94 in the visible and near-infrared region of the light spectrum (Jacques 2013).

The Henyey-Greenstein phase function (Binzoni *et al.* 2006; Henyey and Greenstein 1941) is a theoretical phase function which, in particular, describes the scattering anisotropy in biological tissue and is based on many experimental observations of many biological samples, and is given by (Binzoni *et al.* 2006):

$$\Theta(\theta) = \frac{1-g^2}{(1+g^2-2g\cos\theta)^{3/2}} \tag{2.4}$$

Some numerical models consider one scattering parameter that contains the essence of the three parameters already described, namely the reduced scattering coefficient μ_s' [mm^{-1}] that is defined as:

$$\mu_s' = \mu_s(1-g) \tag{2.5}$$

Conceptually, the reduced scattering coefficient is defined as the inverse of the average distance between two virtually isotropic scattering events. This definition relies on the assumption that many forward scattered collisions are the same as a single isotropic scattering (Alerstam 2011; Gratton and Fantini 2007).

The reduced scattering coefficient is used in biomedical optics since it follows an empirical dependency of a power law, described by (Jacques 2013):

$$\mu_s' = a\left(f_{Ray}\left(\frac{\lambda}{500(nm)}\right)^{-4} + (1-f_{Ray})\left(\frac{\lambda}{500(nm)}\right)^{-b_{Mie}}\right) \tag{2.6}$$

This equation considers parameters from Rayleigh and Mie scatterings defined by the factor f_{Ray}, a is a nameless factor, b_{Mie} is the Mie scattering power and λ the photons wavelength. These coefficients change depending on the actual composition of each particular breast (*e.g.*, fattier versus fibrous tissue). The scattering coefficients provide an averaged measure of the size, shape and concentration of the scattering centres of the tissue.

2.1.3 Absorption

If the energy of an interacting photon on a molecule is the same as the energy transition between two quantum states of that molecule, an absorption event may occur. This absorbed photonic energy will be converted in one of three forms: a higher electronic, a rotational or a vibrational state. Macroscopically, a light-absorbing medium absorbs a fraction of impinging light. In a non-scattering tissue, this is measured by the absorption coefficient and is defined as (Jacques 2013):

$$\mu_a = -\frac{1}{T}\frac{\partial T}{\partial L} \tag{2.7}$$

where μ_a [mm^{-1}] is the so-called absorption coefficient, ∂T [W] is the transmitted fraction of the incoming light that travels an infinitesimal pathlength ∂L [mm]. In this particular non-scattering case, the Beer-Lambert law (Giacometti and Diamond 2013) can be defined as $T = \exp^{-\mu_a L}$.

For samples with more than one absorbing compound, the absorption coefficient can have an alternative expression: $\mu_a = \sum_i \epsilon_i C_i$, where ϵ_i and C_i are the specific absorption coefficient [$mm^{-1}M^{-1}$] and the concentration [M] of the ith absorbing compound in

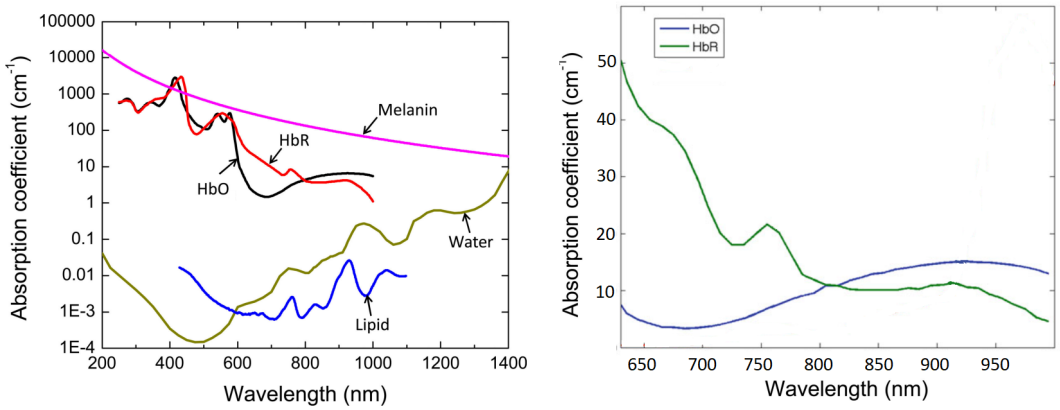

Figure 2.1: Absorption coefficient as a function of wavelength for some of the chromophores present in biological tissue at their typical concentrations. On the left plot, the Oxyhaemoglobins' absorption coefficient is shown in black, in red is the deoxyhaemoglobins', in magenta is the melanin, and the waters' absorption coefficient of comparable concentration in tissue is shown in marine-green. On the right plot, the Haemoglobin's absorption coefficient is presented in a normal scale. The first biological optical window is considered the region between 650 nm and 950 nm, where light is the least absorbed. Taken from Xia *et al.* (2014).

the sample, respectively. Thus, the absorption coefficient provides information on the concentration of tissue chromophores (Jaque *et al.* 2014).

Absorption in biological tissues is mainly caused by water molecules or macromolecules such as proteins and pigments. Figure 2.1 presents the absorption coefficient as a function of the photons' wavelength for the chromophores with the largest absorption coefficient in the visible and near-infrared region of the electromagnetic spectrum. On the left side, they are shown on a logarithmic scale, and on the right side, the two most significant absorbers in breast tissue are presented on a linear scale. The melanin absorption is not shown in this second plot as it solely resides in the skin and not inside the breast tissue. These endogenous contrast agents are presented in their respective concentrations in biological matter. Herein, one also can identify the so-called biological windows of therapy characterized as the wavelength range in the electromagnetic spectrum, where the absorption from haemoglobin and water is minimal. The first biological window lies between the visible red (650 nm) and the near-infrared (950 nm) part of the spectrum, and the second in the near-infrared between 1000 and 1250 nm (Xia *et al.* 2014).

For reference, Table 2.1 shows the average optical properties of normal and tumour breast tissue measured at 785 nm.

2.1.4 Radiative Transfer Equation

The light inside biological tissue refracts between two different n mediums, scatters and is absorbed. There are several quantities to measure the light *quantity* at any given place or time. The radiance $\phi_r(\vec{r},\vec{s},t)$ [W m^{-2}sr^{-1}] describes the power per unit area and per

Table 2.1: Average optical properties of the tumour and background tissues for three cases examined at 785 nm. Retrieved from Jiang *et al.* (2002)

	Background		Tumour	
	μ_a (mm^{-1})	μ_s' (mm^{-1})	μ_a (mm^{-1})	μ_s' (mm^{-1})
Case 1	0.0093	0.75	0.016	1.02
Case 2	0.0072	1.07	0.013	1.33
Case 3	0.011	1.02	0.021	0.68

steradian flowing in direction $\vec{s}$ in the position $\vec{r}$ at a time t. The quantity of light per unit area inside tissue is defined as the fluence rate $\phi(\vec{r},t)$ [W mm^{-2}]. The relation between these two quantities is $\phi(\vec{r},t) = \int \phi_r(\vec{r},\vec{s},t)d\vec{s'}$.

The radiative transfer equation is phenomenological at its essence since it is premised on energy conservation and is used to model the radiance $\phi_r(\vec{r},t)$ [W m^{-2}sr^{-1}] using the optical properties of tissue already presented. This equation is given by (Chandrasekhar 1960):

$$\Big(\frac{1}{c}\frac{\partial}{\partial t} + \vec{s}\cdot\vec{\nabla} + \mu_t(\vec{r})\Big)\phi_r(\vec{r},\vec{s},t) = \mu_s(\vec{r})\int_{4\pi}\Theta(\vec{s}\cdot\vec{s'})\phi_r(\vec{r},\vec{s},t)d\vec{s'} + q(\vec{r},\vec{s},t) \tag{2.8}$$

where $\vec{r}$ represents the position vector, $\vec{s}$ represents the directional unit vector, $\mu_t(\vec{r})$ the attenuation coefficient defined by $\mu_t(\vec{r}) = \mu_s(\vec{r}) + \mu_a(\vec{r})$ [mm^{-1}], $\Theta(\vec{s}\cdot\vec{s'})$ represents the normalized phase function, and $q(\vec{r},\vec{s},t)$ [W mm^{-3}sr^{-1}] is the light source term.

On the right side of equation 2.8, the first term accounts for the changing radiance over time, the second term accounts for the radiance exiting and entering a small volume from the tissue, and the third term accounts for the loss in radiance due to the tissue's attenuation. On the right side of the equation, the first term accounts for a change in radiance due to a change of direction by scattering light (from direction $\vec{s'}$ into $\vec{s}$), and the second term accounts for a light source present inside that elemental volume (Chandrasekhar 1960).

Green's function theory can provide an analytical solution for the radiative transfer equation to elementary homogeneous geometries (Arridge 1999). Numerical models are needed to provide a solution for the radiative transfer equation for 3D heterogeneous biological samples. There are many models to choose from, and the next list will highlight some of the most used (Alerstam 2011; Arridge 1999):

- Discrete Ordinates
- Spherical Harmonics (P_n)
- Diffusion Theory
- Monte Carlo

Discrete Ordinates' Method The method of discrete ordinates is a numerical method to directly solve the radiative transfer equation using a system of equations, discretizing not only the XYZ-domain but also the scattering term as (Guo and Kumar 2002):

$$\mu_s(\vec{r}) \int_{4\pi} \Theta(\vec{s}\cdot\vec{s}')\phi_r(\vec{r},\vec{s},t)d\vec{s}' = \sum_{j=1}^{n} w_j \Theta(\vec{s}\cdot\vec{s}')\phi(\vec{r},\vec{s},t) \tag{2.9}$$

where w_j are weighting coefficients for direction vectors.

This method is only recently being tackled in 3D as it consumes too much memory solving the system of ordinary differential equations traditionally. One way to slightly decrease memory dependence is to iteratively increase the angular discretization, making the solution iteratively dependent (Guo and Kumar 2002).

Spherical Harmonics Method - P_n This model considers an expansion of some terms of the radiative transfer equation as an expansion series of spherical harmonics truncated at the n-th order (*i.e.*, the scattering phase function, light source and radiance terms). If $n \to \infty$, the method would provide an exact solution to the radiative transfer equation. This method is computationally expensive since it has to solve a system of equations based on the chosen n-th terms and the space discretization (Alerstam 2011; Aydin *et al.* 2004).

Diffusion Approximation Method The diffusion approximation, or P_1 approximation, can be obtained considering the first approximation of the radiative transfer equation in spherical harmonics (Arridge 1999) (i.e. $n = 1$). If one considers a constant wave light source, then this equation is written as:

$$-\vec{\nabla}\cdot\vec{\kappa}(\vec{r})\vec{\nabla}\phi(\vec{r}) + \mu_a(\vec{r})\phi(\vec{r}) = 0, \vec{r} \in \Omega, \tag{2.10}$$

where $\vec{\kappa}(\vec{r}) = 1/(3(\mu_s'(\vec{r}) + \mu_a(\vec{r}))$ [mm^{-1}] is the diffusion coefficient, $\phi(\vec{r})$ the fluence rate [W mm^{-2}] and Ω its domain(Schweiger *et al.* 2014).

The diffusion approximation is derived under some premises, which lead to the following restrictions: it is only valid in high scattering tissues ($\mu_s \gg 1$), the condition $\mu_a/\mu_s \to 0$ must always be valid, the solutions of these equations are only valid away from the light source, and the optical properties cannot change dramatically from the surrounding regions (Alerstam 2011; Arridge 1999; Aydin *et al.* 2004). Nonetheless, the diffusion approximation is one of the most considered in modelling radiative transfer in biological tissue since it satisfies all of these requisites and is numerically inexpensive (Arridge 1999; Arridge and Schotland 2009; Gibson *et al.* 2005).

Monte Carlo Method The Monte Carlo method is a numerical method that consists of solving the radiative transfer equation by stochastically tracing fictional photon packets or particles through the medium.

Randomized numbers will be attributed to each photon packet, given one probability density functions to each potential scattering interaction property (*e.g.*, scattering probability, a new direction of propagation, or distance travelled). The photon packet will decrease in its weight with the travelled distance using the Beer-Lambert law, and if the packet is less than a predefined number, this photon packet is discarded. The density of such photon packets $N(\vec{r},\vec{s},t)$ [$\text{mm}^{-3}\text{sr}^{-1}$] has a direct relation to radiance (Alerstam 2011):

$$N(\vec{r},\vec{s},t) = \frac{\phi_r(\vec{r},\vec{s},t)}{E\lambda} \tag{2.11}$$

where E [W] is the power per packet and λ [mm^{-1}] the photons' wavelength. A simulation of an infinite number of these particles would generate a particle density which would be an exact solution to the radiative transfer equation (Alerstam 2011; Fang 2010).

The main disadvantage of this numerical method is the time considered to perform the simulation. Considering the same computer hardware (CPU, RAM, hard drive and GPU), the significant bottleneck is the simulation software, the number of photons, and the problem's geometry. To develop a numerical solution of the problem, one can take from a few seconds, if the program is developed to run on a general-purpose graphics card unit, to a few days if it runs only on one CPU (Fang 2010; Fang and Boas 2009a; Glaser *et al.* 2013; Wang *et al.* 1995). Moreover, a computer with better specifications would also decrease the simulation time.

2.2 Matter-Light Interactions

Biological tissue will also be affected by the light-matter interaction, especially by the absorption of light, which may cause a significant change in the tissue's properties. These effects will be addressed in the interaction mechanism's subsection, where special attention is dedicated to thermal therapy and thermal damage. This section is followed by an introduction to heat propagation and damage in biological tissue.

2.2.1 Interaction Mechanisms

The absorption of visible or near-infrared light will result in higher vibrational, rotational or electronic states. If one considers a short light pulse that impinges totally on an absorbing homogeneous object and no heat diffusion is regarded, then the temperature rise is proportional to the total energy absorbed and is defined as (Walsh 2010):

$$\rho c \Delta T = \mu_a H \tag{2.12}$$

where ΔT [K] is the temperature change, H [J mm^{-2}] the radiant exposure (*i.e.*, the total light energy that was impinged on the tissue), ρ [Kg mm^{-3}] the tissue density and c [J $\text{Kg}^{-1}\text{K}^{-1}$] is heat capacity.

Depending on each of these parameters' choice, many different types of interaction mechanisms can be observed at a macroscopic scale, as Figure 2.2 suggests. As can be seen, the radiant energy of these interactions has an extensive range of approximately 1 Jcm^{-2} to 10^3 Jcm^{-2}. Hence, to select a specific interaction mechanism, one must first consider the laser and a target time exposure (Niemz 1996; Sajjadi *et al.* 2013).

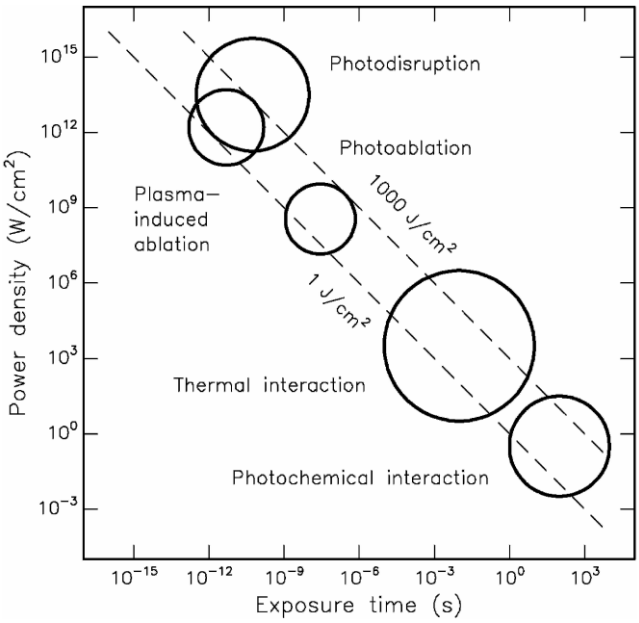

Figure 2.2: Map of laser-tissue interactions. The circles suggest what laser parameters are to be used to attain such an interaction mechanism. Taken from Niemz (1996).

Photochemical interactions happen when the photon acts as a reagent to produce chemical reactions and releases free radicals within macromolecules or tissues. These are limited to the region of photon absorption, usually defined as the optical zone. Biostimulation and photodynamic therapy are based on this interaction mechanism (Jacques 1993; Niemz 1996).

The photothermal interaction will be discussed in more detail in the next subsection due to its importance to the thesis' context.

Photoablation relies on using high-energy ultra-violet photons to break the molecular bonds, removing tissue by a rapid expansion of irradiated volume and ejection of tissue debris (Sajjadi *et al.* 2013).

Photodisruption and plasma-induced ablation are associated with the so-called optical breakdown, characterized by a nonlinear absorption of light. In these interaction mechanisms, the absorption coefficient is a function of the laser intensity. Thus, equation 2.12 is no longer valid in these higher power density mechanisms.

In a plasma-induced ablation, a cascade of free electrons caused by a torrent ionization forms a plasma with other ions, removing targeted tissue in a non-thermal way. The surrounding tissue remains free of mechanical or thermal damage. With even higher

energies than plasma-induced ablation, shock waves and other mechanical effects become dominant, fragmenting and cutting tissue.

Photodisruption is a mechanical interaction that may happen during a plasma-mediated ablation due to extreme laser intensity, leading to bubble formation and shock wave generation (Sajjadi *et al.* 2013).

2.2.1.1 Photothermal Interaction Mechanism

The photothermal interaction mechanism involves thermally induced effects, which can extend beyond the region of light absorption. Once the photonic energy is absorbed and converted into thermal energy, the thermalization process occurs. In this process, the vibrational/rotational energy of the excited molecule is transferred to other molecules as translational kinetic energy, a process also known as thermal diffusion (Jacques 1992).

The photothermal interaction mechanism may lead to thermal tissue damage, depending on the temperature achieved and tissue exposure to that temperature. Figure 2.3 shows a qualitative dependence on reversible and irreversible damage as a function of temperature and the duration of temperature (Niemz 1996).

However, from a clinical perspective, each stage of temperature achieved and exposure time leads to different types of thermal damage from a histologic point of view. Assuming an average body temperature of 37^{o}C and trending up in the temperature scale, the first categorized thermal therapy is defined as *diathermia*, and temperature ranges from 37^{o}C up to 41^{o}C. In this range of temperatures, the modifications at a cellular level are not significant to cause irreversible damage but end up being a beneficial heating treatment where blood flows and ion diffusion rates across cellular membranes increase.

The next class of thermal treatment is called *hyperthermia*. This thermal therapy is usually applied in combination with other cancer treatments, such as radiation and chemotherapy. The temperature ranges from approximately 41 to 48 ^{o}C, and if the time of exposure is adequate, molecular conformational changes occur, as well as protein denaturation and their de-aggregation, leading to irreversible tissue injuries. From a histologic point of view, while the thermal damage is irreversible, there is no visible effect on the tissue (Jacques 1992). This study aims to work within this temperature range. Due to the relevance of this temperature range, it is also usual to associate the parameter *cumulative equivalent minutes* CEM_{43} as an estimate induced stress by the thermal load of tissue at, *e.g.*, 43 ^{o}C. Different tissues have different responses to thermal load. Skin tolerates more than CEM_{43} = 40 min, fatty tissues' limit is on the CEM_{43} = 15 min (Murbach *et al.* 2014). Hence the objective would be to give thermal damage to the tumour and not to the skin, which in principle could be a challenge due to the melanin absorption spectra, as shown in figure 2.1.

Irreversible injury treatments are attained much faster when the temperature of the tumour exceeds 48 ^{o}C for a few minutes since this is when coagulative necrosis processes happen.

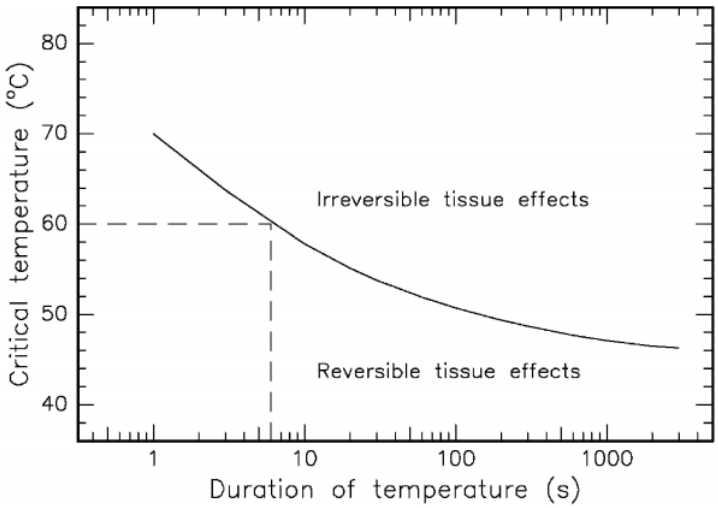

Figure 2.3: Critical temperatures for the occurrence of cell necrosis presented as a function of exposure to that temperature. Taken from Niemz (1996).

Above 60 ^{o}C, irreversible and almost instantaneous *protein denaturation* take place. This treatment often results in brown colour to tissue, similar to cooked meat in the target area (McKenzie 1990).

There are other thermal categories defined above this temperature threshold. However, the limit is defined up to this point since the target temperature is at 45 ^{o}C. The interested reader is referred to Sajjadi *et al.* (2013), and references cited therein.

2.2.2 Bioheat Transfer

In biological tissue, heat transfer is a complex process because biological bodies can regulate themselves or change the temperature if necessary. Moreover, bioheat transfer can happen at many scales, depending on the heat quantity: at a microscopic scale between particles and molecules, at a mesoscopic scale between tissues and organs, and at a macroscopic scale between the body and its surroundings. The heat propagates itself in tissues *passively* through conduction, convection or radiation heat transfer mechanisms, but also *actively* regulating or changing the temperature by varying the blood flow using its intricate network of veins, arteries and capillaries; varying its metabolic heat rate by regulating its cellular activities, and making use of its dynamic optical and thermal properties (Bhowmik *et al.* 2013).

At a macroscopic level, the photonic energy absorbed by impinging visible or near-infrared light on biological tissue is stored in two ways: increasing the temperature locally or/and matter phase change (Reynoso 2011; Welch and Van Gemert 2011).

There are many models to determine how heat propagates within the tissue. They can be categorized under continuous or vascular models. The vascular models are complex forms of bioheat equations that try to account for the individual blood flow in each vessel.

The continuum models assume a blood flow average over each control volume (Bhowmik *et al.* 2013; Minkowycz *et al.* 2009).

The most used model in biomedicine is the bioheat transfer equation. It is a continuum bioheat equation that describes the heat propagation inside biological tissue (Bhowmik *et al.* 2013; Pennes 1998) and is defined as:

$$\begin{aligned}\rho(\vec{r})c(\vec{r})\frac{\partial T(\vec{r},t)}{\partial t} =& \nabla\cdot\Big(k(\vec{r})\nabla T(\vec{r},t)\Big) + \omega_b(\vec{r})\rho_b(\vec{r})c_b(\vec{r})\Big(T(\vec{r},t) - T_a(\vec{r})\Big) \\ &+ Q_m(\vec{r}) + Q(\vec{r},t), \vec{r}\in\Omega,\end{aligned} \tag{2.13}$$

where $\rho(\vec{r})$ [Kg mm^{-3}] is the tissue density, $c(\vec{r})$ [W K^{-1}Kg^{-1}] is the specific heat, $T(\mathbf{r},t)$ [K] the temperature, $k(\mathbf{r})$ [W mm^{-1}K^{-1}] the thermal conductivity, $Q_m(\vec{r})$ [W mm^{-3}] metabolic heat rate, $\omega_b(\vec{r})$ [s^{-1}] rate of blood perfusion, $\rho_b(\vec{r})$ [Kg mm^{-3}] density of blood, $c_b(\vec{r})$ [W K^{-1}Kg^{-1}] blood's specific heat, $T_a(\vec{r})$ [K] body's temperature, and $Q(\vec{r},t)$ [W mm^{-3}] the rate of heat generation induced by laser radiation, also known as the volumetric heat source. This term is defined by (Reynoso 2011; Welch *et al.* 2010):

$$Q(\vec{r},t) = \mu_a(\vec{r})\times\phi(\vec{r},t) \tag{2.14}$$

where $\phi(\vec{r},t)$ [W mm^{-2}] is the fluence rate.

The first three terms in equation 2.13 represent the temporal change in temperature shown on the left side, the thermal diffusion, and the blood perfusion terms shown on the right side of this equation.

The bioheat transfer equation is simple in its approach and has been the subject of many research studies (Bhowmik *et al.* 2013). Some of this model's limitations include blood flow, vascular geometry averaged in the blood perfusion term, or the interdependence of heat transfer on many scales. The full limitations of this model are detailed in Bhowmik *et al.* 2013. Nonetheless, it provides reliable results for soft tissue (Mukundakrishnan *et al.* 2009).

Evaporation heat transfer has an important role in biological tissue (Sturesson 1998; Valvano 2010) but is often not considered for non-biological tissues (Elliott *et al.* 2007; Jaunich *et al.* 2008; Reynoso *et al.* 2013).

2.2.2.1 Convective Heat Transfer

The convective heat transfer mechanism is also considered a means of dissipating the heat from the tissue's surface to other mediums of different thermal properties, including its surrounding environment. It is governed by Newton's law of cooling, which is defined as:

$$Q_c(\vec{m},t) = h(T_\infty - T(\vec{m},t)), \vec{m}\in\partial\Omega, \tag{2.15}$$

where h [W mm^{-2}K^{-1}] is the convective heat transfer coefficient, T_∞ [K] is the room temperature, and $\vec{m}$ is the vector position belonging to the domain's border $\partial\Omega$ (Diller 2010).

Thermal Properties Temperature Dependence To a first approximation, biological tissue is like a homogeneous solid with thermal properties dependent on its water percentage. It is crucial to have biological models that do account for the loss or transport of water. To a secondary degree, water thermal properties increase with temperature. Thus it is essential to consider the temperature dependence of the tissue thermal properties (Valvano 2010).

2.2.3 Damage stage

From figure 2.3, one can estimate the thermal tissue damage by the temperature and the duration at which it remains at that temperature for thermal damage to be irreversible. Thus, only the temporal and spatial distribution of heat would be needed to estimate the tissue's damage and measure the therapy's effectiveness. The irreversible types can have an immediate effect and are regarded as direct thermal effects or can happen after the heating event. Secondary thermal effects happen after the heating treatment is done and through a complex process that leads to cell death. Therefore, to correctly measure the thermal effects either by immediate effects or secondary effects, one would have to wait a few days to ensure all cells undergo apoptosis (Thomsen and Pearce 2010).

To determine tissue necrosis (Θ) when the temperature exceeds the hyperthermia damage temperature ($T_{d,h}$) for more than a certain period ($t_{d,h}$), it is considered the following parameter

$$\Theta = \frac{1}{t_{d,h}} \int_0^\tau \epsilon_{d,h} dt \tag{2.16}$$

where,

$$\epsilon_{d,h} = \begin{cases} 1 & \text{if } T > T_{d,h} \\ 0 & \text{otherwise} \end{cases} \tag{2.17}$$

Here Θ represents a dimensionless parameter and is 0 if the temperature is below $T_{d,h}$ and 1 if the temperature exceeded $T_{d,h}$ by $t_{d,h}$ seconds.

With this parameter, one can estimate the level of damage given by direct thermal effects and make direct comparisons with histologic results to increase the reliability of the numerical model (Thomsen and Pearce 2010).

2.3 Nanoparticle-aided Photothermal Therapy

Photothermal therapy using visible or near-infrared light has been considered a nonreliable technique to perform in-depth tumour treatments since biological tissues have

strong attenuation, limiting photothermal treatments to superficial tumours. With the advent of nanoparticles, it is possible to circumvent these limitations due to the nanoparticles' following properties and functionalities (Abadeer and Murphy 2016; Jaque *et al.* 2014):

- *High absorption:* By providing a large heat rate conversion efficiency, making thermal therapy with low-power lasers possible.
- *Tunability:* Optically tunable particles are developed to have large absorption cross-sections in a chosen wavelength, preferentially in the biological windows, so that tissue absorbs the radiation minimally.
- *Low toxicity:* By having non-toxicity levels which render them inert to cells when deprived of optical radiation.
- *Good Solubility:* The majority of these particles have good solubility in biocompatible liquids, allowing them long circulation times in the bloodstream.
- *Active targeting:* Some nanoparticles are produced with coatings to give them biocompatibility or/and coated with antibodies recognised explicitly by proteins present in the malignant cells.
- *Passive targeting:* Capitalizing on the enhanced permeability and retention effect, which exploits the abnormalities of tumour vasculature, nanoparticles can be developed to accumulate around tumours naturally.

At the nanoparticles' production, one can manipulate these properties to make them ideal candidates to perform localized treatments, increase the treatments' efficiency, damage malignant cells, and reduce the damage level to healthy tissue. However, this circumvent on the therapy's limitations is not unbounded (Cho *et al.* 2010; Qin and Bischof 2012).

The laser wavelength for photothermal therapy using nanoparticles is chosen usually in the first biological window because most nanoparticles have an operation range on that window (Jaque *et al.* 2014).

Qin and Bischof (2012) present a review of several studies on nanoparticle research and temperature change, the size target and the necessary continuous wave (CW) laser power to reach the desired temperature increase. The nanoparticles' concentration is assumed to be 5 μg/g ($\sim 1.83 \times 10^{10}$ nanoparticles/ml). This value can be achieved by systemic delivery. To get a temperature increase of 10 ^{o}C: for a target size of 0.1 mm, the total number of nanoparticles would be 10^3 and the irradiance 2.5×10^4 W cm^{-2}; for a 1 mm target size, the total number of nanoparticles would be 10^6 and the irradiance 2.1×10^2 W cm^{-2}; for a 10 mm size, the total number of nanoparticles would be 10^9 and the irradiance 2 W cm^{-2}. These values are predictions of what amount of light absorption it

would take for a particular size of an excised tumour. A more thorough investigation has to be considered when the tumour is considered inside breast tissue due to light diffusion.

2.3.1 Light Delivery Methods

The concepts of photothermal therapy were introduced by de-constructing phenomenologically the therapy and presenting it in the first of two parts. The first part concerned the irradiation until the photonic energy to heat conversion, and the second part concerned the heat propagation and damage control. This subsection will review the laser delivery methods that directly impact light absorption by nanoparticles inside tissue at a certain depth.

The light sources applied in biomedical optics are lamps, LEDs and lasers, each of which has distinct characteristics that make them ideal for different applications. The best light source for photothermal therapy is laser light due to, among others, the narrower spectral width, wavelength choices, directionality and high intensity (Zhang 2014). Whenever possible, the laser specifications are chosen in each application to maximize the desired effects. Hence, in photothermal therapy, both properties of the incident light and tissue's, play a central role in selecting the optimal laser properties. These properties combined govern the light propagation into and through tissue and consequently heat generation and damage. *e.g.*, the narrow peak spectral absorption of most nanoparticles (Jaque *et al.* 2014) leads to a selection of a narrow spectral light source, such as the laser to optimize the heat generated by the nanoparticles. This section discusses some of the light properties that enhance light penetration depth in the breast tissue.

Some laser light properties, definitions and quantities considered when performing photothermal therapy treatment planning or device design are presented in the next list (Niemz 1996; Paschotta 2008; Sheng *et al.* 2017; Welch and Van Gemert 2011):

- Irradiance [W/m^2]: is equal to the flux density crossing a surface.
- Fluence rate [W/m^2]: is equal to the flux density seen by the absorber[1].
- Light intensity [W]: the power of the incident light.
- Spatial profile[-]: defines the spatial distribution of the incident irradiance of a laser beam (*e.g.*, Gaussian, flat-top, highly-modulated multimode).
- Spectral profile [nm]: describes the relationship between light intensity as a function of wavelength.
- Spot size[m^2]: provides a measure of the irradiated area.
- Temporal profile[ns]: expresses the beam intensity over time (*i.e.*, constant wave, pulsed or frequency domain).

[1] In https://omlc.org/news/sep05/irradiancemovie.html is shown the distinction between fluence rate and irradiance.

As already discussed, light can cause tissue damage. The ANSI Z136, IEC 60825 and EN 207 standards regulate the light source properties to prevent any damage to biological tissue, and they are considered to do, *e.g.*, optical imaging but not therapy. Hence, the laser source characteristics will have to be tailored to the tissue's optical properties to ensure that the absorbed energy does not significantly damage the skin. However, there are some light properties already discussed which can be generalized. The laser wavelength would have to be one such that would explore the biological windows' low attenuation, specifically in the first biological window because most nanoparticles have an operation range on that window (Jaque *et al.* 2014). The other known properties that can influence the fluence rate in depth without increasing irradiance are the laser temporal profile and the spot diameter (Sheng *et al.* 2017), which will be discussed in the next paragraphs.

2.3.1.1 Temporal Profile

A laser beam can have three operating modes. The continuous wave (CW) mode is characterized by steady light emission, which lasts from a few milliseconds up to 1 second. A pulsed laser beam is characterized by an interrupted laser beam ranging from 0.5 ms to 1 ns. With a frequency-modulated beam, the light intensity ranges within hundreds of MHz.

When considering the laser pulse through a heat confinement result, as it is studied in Jacques (1993), one sees that the optical zone (d) and the laser pulse (t_p) have the relation $t_p = \frac{d^2}{k}$, where k is the thermal diffusivity. In this context, the optical zone constitutes the laser-induced heat source in depth. Hence, to achieve a larger optical zone, a larger pulse width must be considered.

Figure 2.4 shows the temperature change in depth for different laser pulses (Jacques 1992). The absorption coefficient dominates the scattering parameter and is 10^4 cm^{-1}. The pulse radiant exposure (irradiance of a surface integrated over time) is constant at 100 mJ/cm^2. Although this plot is not representative of what temperature increase is like in tissue as it can be seen through both axis values, the overall variation between the temperature increase of the different pulse width' plots is, especially the relation between the pulse width and the temperature increase in depth which is the focus.

The last two paragraphs' conclusions lead to a constant wave light source to maximize the energy absorption in-depth.

2.3.1.2 Spot Diameter

Figure 2.5 shows the fluence rate as a function of tissue depth for different simulated flat-top beam radius. The incident irradiance, or irradiance at the surface, is maintained constant for each beam spot, implying that the light intensity is necessarily higher for a higher beam radius. Naturally, this implication results in an increase in fluence rate for larger beam diameters at higher depths. At the largest beam diameter, the fluence rate at

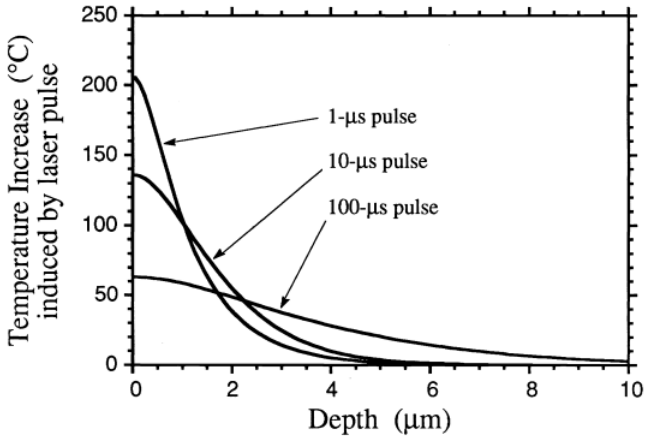

Figure 2.4: Temperature increase as a function of depth for different laser pulses with the same radiant exposure (irradiance of a surface integrated over time of irradiation). The thermal confinement effect at the surface is lower when the pulse duration is larger. Retrieved from Jacques (1992).

a depth of 0.3 mm is higher than the irradiance at the tissue's surface due to the scattering of light.

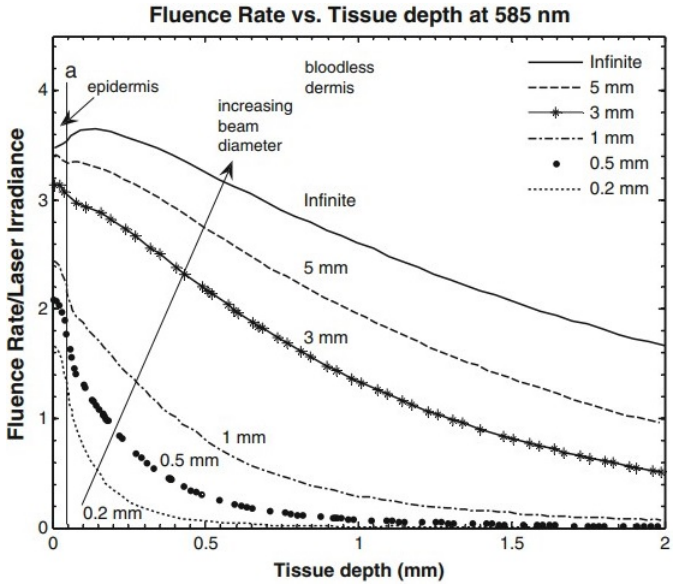

Figure 2.5: The fluence rate along the laser beam axis is shown as a function of depth from the skin surface up to 2 mm. Several beams with different radius from 0.2 mm to *infinite* are presented, with the same incident irradiance (1 W cm^{-2}), delivered by a flat-top beam profile. Retrieved from Welch *et al.* (2010).

2.3.2 Model Comparison of Nanoparticle-Mediated Photothermal Therapy

In this subsection are discussed the most common experiment and numerical models of tackling nanoparticle-aided photothermal therapy. The models will be discussed in some detail, and particular emphasis will be placed on the difference between the different numerical models. These studies have recognized the importance of using photothermal experiments in optical phantoms embedded with nanoparticles to validate their numerical simulations.

It is critical to have temperature measurements throughout the whole experiment in time and space. There are three categories of temperature monitor devices: volumetric, surface and local. Volumetric thermometry readings in temperature take in several points of a volume. One of the most popular techniques employed is magnetic resonance temperature imaging, where the temperature measurements are considered in each $\sim mm^3$. In surface thermometry, several points on a surface are monitored. Using an infrared camera is one of the most employed thermal sensors in medicine. Local thermometry probes such as thermocouples, or fibre optic sensors are used to read the temperature at the desired location (Welch and Van Gemert 2011).

However, it is not always possible to measure the temperature and predict the light dosage at every point. That is one reason why numerical simulations take a crucial part in photothermal therapy to estimate the therapy's success, perform calorimetric calibrations and treatment planning (Miaskowski and Subramanian 2019).

Figure 2.6 presents a block diagram representing the four stages in which the numerical method of photothermal therapy can be divided. The first stage deals with determining the fluence rate using the tissues optical properties and the laser beam characteristics. With these results in hand, one can determine the rate of heat generation inside the tissue. The next step deals with heat propagation, and with the help of the tissues' thermal properties, an estimate of the temperature can be obtained. In the last stage, one considers the temperature, time of exposure and tissues' rate constants to estimate the damage accrued.

Different numerical methods and equations can be applied at each stage. The choice of using the appropriate numerical method is often conditioned by the type of characteristics of the experiment combined with the model restrictions. Cheong *et al.* (2008) and Reynoso *et al.* (2013) used in their numerical simulations a solution to the diffusion approximation to model the light propagation inside tissue and the classic heat transfer equation to estimate the temperature inside an optical phantom with nanoparticles. Elliott *et al.* (2009) reproduced the experiment from Elliott *et al.* (2007) using the Eddington approximation instead of the diffusion approximation to compute the fluence rate. Several studies suggest that there are two approaches when it comes to simulating photothermal therapy with nanoparticle-filled mediums: either consider the nanoparticles part of the medium and the local absorption and scattering coefficients would reflect its presence (Elliott *et al.* 2007; Elliott *et al.* 2009) or consider them as individual light-absorbing particles inside a medium where the heat generation would be proportional to

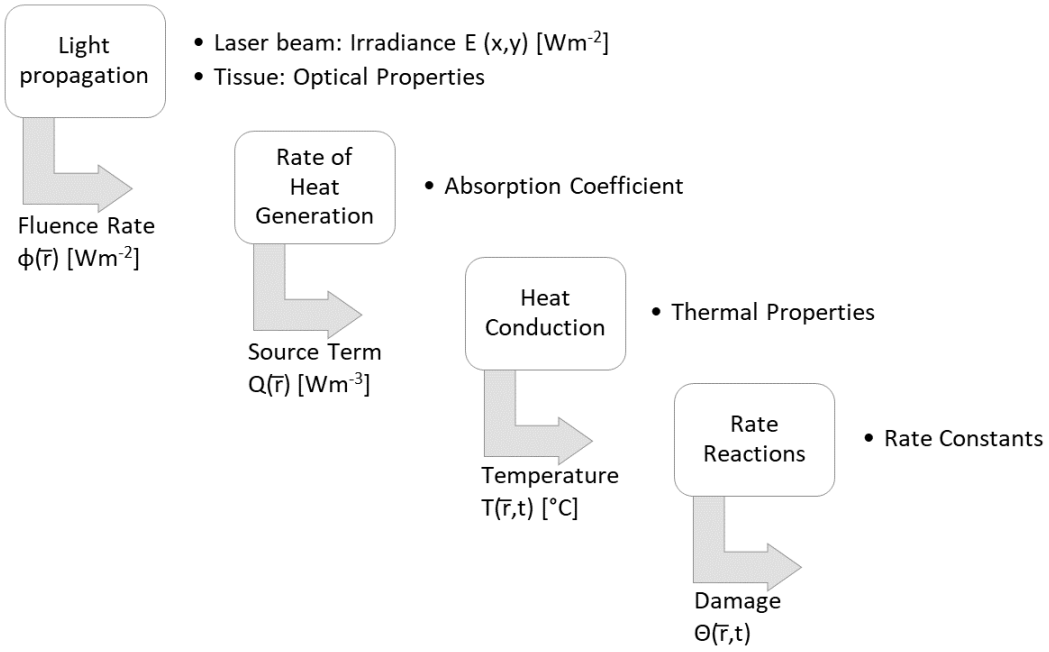

Figure 2.6: Block schematics of the photothermal therapy numerical model. Each of the boxes can have several numerical methods to choose. This diagram is adapted from reference Welch and Gemert (2010).

the absorption cross-section of each nanoparticle and the fluence rate is then computed (Cheong *et al.* 2008; Jakub *et al.* 2018; Reynoso *et al.* 2013). There are many different approaches to model this therapy numerically, each having pros and cons, which will be discussed in the next paragraphs.

Elliott *et al.* (2007) These authors present a rather exhaustive study with two 2-layered phantom-cylinders with different optical properties. Figure 2.7 shows an illustration of one of the phantoms. These phantoms differ by their optical properties. Phantom *A* has an absorbance[2] of 0.55, and phantom *B* has 0.695. The phantom cylinder top-part is composed of a mixture of agar and water, while in the bottom part, the same mixture was filled with a concentration of nanoparticles similar to that of the highest concentration they would deem to be suitable for therapy. They calculated the optical properties of the agar mixture and the mixture with nanoparticles, making it two distinct regions of optical properties. The thickness of the first layer is 1.1 cm, the second layer 4 cm, and its diameter is 2.3 cm. The phantoms were irradiated with four different CW laser intensities: 0.4 W, 0.8 W, 1.0 W, 1.5 W; in the centre of the top face-layer for 3 minutes. It was assumed a Gaussian lateral profile, and the width was adjusted accordingly to account for the depth width, as mentioned in Welch (1984).

A magnetic resonance thermometry 2D imaging (MRTI) apparatus was used to measure the phantom's temperature. The experiment lasted 300 seconds, and the temperature

[2]Absorbance A is proportional to the attenuation coefficient by $A = (\mu_a + \mu's)/\log_{10}(e)$

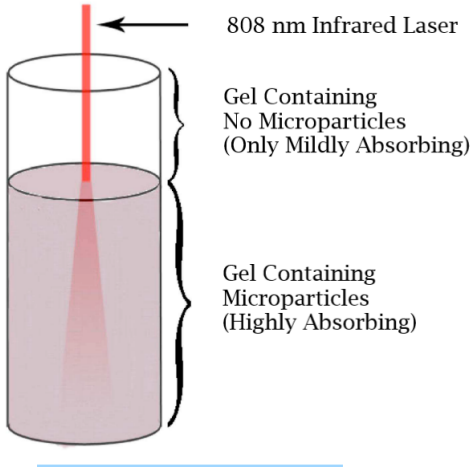

Figure 2.7: Illustration of the two-layer phantom with nanoshells in the bottom layer shows how the 808 nm laser was introduced from the top. Retrieved from Elliott *et al.* (2007)

readings were done at a rate of 5 seconds.

To numerically compute the temperature, they used the Gaussian solution of the optical diffusion approximation coupled with the classic heat transfer equation. In other words, in equation 2.13 with the terms for metabolic heat rate and blood density were set to zero since it was an optical phantom and not a tissue. Newton's law of cooling was also considered to simulate the surface's interaction air. Figure 2.8 illustrates the measured temperature on the left side, and on the right-side is shown an overlay of finite element isotherms of 5, 10 and 12 ^{o}C.

The conclusions were somehow misleading since for phantom *A* the results showed overall a smaller difference between experimental data and numerical simulations and a higher difference between them for phantom *B*, which had a higher optical density. This higher difference made them use a different numerical method to solve the radiative transfer equation, which will be discussed later in this section.

Cheong *et al.* (2008) replicated the experiment of Elliott *et al.* (2007) numerically, namely phantom *A* and the 1.5W CW laser intensity. Conceptually they did not consider the nanoparticle filled medium as a whole but used the same optical properties for the entirety of the phantom and determined the fluence rate in each position $\vec{r}$ using the same methods of Elliott *et al.* (2007). In their assessment of the therapy, this approach would be preferred over attempting to measure the absorption and scattering properties of a tissue-like medium filled with an unrealistic homogeneous GNP distribution (Reynoso 2011).

The heat transfer equation included an additional sum term which accounted for each nanoparticle. The results of both numerical models are shown in figure 2.9. On the left side are shown the results of Elliott *et al.* (2007), where the temperature change is

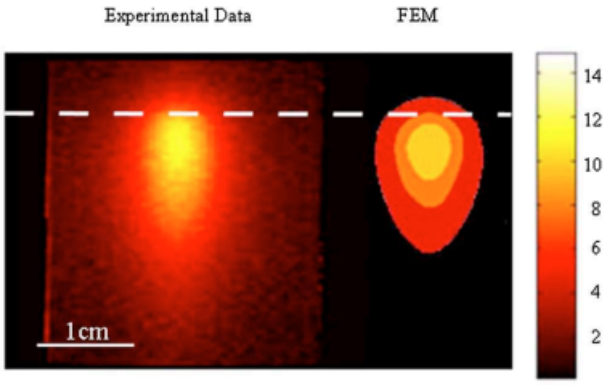

Figure 2.8: Experimental and finite element data comparison in temperature readings inside a 2-layer agar phantom. The white line defines the transition surface, separating the volumes with and without gold nanoparticles. The phantom was irradiated with a laser intensity of 1 W. Results retrieved from Elliott *et al.* (2007).

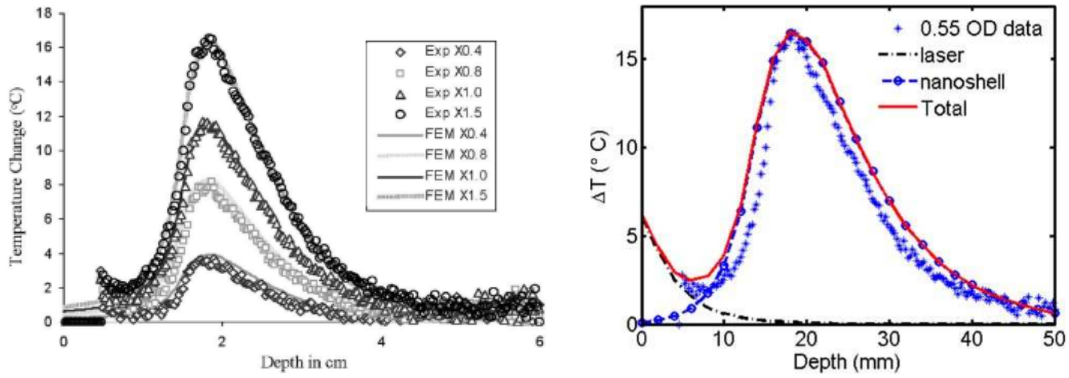

Figure 2.9: Numerical and experimental results of the temperature change as a function of depth are shown on the right from Elliott *et al.* (2007) and the left from Cheong *et al.* (2008). Experimental data is shown in points, and lines present the numerical results. Different laser intensities are represented on the left, while on the right only for 1.5 W. Also shown on the right are the different heat components of the total temperature (red), the nanoparticles component in blue and the laser component in black.

presented as a function of depth. The experimental data is shown in points while the numerical results lines for 0.4 W, 0.8 W, 1.0 W and 1.5 W. The plot displayed on the right show results from Cheong *et al.* (2008), also showing temperature change as a function of depth for the 1.5 W. In black and blue, the laser and the nanoparticles' heat are presented on the right-side plot. The sum of both contributions is presented in red.

Figure 2.10 shows the same comparison between the two studies, this time showing the results of the change in temperature as a function of time. Experimental data is shown in data-points, and the lines show the numerical results. On the left, the results of the 0.4 W, 0.8 W, 1.0 W and 1.5 W laser intensities are displayed, while the right plot shows the

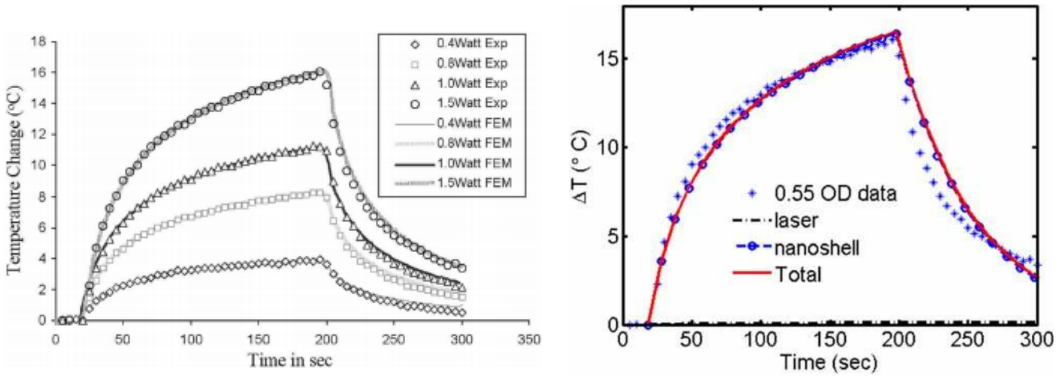

Figure 2.10: Comparison results of temperature change as a function of time between two diffusion approximation based numerical models are shown on the right and left from Elliott *et al.* (2007) and Cheong *et al.* (2008). Experimental data is shown in points and lines the numerical results. On the left, the different laser intensities are showed while on the right, only the 1.5 W laser intensity. Also shown on the right are the different heat components of the total temperature (red), the nanoparticles component in blue and the laser component in black.

experimental data and simulated contributions of the 1.5 W laser intensity.

Both studies show comparable results between the experimental and numerical data. Elliott *et al.* (2007) present the maximum temperature difference in percentage between the numerical simulations and the experimental results to be 17%, while considering all data, they agree within 3%. On the other hand, Cheong *et al.* (2008) present temperature results systematically higher than those measured experimentally, being those within the average percentage difference of 10%.

This 10% average percentage difference showed the need to keep developing this numerical approach.

Elliott *et al.* (2009) To account for Elliott *et al.* (2007)'s study shortcomings on the numerical model side for phantom *B*, Elliott *et al.* (2009) tested a different numerical model for light propagation. The phantom set up was also replicated. They used two optical phantoms with an optical density (OD) of 0.695 and 1.49, defined hereon as phantom *B* and *C*. These correspond to a reduced scattering coefficient of 0.089 $mm^{-1}$and an absorption coefficient of 0.071 $mm^{-1}$with 1.1×10^9 nanoparticles/ml (these nanoparticles would occupy 1/500 000 of the total volume (Elliott *et al.* 2009)) for phantom *B*. Phantom *C*'s optical properties were determined to be $\mu_s' = 1.92$ $cm^{-1}$and an absorption coefficient $\mu_a = 1.51$ $cm^{-1}$with $2.53{\times}10^9$ nanoparticles/ml.

For comparison purposes, they considered solving the radiative transfer equation using the delta-P1 approximation (You *et al.* 2005) along with the diffusion approximation, maintaining the classic heat transfer equation and its properties. The delta-P1 approximation models the scattering phase function and the radiance in a diffuse scattering and

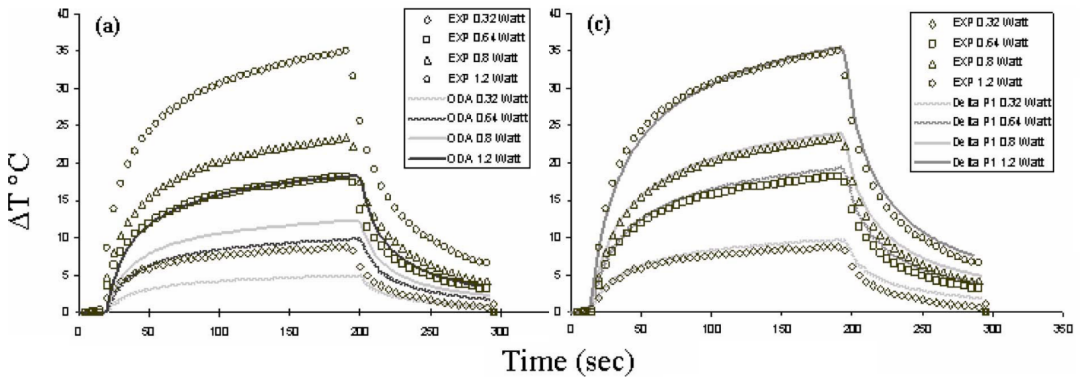

Figure 2.11: Shown is the change in temperature versus time for the 1.45 OD phantom *C*. The points reflect the measured temperature and the lines the simulated temperature. On the left, the experimental values are compared to diffusion approximation simulations. On the right, they are compared with the δ-Eddington approximation. Adapted from Elliott *et al.* (2009).

a forward scattering component.

Figure 2.11 presents the change in temperature in time for the 1.45 OD phantom in the highest temperature point. The points show the experimental results whereas, the lines represent the simulated temperature, on the right the results from the δ-Eddington approximation and on the left the results from the diffusion approximation simulation. For an even higher OD phantom, the optical diffusion approximation results are even further apart from the experimental data. The average RMS difference is 5.5 ± 3.1 ^{o}C, while the δ-Eddington approximation is 0.88 ± 0.31 ^{o}C.

This study concluded that the δ-Eddington approximation is also not a simulation model that accounts for slightly broader temperature distribution in-depth compared to the experimental results.

Reynoso *et al.* (2013) extended the concept model of Cheong *et al.* (2008), applying it to a geometric breast using water optical and thermal properties. With this phantom geometry, they concentrated on distributing gold nanoparticles within a small sphere, irradiating its surface as presented in figure 2.12. On the left side of this figure is shown the temperature variations in a cross-ectional view after 180 s of 1W CW 808nm laser irradiation. The hottest spot on this figure depicts the heat generated by an embedded 4mm-sphere of nanoparticles, and the second hottest is attributed to the laser heating the surface skin. The right side shows a 1D temperature variation collinear with the laser beam axis and the nanoparticles' centre. The pink area highlights the zone where the nanoparticles are.

The concentration of nanoparticles differed from what was considered in the other studies. It was increased to make it optimal for the highest temperature achieved up to 9.3×10^{10} nanoparticles/ml. Although this study aimed not to validate the possibility of

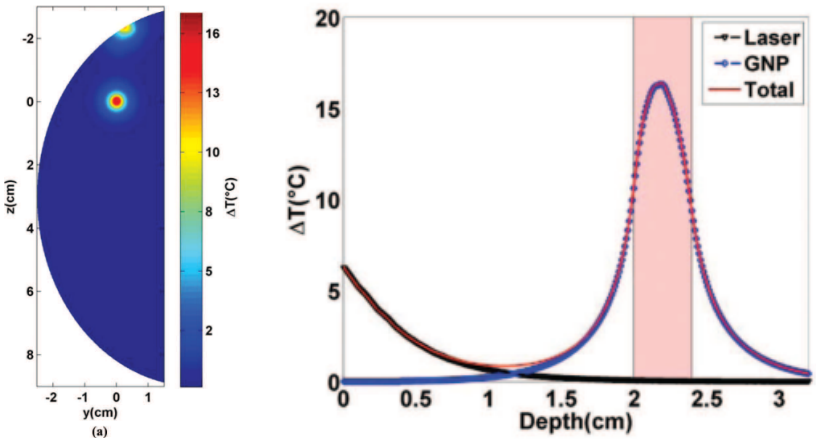

Figure 2.12: Left - a cross-sectional view of a breast meshed-phantom showing the temperature changes after 180 s. The hottest spot depicts the heat generated by an embedded 4mm-sphere of nanoparticles, and the second hottest is attributed to the laser heating the surface. Right - Temperature changes along the laser beam axis for the breast phantom heated with a 1W CW laser source at 180 s of irradiation. The pink area highlights the area where the nanoparticles are. The black line represents the heat generated by the laser light absorption, the blue represents the heat generated by the nanoparticles alone, and the red both temperatures summed. Retrieved from Reynoso *et al.* (2013).

performing photothermal therapy in-depth with a direct comparison of an experiment with an optical phantom mimicking the same optical and thermal properties, it certainly opened a window of an opportunity to study it.

2.4 Chapter Conclusion

Light propagation inside tissue is governed not only by the lights' but also by tissues' properties. Knowing these properties allows one to correctly interpret diagnostic measurements, plan therapeutic protocols or design diagnosis and therapeutic devices. However, determining correctly optical properties can be a tricky procedure since most of these properties depend on wavelength, temperature and pressure. With ongoing treatment, most molecules undergo structural changes such as a decrease in water concentration or variation in oxygenation, which impacts the estimation of the temperature and partially the effectiveness of the treatment. This chapter discussed the most critical components of this therapy's success. Firstly, the two most important components affecting photothermal therapy's effectiveness are the characteristics of the laser beam such as beam spot size and profile, laser intensity, wavelength, exposure time, temporal profile, and the characteristics of the target tissue defined by absorption and scattering coefficients and thermal properties. Secondly, nanoparticles play a crucial role in providing additional heat to produce sufficient thermal damage to the targeted tissue, where before using them, a negligent temperature change was observed. The nanoparticles' concentration, size, and optical properties are some of the most critical parameters that affect photothermal therapy's success. Thirdly, modelling correctly nanoparticle-mediated photothermal therapy is a complex but necessary task.

Several questions remain when probing the accuracies of the light propagation methods studied. Most studies discussed (Cheong *et al.* 2008; Elliott *et al.* 2007) provide the Gaussian solution for the diffusion approximation in situations that the limitations of this model are hardly met. Consequently, their results are highly dependent on the optical properties of the tissue. Other ways of providing a solution for the radiative transfer equation to account for this problem will be explored.

Cheong *et al.* (2008) and Reynoso *et al.* (2013) considered the problem where it is wrong to assume a highly heterogeneous tissue with strikingly unequal optical properties due to the presence of nanoparticles. The solution would be to measure first the optical properties of the tissue and the nanoparticles, and after administrating the nanoparticles determine their concentration in tissue. In this way, one can separate the contributions for the laser heating and nanoparticles plus laser heating, making the numerical model faster and more accurate than simply using the optical diffusion approximation. Although this is an interesting point of view at the beginning of the therapy, once the thermal effects kick in and start to change the optical properties, it does not make sense maintaining this argument. The possibility of using a heterogeneous mesh capable of varying their optical parameters is the most appropriate since it has more capabilities of being applied in live temperature readings and measuring dynamic optical properties.

The three optical properties were not used at the same time in their numerical models. These impact significantly the estimation of the temperature and the thermal damage in tissue. These will also be taking into consideration in this study. Additionally, none of

the studies presented used similar biological tissue's optical properties in their phantoms, which also impacts the fluence rate, the temperature achieved and, consequently, the thermal damage.

Several numerical models will be considered to address these issues in which the biological complexity will be increased, and different irradiation schemes will be tested. The objective will be to use photothermal therapy to treat breast cancer, maximizing the thermal damage in malign tissue and minimizing it to the healthy one.

Chapter 3

Materials and Methods

Chapter Overview This chapter describes the development of phantom production, tissue characterisation and numerical simulation protocols. In pursuance of the ideal photothermal therapy conditions, to be later applied in real-life situations, one needs to develop a cycle increasing complexity between the design of the phantom production and its optical characterisation, numerical simulations and planned photothermal experiments in controlled conditions.

The phantom production protocol aims to create a similar geometry to the breast one, with comparable properties. The numerical models are tested extensively with close to real-life conditions, and the photothermal experiments provide results closely related to a similar treatment applied to the breast. A comprehensive study of different phantom production components is presented, and a choice of its components to mimic breast properties. The experimental apparatus to measure the phantom's optical properties must determine the phantom's absorption and scattering coefficients, significantly impacting the therapy's effectiveness. The development of a photothermal mimicking experiment such that most of the conditions and properties are known and controlled would estimate the temperature in the desired place by the numerical models. Furthermore, develop a numerical protocol specialising in the light propagation model to increase the complexity of the model by including skin and several laser sources to limit light dosage in healthy tissue. This chapter ends up with detailing and discussing the software to pursue the objectives of this thesis.

Introduction There is a need to develop medical tissue-simulating phantoms to mimic the properties of biological tissues, such as breast, skin or liver, to create and develop diagnostic imaging systems, plan physical therapeutic interventions, test therapeutic systems, and devise performance tests between different systems.

Biological tissue can be characterised by different physical properties such as acoustic, chemical, electromagnetic, mechanical, optical, and thermal. In turn, these properties can be themselves a function of position, time or even having interdependent relationships like the optical scattering and wavelength and temperature (Jacques 2013; Jaywant *et al.* 1993). Ideally, to simulate light and breast tissue interaction, all of these properties and their interdependencies would have to be considered since the interplay between different physical events impacts the therapy's effectiveness, as figures 2.2 and 2.3 suggest. In practice, most of these interdependencies can be discarded due to their negligible influence on the desired outcome and limitations in computing power. 45 ^{o}C is the desired target temperature for this study, where thermal interactions are dominant. Consequently, the variations in optical properties due to tissue conformal changes and their dependency on temperature or even protein denaturation are discarded, since they happen at temperatures above 60 ^{o}C. Additionally, the non-linear absorption of light in the matter, which happens at a higher fluence rate than those planned to attain in this study, will not be considered. Thus, this work considers only optical and thermal interactions and their properties as many other authors do so (Elliott *et al.* 2009; Jacques 1993; Liu *et al.* 2013; Qin and Bischof 2012; Reynoso *et al.* 2013; Sajjadi *et al.* 2013).

3.1 Measuring Optical Properties

There are several options to determine the optical properties of biological tissue (Kim and Wilson 2010; Liu *et al.* 2013; Patterson *et al.* 1991b). These can be grouped into two classes: direct and indirect methods. The first class refers to types of experiments developed to measure the optical properties of optically thin tissues directly and are independent of mathematical models. The indirect methods derive the phantom's optical properties from a dependent parameter such as the transmittance or the diffuse reflectance and use mathematical models of the radiative transfer equation to estimate properties such as absorption and reduced scattering coefficients (Cheong *et al.* 1990; Kim and Wilson 2010; Patterson *et al.* 1991b).

Table 3.1 presents the average optical properties of breast and skin tissue determined at 808 nm wavelength and are based on Jacques (2013) review article. Here are presented the mean and standard deviation of the reduced scattering coefficient and absorption coefficient, refractive index, and scattering anisotropy.

Due to the high scattering properties of skin and breast tissue's and the devices available in the laboratory to perform this kind of measurements, a setup was chosen based on direct methods. Therefore, each photon has to interact at most once with the tissue on average. Hence, given the optical properties already shown in table 3.1, the thickness of

Type	μ_s' [cm^{-1}]	$\sigma_{\mu_s'}$ [cm^{-1}]	μ_a [cm^{-1}]	g	RI
Breast tissue	10.3	3.4	0.176	0.95	1.4
Skin	23.3	10.69	0.289	0.6	1.4

Table 3.1: Mean and standard deviation of reduced scattering coefficient in breast and skin tissue at 808 nm. The absorption coefficient, anisotropy and refractive index values are also presented. These values were retrieved from Jacques (2013) and Metwally *et al.* (2015).

the sample l must be less than one mean free path, *i.e.*, $l \ll 1/\mu_t$. So, $\mu_t = \mu_s'/(1-g) + \mu_a = 103.2$ cm^{-1}, which means a thickness of less than 10 μm. It is possible to have such thin samples using a freezing microtome, but this may induce tissue conformational changes and, therefore, a change in optical properties due to freezing and thawing. Additionally, with such a small tissue thickness, the interaction probability is necessarily low and can be easily masked by fluctuations of the incident flux or by a non-uniform response of the integrating sphere (Kim and Wilson 2010), which must be avoided.

To partially circumvent these obstacles, one can consider a thicker sample up to 10% of the reduced scattering mean free path (*i.e.*, $1/\mu_s' \sim 1$ mm), but this consideration comes with some restrictions. The acceptance of the solid angle must be less than 10^{-5} sr, and the use of stronger collimation is imperative (Kim and Wilson 2010; Marchesini *et al.* 1989).

Kim and Wilson (2010) and Patterson *et al.* (1991a) discuss four different methods to measure the attenuation, scattering anisotropy, absorption and scattering coefficients. Due to available material restrictions, only two were considered in this study: the attenuation and absorption coefficient. The values for scattering anisotropy will be retrieved from the literature and the scattering coefficient is determined by subtracting the absorption component from the attenuation. The description of these experimental apparatus follows.

3.1.1 Experimental Apparatus to Determine the Reduced Attenuation Coefficient

A similar procedure to the one described in Kim and Wilson (2010) and Patterson *et al.* (1991a) was followed to measure the reduced attenuation coefficient μ_t'. A schematic diagram of this experimental apparatus is depicted in figure 3.1. The following materials were used:

(1) Two collimating Lens (ref: Avantes, COL-UV/VIS)

(2) Monochromatic laser source (ref: JDSU, L4-2495-003)

(3) Fibre-optic cables (ref: Avantes, FC-UVIR200-2)

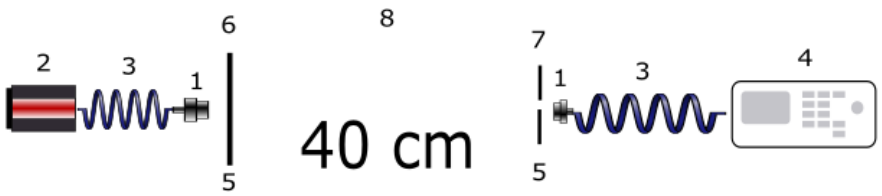

Figure 3.1: Schematic diagram to measure the attenuation coefficient. The numbers in the diagram highlight the different materials used to assemble this setup: 1 - collimating lens, 2 - laser source, 3 - fibre-optic cables, 4 - spectrometer, 5 - cage cubes, 6 - cuvette, 7 - pinhole and 8 - cage system construction rods.

(4) Spectrometer (ref: Avantes, Avaspec 2048)

(5) Two cage cubes (ref: Thorlabs)

(6) 1mm path length cuvettes

(7) 1mm pinhole (ref: Thorlabs)

(8) Cage system construction rods (ref: Thorlabs)

To the laser source (2) is attached a fibre-optical cable (3) and a collimating lens (1) at its end. The collimating lens (1) is attached to one of the cage cubes (5) with the appropriate adaptor. The cuvette (6) is placed in a cage cube (5), which has an appropriate adaptor so that the light rays are perpendicular to the cuvette's face. The other cage cube has a 1 mm pinhole (7) placed more than 40 cm apart from the sample with construction rods (8), thus maintaining the laser and the detector's necessary alignment and the required minimum solid angle. This cage cube (5) has another collimating lens (1) that leads the light into the spectrometer (4).

The Beer-Lambert equation (Beer 1852; Kim and Wilson 2010) was used to determine the reduced attenuation coefficient (μ_t'),

$$\mu_t' = -\frac{1}{t}\log\frac{I}{I_0} \tag{3.1}$$

where t is the thickness of the sample, I is the measured signal of the cuvette with the sample and I_0 the measured signal of the cuvette with distilled water. For each measurement of I and I_0, the spectrometer's time integration parameter was adjusted to obtain optimal spectral distributions averaged over at least ten times, and in the subsequent step, each intensity value was divided by their respective integration time. The I measurement was repeated five times, irradiating different positions of the sample. The I was determined by integrating the distribution area at twice the standard deviation from its mean and averaging the five different measurements.

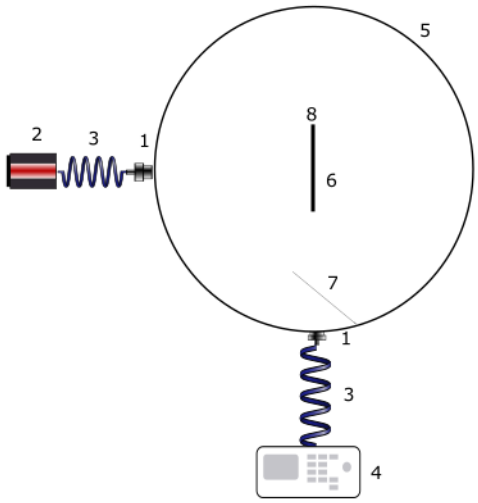

Figure 3.2: Schematic diagram to measure the absorption coefficient. The numbers highlight the diagram materials used to assemble this setup: 1 - collimating lenses, 2 - laser source, 3 - fibre-optic cables, 4 - spectrometer, 5 - integrating sphere, 6 - cuvette, 7 - integrating sphere's baffle and 8 - sample holder.

3.1.2 Experimental Apparatus to Determine the Absorption Coefficient

The absorption coefficient's setup (μ_a) is similar to the one described in Kim and Wilson (2010) and Marchesini *et al.* (1989). Its schematic diagram is illustrated in figure 3.2. The following materials were used:

(1) Two collimating Lens (ref: Avantes, COL-UV/VIS)

(2) Monochromatic laser source (ref: JDSU, L4-2495-003)

(3) Fibre-optic cables (ref: Avantes, FC-UVIR200-2)

(4) Spectrometer (ref: Avantes, Avaspec 2048)

(5) 3-Port Integrating Sphere (International Light, INS 250)

(6) 1mm path length cuvette

(7) Baffle

(8) Sample holder

The cuvette (6) was placed in a 3D printed sample holder (8) and at the centre of the integrating sphere (5). The baffle (7) was placed at the exit's port to prevent the detector (4) from receiving light that interacted only once with the integrating sphere in each measurement. Coupled in the remaining two ports of the integrating sphere (5) was the

laser source (2) and the spectrometer (4) using a collimating lens (1). The absorption coefficient (μ_a) was determined using the relation

$$\mu_a = \frac{1}{t}\frac{I_0 - I}{I_0} \tag{3.2}$$

where I_0 is the measurement with distilled water, I the signal measured with the sample solution and t its thickness. For each measurement, the I and I_0 time integration parameters of the spectrometer were adjusted to obtain optimal spectral distributions averaged over at least ten times, and in the subsequent step, each intensity value was divided by their respective integration time. The I parameter's measurement was repeated five times, irradiating different sample positions. The I parameter was determined by integrating the distribution area at twice the standard deviation from the distribution's mean and averaging the five different measurements.

The reduced scattering coefficient (μ_s') was determined using the equation $\mu_s' = \mu_t' - \mu_a$.

3.2 Phantoms for Photothermal Experiments

Optical phantoms provide a crucial component in the biomedicine research field. They may be applied to testing system designs, being a reference of calibration to optimise setups or even serving as a reference to devise performance comparisons between different systems. They are comprised of three main components: matrix, scattering and absorbing agents. The success of photothermal therapy is highly dependent on the breast's optical properties and the density of the nanoparticles present in the tumour (Hirsch *et al.* 2003; Qin and Bischof 2012; Soni *et al.* 2013). Hence, knowing the properties of the components and their density in the phantom is also a critical step. These phantoms can be tailored to a specific purpose by selecting different materials as their components.

A matrix provides the phantom's structure and can be made of different materials: water, hydrogel, polyester, polyurethane or silicon. The last two matrix materials (polyurethane and silicon) result in a solid permanent phantom and are usually used to calibrate setups. In comparison, the first two matrix materials (water and hydrogel) have a soft medium, are biocompatible and have more comparable physical and thermal properties to biological tissue than the former two. The absorber materials are varied and range from whole blood, ink, molecular dyes or even fluorophores. The most used optical scattering agents for producing phantoms include lipids, microspheres and titanium dioxide (Pogue and Patterson 2006). Each of these scattering and absorbing materials provides different properties to the phantom and is therefore used in different situations. In the first stages of this research study, there is no specific need for definite absorption and scattering properties of the phantom, and thus, aside from the matrix component, the choice is made by the ease of access. In this study, the choice of matrix, absorption, and scattering agents were agar powder, Indian ink, and Intralipid. The choice of the matrix component must rely on water or hydrogel since they mimic better breast properties

compared to the other materials. The final choice of a gelling agent, such as agar, was made so that the phantom could have distinct regions of homogeneous optical properties, such as a distinct region of gold nanoparticles.

There are some limitations to the production of phantoms with these materials. The optical properties of produced phantoms usually differ even when using the same recipe but different bottles of the same brand materials (Di Ninni *et al.* 2010). Phantoms made with biological material usually are not stable and change their properties with time. In practice, this means that every produced phantom must be optically characterised.

Standard agar has a fusion point over 80 ^{o}C and solidifies at 35 ^{o}C, and it is widely used in thermal therapy studies as they are one of the most promising candidates for creating heterogeneous phantoms with different thermal and optical properties (Dabbagh *et al.* 2014). Intralipid is also thermally stable under specific conditions. While the scattering remains unchanged, the absorption varies when the Intralipid is subject to changes in temperature, but these changes in absorption are wavelength-dependent, and in the near-infrared region of the electromagnetic spectrum, they remain unchanged (Lai *et al.* 2014; Rowe *et al.* 2013). Intralipid provides a similar scattering as in biological tissues due to the scattering molecules' different sizes. Indian ink is also thermally stable at these ranges of temperatures. The desired maximum temperature in the photothermal experiments with phantoms is at most 45 ^{o}C.

3.2.1 Optical Setup Performance Test

To test the two setups detailed in section 3.1 and shown in figures 3.1 and 3.2, a phantom fabricated by the INO - Biomimic Phantoms company was used. This phantom was produced with polyurethane as the matrix, the scattering agent is titanium dioxide, and the absorber is carbon black. The materials used provided it with long-term stability and reproducibility such that it allowed them to design the phantom with an absorption coefficient of 0.1 cm^{-1} and a reduced scattering coefficient of 10 cm^{-1}at 800 nm wavelength.

This *INO* phantom was used to make a performance comparison between two optical characterisation systems, which were labelled *Bouchard* and *measured*. The first system refers to the experimental setup made by the INO company to characterise the *INO* phantom optically. This characterisation was performed using a 20 mm thick by 55 mm radius sample. The use of a pulsed laser allows an independent determination of the absorption and the reduced scattering coefficient. The reduction of the collected signal allows the determination of the absorption coefficient, and the measurement of the extension of the pulse's distribution permits the determination of the reduced scattering coefficient. The specific methods for measuring the optical properties used by the INO company are described in Bouchard *et al.* (2010). The *measured* setup refers to the two experimental apparatus described in sections 3.1.1 and 3.1.1.

Table 3.2 presents the results of the two optical characterisation setups, *Bouchard*

setup	μ_a [cm^{-1}]	μ_s' [cm^{-1}]	g	μ_t' [cm^{-1}]
Bouchard (@ 800 nm)	0.1 ± 0.06	10.1 ± 0.2	0.62 ± 0.02	<u>10.2 ± 0.3</u>
Measured (@ 808 nm)	0.09 ± 0.09	<u>10.8 ± 0.9</u>	-	10.9 ± 0.8

Table 3.2: Comparison between two optical characterisation systems denominated *Bouchard* and *measured*. The *Bouchard* optical properties refer to measured properties considering the experimental procedure and setup in Bouchard *et al.* (2010). The *measured* optical properties consider an average and standard deviation of the measurements performed with the setups described in this section. The properties underlined were computed using the equation $\mu_t' = \mu_s' + \mu_a$.

and *measured*. The *Bouchard* system measured an absorption coefficient of 0.1 cm^{-1} and a reduced scattering coefficient of 10.1 cm^{-1}. The averaged standard deviation of the fitted optical properties for each sample are σ_{μ_a}= 6.2% and $\sigma_{\mu_s'}$ = 1.8%. The *measured* setup measurements were 0.09 cm $^{-1}$ for the absorption coefficient and 10.8 cm^{-1} for the reduced scattering coefficient. The uncertainties associated with these measurements were σ_{μ_a} = 0.09 cm^{-1} and $\sigma_{\mu_s'}$ = 0.9 cm^{-1}, respectively. The optical properties in Bouchard *et al.* (2010) were determined at 800 nm, while the *measured* setup is optimised for 808 nm. This disparity in wavelength leads to a decrease in the measurement of both optical properties in the *measured* system inferior to 5 % (INO 2019).

Overall, when comparing both setups' values on the absorption coefficient's results and associated uncertainties, the *measured* absorption setup provides an acceptable estimate of this sample's absorption coefficient since both the measurement and experimental uncertainties of the two systems are comparable. The absorption coefficient of this sample is very low, and in turn, some issues such as laser power instability or non-uniformity of the integrating sphere scattering surface increase the measurement's fluctuations and uncertainty. When comparing both setups' values on the reduced scattering coefficients' results and associated uncertainties, it can be highlighted that the *measured* phantom attenuation uncertainty represents a 7% variation, which is acceptable given the magnitude of the reduced scattering coefficient.

The *measured* setup gives a reasonable estimate of the measurement of the reduced scattering and an acceptable measurement of the absorption coefficient. An optical power meter would decrease the uncertainties of both coefficients since this device is better to measure energy flux than a spectrometer. Nonetheless, these results grant the confidence to choose the adequate concentrations of the chosen materials to design phantoms and choose the appropriate light source parameters to increase the therapy's effectiveness.

3.2.2 Materials' Characterisation

The following brands for each material were chosen to produce the optical phantoms: agarose powder (Agar-Agar, Vahiné, France), Intralipid® 20% (SMOFlipid 200 mg/ml

emulsion for infusion, Fresenius Kabi Austria GmbH, Graz, Austria), Indian ink (black 23 ml, Vallejo) and a solution of biocoated gold nanoparticles developed by Silva *et al.* (2016).

Some of these materials' optical characterisation must be considered to design an optical phantom with such optical properties. Hence, some useful parameters also have to be considered, such as the intrinsic absorption ξ_a [$m^{-1}kg^{-1}$] and the intrinsic reduced scattering ξ_s' [$m^{-1}kg^{-1}$] account for the inherent property per mass of that component. The absorption coefficient and reduced scattering can be determined as (Huppert 2013)

$$\mu_a = \sum_i \xi_a^i \rho^i \tag{3.3}$$

$$\mu_s' = \sum_i \xi_s^{i\prime} \rho^i \tag{3.4}$$

where ρ^i is the concentration of the i^{th} component in the sample. To design them to have predetermined optical properties comparable to the breast ones, one must estimate what concentrations one should use. For Indian ink and Intralipid components, existing literature allows an educated estimate of what concentrations should be used, such as Di Ninni *et al.* (2010) and Lai *et al.* (2014). The order of magnitude considered reasonable concentrations in these references is 1 μl and 1 ml for Indian ink and Intralipid. The gellification phase starts at 0.5-0.8% of the agar's powder to the water's weight. A concentration of 1.5% of this brand of Intralipid was chosen to obtain a μ_s' of ~ 10 cm^{-1} to ensure similar properties as the breast optical properties, shown in table 3.1.

The protocol to obtain the gold nanoparticle's solution is presented in Silva *et al.* (2016) where these nanoparticles' optical properties are also characterised.

3.2.3 Phantom Protocol

Two homogeneous solutions of hydrogels were designed to produce a heterogeneous phantom. The protocol considered a mixture of agar, Indian ink, Intralipid, the nanoparticle' solution to mimic the tumour and GNP region of interest, and another one with the same base materials but without the GNP solution to mimic the breast region.

Here are presented the steps to produce 100 ml of the first solution:

1. 1.5 g of agar powder.
2. Put in a beaker 97 g of distilled water using a new pipette
3. Mix the agar powder and the water with a spoon and heat the mixture up to 90 ^oC.
4. Mix the solution until it drops to 50 ^oC and reheat again. (Repeat 2x)
5. Let the solution cool down to 40 ^oC

6. Take 1.5 ml of Intralipid and mix it with the previous solution.

The procedure to make the second solution was equal to the first one, where an additional step was added at the end: take 20 ml of the first solution and mix it with 20 ml of the gold nanoparticle solution. By restricting the temperature to less than 40 ^{o}C during the mixing, both the biocoating and the Intralipid maintain their biological structures intact. The next step in the process would be to put both solutions in an appropriate cuvette or a plastic mould, determine their optical properties and proceed with the experiment.

3.2.4 Thermal Properties

The thermal properties are an essential part of numerically estimating the temperature of the photothermal experiment. Table 3.3 shows the specific heat capacity c, density ρ, thermal conductivity k and the heat transfer coefficient h for breast and agar-gel. These thermal properties were taken from Cheong *et al.* (2008), Das and Mishra (2013), Dear *et al.* (1997), Elliott *et al.* (2007), Haemmerich *et al.* (2005), and Zhang *et al.* (2011). To the best of my knowledge, there is no reference in measuring the density of agar-gel. It is assumed to be the same as the waters' due to the small increase in weight and negligible volume change in the transition from liquid phase to gel.

	c [J Kg^{-1}K^{-1}]	ρ [kg m^{-3}]	k [W m^{-1}K^{-1}]	h [W m^{-2} K^{-1}]
Agar-phantom	4160	998 (H2O)	0.588	5
Breast	3000	920	0.42	3.4

Table 3.3: Thermal properties for agar-agar and breast tissue. These values were taken from Das and Mishra (2013), Dear *et al.* (1997), Elliott *et al.* (2007), Haemmerich *et al.* (2005), Miaskowski and Subramanian (2019), and Zhang *et al.* (2011)

Thermal properties of biological tissue such as breast tissue can change significantly, within an order of magnitude, depending on the fat content of the subject's breast, among other properties (Valvano 2010). The fact that the thermal properties of these samples are comparable suggests that the thermal interaction between the two samples are also comparable to some extent, and consequently, the temperature change. Hence, from a temperature increase perspective, these optical phantoms can help design better photothermal therapy experiments with some degree of accuracy since the thermal damage is proportional to the temperature and the time that the tissue is subject to that temperature (Niemz 1996).

3.3 Numerical Protocol

To present a numerical protocol, one should first define the most appropriate numerical models to solve the governing equations, define the physical domain of the research questions and the initial conditions and properties of that domain. The majority of numerical models for solving partial differential equations of continuum mediums can be classified into finite difference, finite volume, and finite element methods. In the next paragraphs are described the main characteristics of these methods.

The basis of the finite difference method is to consider a discrete grid over which one would use the Taylor expansion series as approximations for the governing partial differential equations, *e.g.*, diffusion approximation or Pennes' bioheat equation. This method solves algebraic finite difference expressions to estimate the variable of interest. On the one hand, the main benefits of this numerical method are: its simplicity to implement and computationally fast, high order is feasible, increasing the Taylor approximation and is explicit in time. On the other hand, when handling complex geometry in multiple dimensions, this method can become problematic since partial differential equations are considered topologic squares of line networks. This geometry would require complex mapping of functions that would relate to the grid. The solution of this method will be obtained at each node of the grid. The finite volume and finite element methods were developed to overcome these problems (Hesthaven and Warburton 2008; Mukundakrishnan *et al.* 2009).

The idea behind the finite volume method is to divide the geometry into several non-overlapping control volumes such that there is one control volume surrounding each nodal point. The main advantage of this method compared to the finite difference method is, it does not require the use of structured grids, *i.e.*, the control volumes are generally non-uniform. The governing equation would be integrated over each control volume to get the numerical solution. This method can handle complex geometries and is explicit in time. Its central inability is to extend high-order accuracy on general unstructured grids and has grid smoothness requirements (Hesthaven and Warburton 2008; Mukundakrishnan *et al.* 2009).

The finite element method splits the physical domain, defined as a mesh, into usually tetrahedral elements and detaches the problem of finding the solution for the entire physical domain to find the solution for each element. Each tetrahedral element is defined by four nodes and is a continuum inside itself. It has a unique solution if a set of boundary conditions is defined for it. On the one hand, the main advantage is it can combine high-order accuracy and complex geometries, but on the other hand, it is implicit in time and not well suited for problems with direction (Hesthaven and Warburton 2008; Mukundakrishnan *et al.* 2009).

The discontinuous Galerkin finite element method overcomes the finite element method's and the finite volume method shortcomings and combines their strengths. The discretisation of the physical domain, the mesh, is done into finite elements providing a

good precision as the number of elements compose the mesh. Each element has a set of shape or interpolation functions used to interpolate the domain variables of that element. Then a matrix equation for the same finite element is established. This matrix equation relates the nodal values of the unknown function to other parameters and elements. To find the global equation system for the whole domain, one must combine local element equations for all elements used for discretisation, and finally solve the global equation system (Hesthaven and Warburton 2008; Mukundakrishnan *et al.* 2009; Nikishkov 2004; Schweiger *et al.* 1993).

The Monte Carlo method The numerical methods discussed until this point provide a solution to the partial differential equations of interest using numerical approximations, *e.g.*, the physical domain's discretisation. However, the Monte Carlo method relies on the simulation of stochastic processes and sampling of stochastic (random) variables to estimate the partial differential equation's solution. In the case of the radiative transfer equation's solution, the Monte Carlo method estimates (*e.g.*) the absorption distribution in a physical domain by sampling a high number of photons (N) that would travel through a medium with a pre-defined absorption coefficient. Each photon can be absorbed in a different space-time point, and as the number of photons increases, the Monte Carlo estimate approaches the actual absorption distribution of that physical domain. The same approach is taken to determine the scattering and anisotropy distributions. These distributions are used to determine the physical domain's fluence rate (Alerstam 2011; Prahl 1988).

There are different possibilities of implementing the Monte Carlo method: in volume, element or finite difference form. Since the finite element method is chosen for solving the numerical partial differential equations of both the diffusion approximation and the bioheat equation, it is crucial that the Monte Carlo method software also provides a *meshed* solution so that the numerical differences due to the physical domains between the models are kept to a minimum.

3.3.1 Numerical Protocol

The numerical protocol developed in this study took its roots in the mathematical model presented in figure 2.6 and detailed in chapter 2. Figure 3.3 presents a schematics overview of the used numerical models and software included in the simulation protocol in each box. To define the element-mesh of the digital phantom, either the Iso2mesh (Fang and Boas 2009c) or GMSH (Geuzaine and Remacle 2009) were used. These programs create digital phantoms and define the physical domains in which the numerical models ran.

Once the physical domain was created, they were used to solve the light propagation considering two different models: the diffusion approximation and the Monte Carlo method. The software used to provide the fluence rate solutions were TOAST++

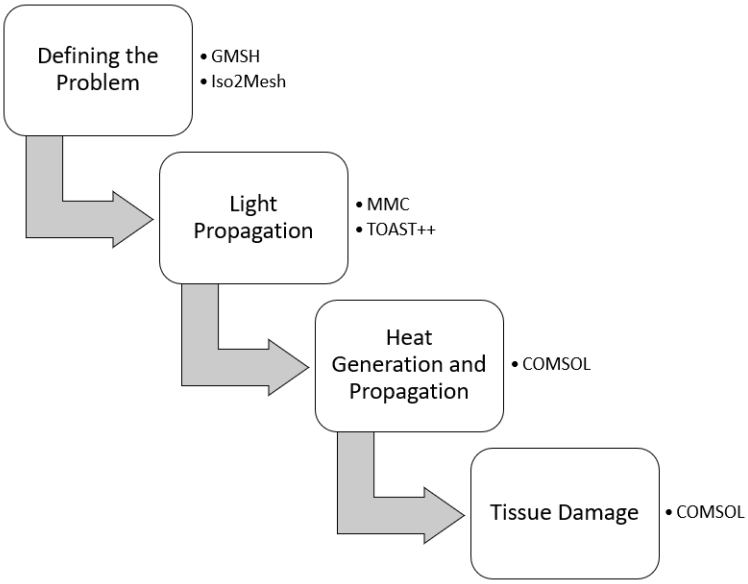

Figure 3.3: Diagram of the software used in each stage of the simulation.

(Schweiger *et al.* 2014) which considers the solution of the diffusion approximation using the discontinuous Galerkin finite element method and Mesh-based Monte Carlo (Fang 2010), which considers the solution of the Monte Carlo method in a mesh.

The commercial software COMSOL Multiphysics® was used to determine the temperature and damage in tissue and is based on the discontinuous Galerkin finite element method. MATLAB® and COMSOL Multiphysics® were used to perform the data analysis.

The next sections will dwell on a simple description of these numerical applications.

3.3.2 Diffusion Approximation with TOAST++

Toast++[1] (Schweiger *et al.* 2014) is an open-source toolbox developed for modelling and reconstruction in Diffuse Optical Tomography. It made possible the solution of both the forward problem and the inverse problem. The latter tries to find the optical properties with multiple optodes - which pairs of source and detectors distributed in the periphery of the digital phantom. The forward problem determines the fluence rate given the optical properties and illumination conditions. This module uses the discontinuous Galerkin finite element method to simulate the transport of light in highly scattering, inhomogeneous biological media, using the diffusion approximation to the Radiative Transfer Equation. The initial conditions needed include optical properties such as reduced scattering (μ_s') and absorption coefficients (μ_a), and refractive index (n). The basic units in Toast++ for length and time are mm and ps, respectively. Toast++ maps a domain to a correspondent mesh and uses basis functions $u_i(r)$ (vertex i of the tetrahedral element j)

[1] Acronym for Time-resolved Optical Absorption and Scattering Tomography

to establish a relation between them. In this way, one can assume that a function $f(r)$ of the domain Ω is:

$$f(\vec{r}) \approx f^h(\vec{r}) = \sum_i f_i u_i(\vec{r}) \tag{3.5}$$

As an example, the photon density distribution $\phi(\vec{r})$ in a 3D domain would be represented as an approximation $\phi^h(\mathbf{r})$ by:

$$\phi(\vec{r}) \approx \phi^h(\vec{r}) = \sum_i \phi_i u_i(\vec{r}) \tag{3.6}$$

Thus, the diffusion equation and boundary condition for a continuous wave source outside tissue given by:

$$-\nabla \cdot \kappa^h(\vec{r}) \nabla \phi^h(\vec{r}) + \mu_a^h \phi^h(\vec{r}) = 0, \ \vec{r} \in \Omega \tag{3.7}$$

$$\phi^h(\vec{m}) + 2\xi(c)\kappa^h(\vec{m}) \frac{\partial}{\partial \nu} \phi^h(\vec{m}) = q^h(\vec{m}), \ \vec{m} \in \partial\Omega \tag{3.8}$$

where the superscript h determines a function's approximation, $q^h(\vec{r})$ is the source distribution, $\kappa^h(\vec{r})$ is the diffusion coefficient, c is the velocity of light inside the medium, ξ is a function associated with the change of refractive index between the different mediums, and $\partial\nu$ is the outward boundary normal.

The forward problem's solution to light diffusion near the boundary is determined using the Fresnel law (Haskell *et al.* 1994). The light source is placed at the boundary considering a Neumann source to simulate an inward current with a Gaussian shape.

3.3.3 Monte Carlo method with MMC

MMC[2] (Chen *et al.* 2012; Fang 2010; Fang and Kaeli 2012; Yao *et al.* 2016) is a 3D Monte Carlo (MC) simulation software for photon transport in complex turbid media. It can use an FE-like tetrahedral mesh to represent complex structures, making it accurate, flexible, and memory efficient. MMC uses ray-tracing techniques to simulate a *photon-packet* propagating inside a mesh.

In the next list is presented a written flowchart of the MMC code. Keep in mind that position $\vec{r}$ and vector $\vec{v}$, define a 3D ray ($R(\vec{r}, \vec{v})$), and can be related to the Cartesian form (see Fang (2010)).

1 Start with photon packet of weight 1, in position $R(r_0, v_0)$, enclosed in the mesh element e_0.

[2] Acronym for Mesh-based Monte Carlo

2 Compute random scattering length $l_s = \exp^{a\mu_s^i}$ along with d. μ_s^i is the scattering coefficient of element i, and a is a random number $\in [0,1]$.

3 R is then tested against the 4 triangular faces of the tetrahedral e_0, to determine the exit point P_x.

4 Case condition:

4.a $|PP_x| \leq l_s$; $P = P_x$ and go to step #2

5 $P = P + vl_s$

6 Start a new scattering event, assuming a uniform random azimuth angle $\in [0, 2\pi]$ and uniform generated random elevation angle between $\in [0, 2\pi[$ following the Henyey-Greenstein phase function.

7 The photon packet weight is decreased along the trajectory according to Beer Lambert's law, considering the μ_a^i of each element i. The weight loss is deposited into the mesh using Barycentric coordinates calculated from the above Ray-tracing step.

A photon can be reflected or transmitted from a surface, depending on the reflection coefficient, R, using Fresnel's equation. If $R <$ a (random uniform number), the photon is transmitted and killed. If $R \geq$ a, the photon packet is reflected in a new direction. The output result of this code is the fluence rate.

3.3.4 Rate of Heat Generation

The rate of heat generation is determined considering at each nodal point the product (Reynoso *et al.* 2013; Welch *et al.* 2010)

$$Q^i = \phi^i \times \mu_a^i \tag{3.9}$$

where i refers to the nodal point i.

3.3.5 Bioheat Transfer Equation and Damage Integral with COMSOL

The COMSOL Multiphysics® software was chosen to model the bioheat transfer equation (equation 2.13) and to estimate the thermal damage (equation 2.16). Since this is a closed source computer-aided engineering program, the specific mathematical details to solve these equations are not available, to my knowledge. This software applies an implementation of the discontinuous Galerkin methods, transforming the heat transfer and damage equations into a linear system matrix and gives the possibility of selecting one solver from a pool of sparse direct solvers that have different properties, which can be selected depending on, *e.g.*, different computing systems (Lamien 2015).

The focus of this study is the optical propagation of light in biological matter, and since COMSOL Multiphysics® is applied with success in other studies already referenced

in this thesis, such as Cheong *et al.* (2008), Elliott *et al.* (2007), Elliott *et al.* (2009), and Reynoso *et al.* (2013), it was selected.

3.4 CHAPTER CONCLUSION

In the previous sections was argued that to test the effectiveness of the photothermal therapy in-depth, before treatment planning, one must develop four research topics at the same time: the production protocol of an optical phantom to validate, improve and serve as a reference to the numerical models, a setup to measure the optical properties of that phantom because the dependency of fluence rate on them, a protocol to experiment design and the numerical models to simulate those experiments.

In this chapter, were shown three protocols to aid this research project. The first one discussed the most appropriate components for producing a gelled phantom, which would most closely mimic the breast tissue's optical properties. Since the aim is to develop a phantom closely resembling breast tissue in its properties, the materials chosen included agar-gel, Indian ink and intralipid.

A second protocol was developed to measure the optical properties of highly scattering samples: the absorption coefficient and the reduced attenuation. A performance test was developed to test this experimental apparatus using a reference phantom and another system - which measured the absorption and reduced scattering coefficients of this reference phantom. The developed setup provided comparable results with the setup of reference and thus validated this protocol.

A third protocol was developed to compute the temperature and consequent tissue damage due to light exposure numerically. This protocol determines the fluence rate of a non-uniform 3D biological sample explicitly using one of two possible models: the diffusion approximation method or the Monte Carlo method, which lead to the determination of the local heat increase due to photon absorption. The temperature was determined using the bioheat transfer equation using the discontinuous Galerkin method. The validation of this protocol is done in the chapter that follows this.

Chapter 4

In-Depth Photothermal Therapy: Experiments and Simulations

chapter overview This chapter presents the implementation, results, and discussion of the previous chapters' highlighted research topics. An experiment was designed and conducted to benchmark the numerical protocols previously presented. Herein, the limitations of the light propagation models used and highlighted the limitations of this type of therapy are argued. These illations are considered jointly with state-of-the-art, designing and developing an ideal but realistic numerical simulation to assess the effectiveness of photothermal therapy using gold nanoparticles using different irradiation schemes.

4.1 Validating a Numerical Model Using a Photothermal Experiment

A photothermal experiment was designed to compare its data with numerical simulations' data and validate the numerical protocols. This experiment was designed to be compared with the other experiments from other authors discussed in the chapter 2. The comparison will consist of using similar optical properties applied to a different physical domain, a protrusion-like GNP-filled region of interest. This experiment will be more resembled with a realistic case of Gold NanoParticles (GNP) aggregation around and into a tumour, being at the same time a more challenging numerical problem to benchmark both models, instead of two regions with and without nanoparticles as other studies have done (Cheong *et al.* 2008; Elliott *et al.* 2007; Elliott *et al.* 2009).

4.1.1 Phantom Production

To produce the agar gel, the steps written in section 3.2.3 were followed. First, 2.0 g of agarose powder (Agar-Agar, Vahiné, France) was mixed in 200 ml of distilled water. The water was heated along with the agarose powder up to $\approx 90^{o}$C and mixed an additional two times to ensure a gel's homogeneous optical density. Then it was let cool off inside a 60×60×60 mm^3 custom-made acrylic holder, using a cylinder of 15.5 mm in diameter to create a 5 mm hole on top of the phantom and a small sample of this mixture was placed in a cuvette to perform the optical characterisation. These were let cooled down to ambient temperature.

Another batch of the agar mixture was re-heated and let cool down at a temperature close to 35^{o} C, then was added an equal amount of the solution of gold nanoparticles' solution (Silva *et al.* 2016) and mixed. This proportion of GNP solution and agar mixture was used to ensure agar gellification. This liquid mixture of agar and GNP was placed in the cylinder hole of 5 mm deep, and 15.5 mm in diameter and left to gellify.

A final mixture of agar gel was re-heated and let cool down to 40 ^{o}C, and a 4 mm layer of agar mixture was added to the phantom holder. The final phantom's geometry is depicted in figure 4.1.

4.1.2 Measurement of the Phantom's Optical Properties

The optical properties of the agar gel and, agar gel and GNP mixtures were measured using the experimental apparatus described in subsections 3.1.1 and 3.1.2, using an integrating sphere (International Light, INS 250), a laser diode source (Roithner, RLTMDL-808-5W-5) 808 nm wavelength and a spectrometer (Avaspec 2048, Avantes). The measured coefficients, the absorption coefficient and the reduced attenuation are shown in table 4.1.

For reference, it is also shown in this table 4.1 values of optical density for the regions of agar and GNP that Elliott *et al.* (2007) and Elliott *et al.* (2009) used in their study. In

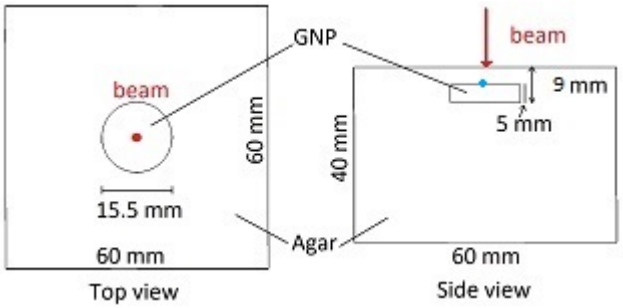

Figure 4.1: Gel phantom setup. The laser beam entry position and direction are depicted in red. The main component (agar) is made of 1% agar and water, while the smaller component (GNP) is made of 1% agar, 50% GNP solution and 49% water. The blue dot represents the thermocouple position.

Sample	μ_a [cm^{-1}]	μ_t' [cm^{-1}]	μ_s' [cm^{-1}]
Gel	0.02	1.78	1.76
GNP	0.31	3.20	2.89
OD = 0.695	0.71	1.60	0.89

Table 4.1: Measured optical properties of the agar gel phantom and the mixture of gold nanoparticles (GNP) and agar gel. The last line presents the optical density of both a phantom studied in Elliott *et al.* (2007) and Elliott *et al.* (2009).

these studies, the authors show some limitations of the diffusion approximation model to estimate the experimental temperature correctly. It is known that this model can only be applied in conditions such that $\mu_s' \gg \mu_a$, which is not the case in their study since the absorption and reduced scattering are comparable in the GNP region.

The optical phantom had its absorption coefficient chosen to compare to that of Elliott *et al.* (2007) and Elliott *et al.* (2009). Having a comparable absorption coefficient, the heat generated in the GNP region would be comparable. Moreover, the diffusion approximation is not valid in the authors GNP region as the optical properties are comparable (Arridge 1999), but in our case, the argument for the condition $\mu_s' \gg \mu_a$ could be made.

4.1.3 Experimental and Simulation Setup

Experimental Setup The phantom was irradiated on the top surface of the box with a continuous wave diode laser of 1.1 W power and an FWHM of 7 mm, as represented in the diagram of figure 4.1. A multi-mode fibre and a collimator were used with the laser to provide a more portable and stable beam. Assuming that this could be modelled as a Gaussian laser beam profile (Sturesson 1998, p. 35), one can associate the FWHM to a beam diameter of 11 mm at the $1/e^2$ points of the distribution, making an incident irradiance at the phantom's surface of 2.31 W/cm^2.

Of the different thermometry measurement devices available to record temperature, the thermocouple was the most reliable for this kind of photothermal experiment due to mechanical and temperature changes. Temperatures were registered using a type K thermocouple (Labfacility, Z2-T-1M) and a thermocouple converter (Seneca K109TC) connected to a LabVIEW® graphical interface which allowed a temperature data acquisition rate averaged to one second. The thermocouple was placed at the closest boundary of the GNP cylinder from the irradiated surface and aligned with the light source axis, and its position is represented in figure 4.1 as a blue dot. The constant wave laser was on for 706 s. The radiation absorbed by thermocouple was considered and subtracted from experimental results, as suggested in Cain and Welch (1974) and Manns *et al.* (1998). The ambient temperature was measured at 22.9 ^{o}C.

Initial Conditions of the Optical Numerical Models The initial conditions common to both optical numerical models follow. The measured optical parameters are presented in the first two rows of table 4.1. Additionally, a scattering anisotropy of 0.9 is assumed (Elliott *et al.* 2007), and the refractive index is that of water 1.33 (Jacques 2013).

The diffusion approximation software (TOAST++) modelled the Gaussian profiled source with σ = 3.07 mm, like a Neumann current with a Gaussian profile. A Gaussian profile was also selected in the Monte Carlo software with the same beamwidth as in the diffusion approximation software. Ten million events were considered in the Monte Carlo's simulation.

The fluence rate, which was the standard output of both simulators, was multiplied by the local absorption coefficient to get the volumetric heat and then was used as a 3D heat source in COMSOL Multiphysics®. The codes for the optical simulations are presented in appendix B and here.

Initial Conditions of the Thermal Numerical Model The COMSOL Multiphysics® settings considered a top surface that transferred convective heat with the room using the Newton cooling law with the respective coefficient at 5 W $K^{-1}m^{-2}$ (Welch and Van Gemert 2011) while the other surfaces were considered to be in thermal isolation. This latter assumption could be considered wrong since the acrylic box that holds the optical phantom has a very low - but not zero - thermal convective constant. This assumption was negligible during the laser-on phase and more significant when the light was off and the phantom cooling down. Hence the results presented consider only the laser-on phase where the assumption is valid. The blood density and the metabolic heat coefficient of the Pennes bioheat equation were set to zero due to the absence of biological tissue. This consideration converts the Pennes bioheat equation into the classical heat transfer equation. The density, heat capacity and thermal conductivity properties of the agar mixture and GNP solution were considered the same as water due to the GNP insignificant influence in a thermal perspective.

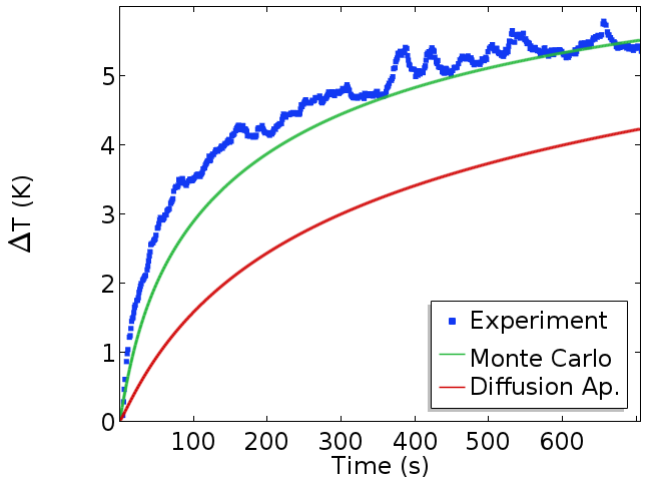

Figure 4.2: Comparison of simulation and experimentally measured increase in temperature, 4 mm below the surface, as a function of time. The diffusion approximation and Monte Carlo models are shown in green and red, respectively, compared with the experimental results shown in blue.

4.1.4 Results and Discussion

Figure 4.2 presents the change in temperature as a function of time at the position of the thermal probe. The experimental data is shown in blue, Monte Carlo simulations shown in green and diffusion approximation simulations shown in red. There are some local variations in the measured temperature along time, especially in the 350 to 500 seconds range. The thermocouple probe has a higher absorption coefficient in the near-infrared region of the electromagnetic spectra than the medium surrounding it. The metallic probe leads to a higher ratio of absorbed photonic energy to be diffused to its surroundings, which happens in a non-linear fashion, as the experimental data suggests. This fact can be confirmed since the instant the irradiation phase stopped; this behaviour was not observed. This a known phenomenon and is also described in Cain and Welch (1974) and Manns *et al.* (1998).

The same metrics of comparison presented in Elliott *et al.* (2007) between data and simulations were also used in this study, namely the average percentage difference and the Pearson correlation coefficient. The average percentage difference between experimental and Monte Carlo data was found at 4.5%, while for the diffusion approximation and experimental data, 61%. The Pearson correlation coefficient between the same pairs is 0.98 and 0.95, respectively.

Monte Carlo simulation's results show a very good agreement with experimental data when considering the two metrics, while the diffusion approximation results provide a good correlation coefficient with data, but not as good average percentage difference. These results can be compared to (Elliott *et al.* 2007), where this problem is explored in a similar experiment as presented in on the left plot of figure 2.10. The authors found

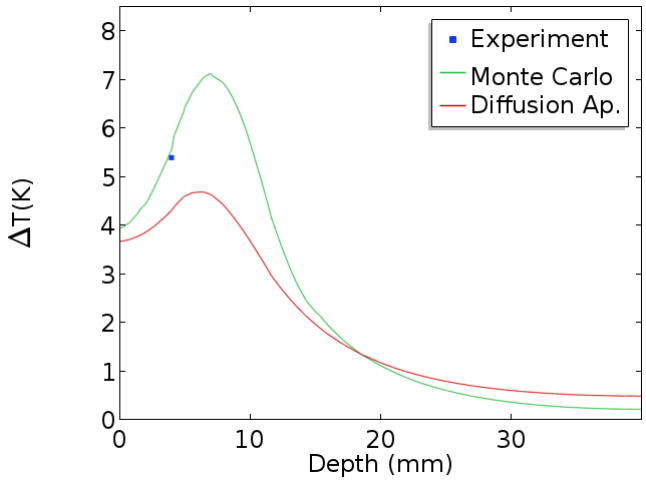

Figure 4.3: Temperature increase at $t = 706$ s right before the laser was turned off. The x-axis represents the *depth* axis aligned with the laser beam axis, which is located at the centre of two faces of the cube. The Monte Carlo simulation results are presented in green, the Diffusion Approximation in red and the experimental data in blue.

that the diffusion approximation used to model the experiment was quite off and therefore they adjusted the computed physical parameters (reduced scattering and absorption coefficients) within a computed uncertainty of 10% to fit better the data. The authors presented an average percentage difference and Pearson correlation coefficient of 4.5% and 0.99.

In Elliott *et al.* (2007)'s study, the optical parameters were changed within the reported 10% experimental uncertainty. To test the sensitivity of the diffusion approximation' results to the measured optical parameters of our model, some of the optical properties were changed by 20%, namely the reduced scattering and the absorption coefficients. This change resulted in a decrease in the average percentage difference from 61% to 23%. Although this value is far from the 4.5% reported in Elliott *et al.* (2007), this change in optical properties highlights the model sensitivity to them, enhancing its importance on measuring the reduced scattering and absorption coefficients of the samples. Figure 4.2 results leads to the conclusion that the diffusion approximation cannot be considered even though $\mu_s'/\mu_a \approx 10$, thus, the relation $\mu_s' \gg \mu_a$ does not stand.

Figure 4.3 shows the temperature change in depth along the laser beam axis inside the phantom, the second before the laser was turned off. The GNP region starts where the experimental point stands and extends itself until a depth of 9 mm. The temperature distribution of both models is different. The experimental temperature increase is at 5.40 K, while the temperature increase registered by the Monte Carlo and the diffusion approximation simulations are 5.56 K and 4.31 K, respectively. Using more thermocouple probes, or using a different temperature measurement technique, such as magnetic resonance temperature imaging, would allow a more comprehensive study of both simulated distributions distribution versus experiment.

When comparing it with similar temperature change distributions in Elliott *et al.* (2007) where the experiment duration took 120 second and the GNP region was 2.2 cm into the phantom, the maximum increase in temperature registered was ∼10 ^{o}C when considering the comparable irradiation power and optical properties. In this study, a maximum temperature change of ∼ 7 ^{o}C was computed at the 706^{th} second, at a deepness of 4 mm. This comparison suggests that the size of the inclusion with nanoparticles is a crucial component to temperature increase. The irradiance, the inclusions' optical properties, density and location inside the tissue also play a part in the increase of temperature, as Chanmugam *et al.* (2012) and Qin and Bischof (2012) highlight.

4.2 Model Comparison: Beam Profile Case Study

Elliott *et al.* (2007) and Elliott *et al.* (2009) discuss an overestimation of the simulated radial temperature distribution obtained with the diffusion approximation model compared with the experimental data. Since there was no experimental data to study this problem radially, one can only use the literature and compare qualitatively the two numerical protocols studied in this work. This effect can also be seen in figure 4.4, where are compared the diffusion approximation and the Monte Carlo simulations in contour plots showing the temperature increase in 1 ^{o}C, 3 ^{o}C and 5 ^{o}C.

In the hope of getting a more relevant insight on the results presented in figure 4.4 and to develop a new photothermal therapy simulation study, figures 4.5, 4.6 and 4.7 are presented. Figures 4.5 and 4.6 show a comparison of the decimal logarithm of the fluence rate and the volumetric heat source parameter between the two models in the $y = 0$ plane, which contains the beam axis. In yellow is displayed the GNP region, whereas in blue and red are presented the contour plots of Monte Carlo and diffusion approximation simulation results, respectively. Figure 4.7 shows the fluence rate (left side) and volumetric heat source (right side) as a function of depth along the beam axis. In blue is shown the Monte Carlo simulations, and in green the diffusion approximation results.

Figure 4.5 shows that the radial dependence of the fluence rate is strikingly different in both models. In the diffusion approximation model, the fluence rate is diffusely distributed inside the phantom. Simultaneously, Monte Carlo simulations results show a predominance of fluence rate along the beam axis, which is expected since the scattering is predominantly forward ($g = 0.9$), making more photonic energy available to be absorbed by the nanoparticles in the centre. This outcome results in a more centralised volumetric heat source parameter than a more evenly distributed volumetric heat, especially inside the GNP region, as displayed in figure 4.6.

The temperature distribution presented in figure 4.4 of both simulations is very similar compared to the respective distribution of the volumetric heat source shown in figure 4.6. Additionally, considering the results from the right plot of figure 4.7 leads to the conclusion that heat confinement plays a significant role only when VHS $\sim 10^{6}$ W m^{-3}.

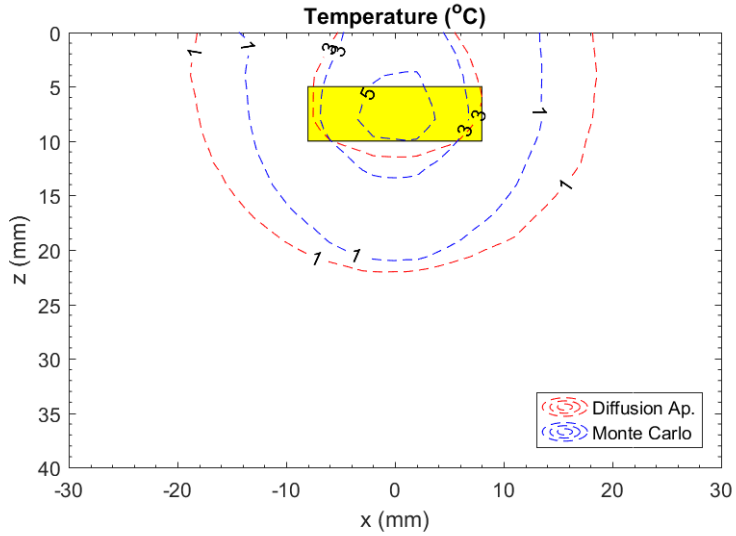

Figure 4.4: Temperature increase at t = 706 s right before the laser was turned off, at y=0. The Monte Carlo simulation results are presented in blue and the diffusion approximation results are shown in red.

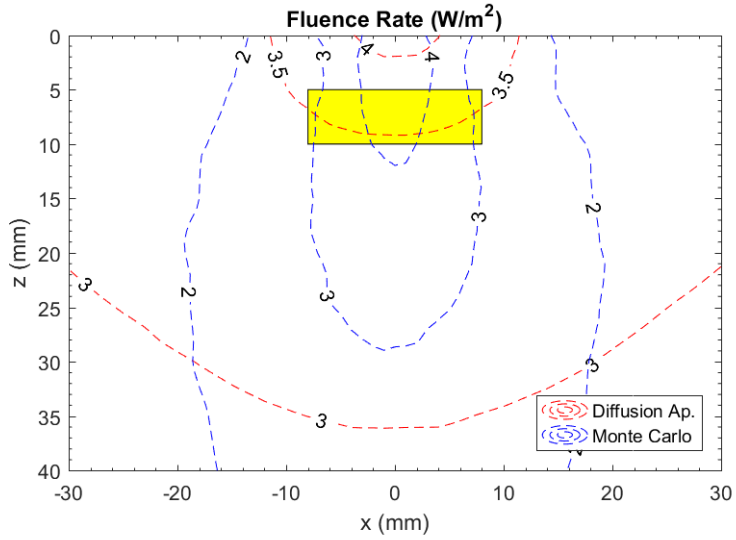

Figure 4.5: Decimal logarithm based fluence rate comparison between the simulation models at y=0. In blue is represented the decimal logarithmic fluence rate ($\log_{10}(\phi)$) of Monte Carlo simulations of the model described in 4.1 in contour lines. In red is represented the diffusion approximation counterpart. In yellow is depicted the cylinder region with nanoparticles.

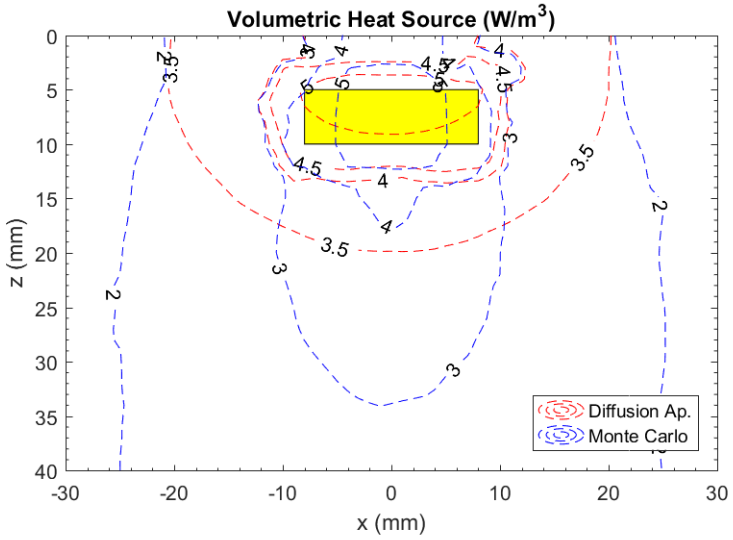

Figure 4.6: Decimal logarithm based volumetric heat source comparison between the simulation models at y=0. In blue is represented the decimal logarithmic volumetric heat source ($\log_{10}(\phi)$) of Monte Carlo simulations of the model described in 4.1 in contour lines. In red is represented the diffusion approximation counterpart. In yellow is depicted the cylinder region with nanoparticles.

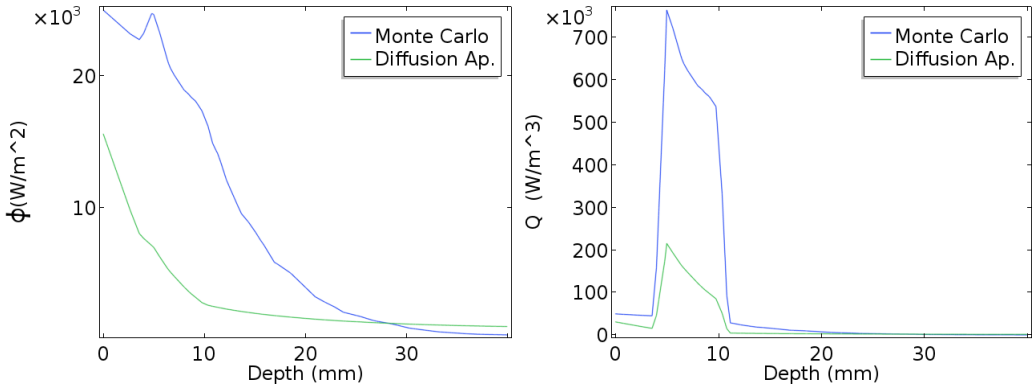

Figure 4.7: Fluence rate (left side) and volumetric heat source (right side) as a function of depth along the beam axis from the skin surface. In blue is shown the Monte Carlo simulations, and in green the diffusion approximation.

The results presented up until this point show that the Monte Carlo simulation protocol performs better when compared to the experimental data and the literature results instead of the diffusion approximation model. Thus, this is the protocol of choice to continue the studies in this thesis. Figure 4.6 suggests that a larger beamwidth should be preferable so that the temperature distribution along each latitude of the phantom is equivalent.

4.3 Compressed Breast Numerical Model

4.3.1 Introduction and Simulation Design

A more realistic example is considered in this section, using a compressed breast model to study different irradiation schemes to increase the effectiveness of doing in-depth photothermal therapy. The compressed breast is usually considered within the medical imaging community to make the optical path shorter.

In this simulation, the addition of skin is going to be considered. Different laser configurations will be considered to study which one has more energy absorption in the tumour tissue than the healthy skin tissue. The aim is to minimise the damage in healthy tissue while providing an adequate temperature at the desired site. The optical properties of skin and breast tissue, namely scattering and absorption coefficients, are the mean of those shown in Jacques (2013) review article, while the thermal properties were retrieved from the COMSOL Multiphysics® software and presented in Hasgall *et al.* (2015).

This study will be pursued only with numerical simulations by increasing the number of sources, changing the beam profile and position, and using the highest realistic concentration of gold nanoparticles mentioned in the references considered in this thesis (Qin and Bischof 2012).

4.3.2 Simulation Setup

Geometry The breast mesh used to perform this simulation was published in Deng *et al.* (2015), where the authors used 2D CT scanned breast data, transformed it into a 3D digital phantom and then characterised its optical properties by developing an inverse problem algorithm solver based on Monte Carlo simulations.

Only the breast geometry is considered in this study, not the optical properties determined in Deng *et al.* (2015). This choice of homogeneous optical properties will limit the number of outcomes in the simulation and allow us a more direct interpretation of the effectiveness of the therapy. Homogeneous optical and thermal properties are attributed to the phantom, tumour inclusion, breast and skin regions. These properties can be seen in table 4.2.

The thickness of the compressed breast totals 29.5 mm. A spherical inclusion of 1 cm in diameter simulating the tumour and gold nanoparticles region was included in the mesh centred at (0, 0, 15) mm, and the first 2 mm from the surfaces were considered skin

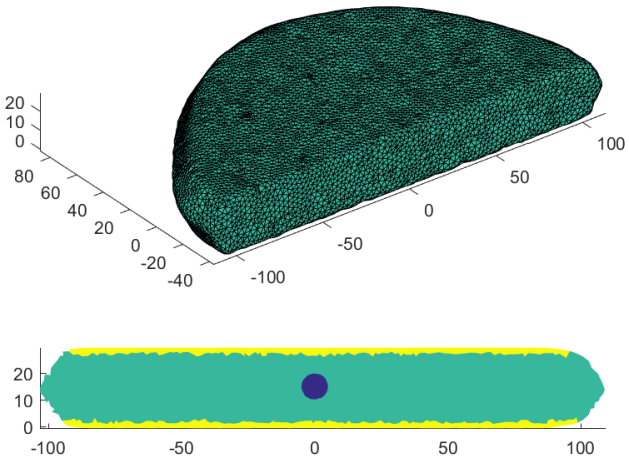

Figure 4.8: Top: Overview of the compressed breast mesh. Bottom: a cross-sectional view of compressed breast at y=0. Different colours represent different regions. In yellow, light green and blue are depicted the skin, breast and, GNP and tumour tissues, respectively. This digital phantom was presented in Deng *et al.* (2015).

region. This digital phantom can be seen in figure 4.8. On top is displayed the whole breast mesh, whereas in the bottom image is displayed a cross-sectional view on the y=0 plane wherein different colours identify different regions: in blue, yellow and green are presented the added GNP and tumour, the skin and breast regions, respectively.

Digital Phantom On the one hand, there is a known limitation of the optical simulation program (MMC), which does not allow it to have parallel regions (i.e., a slab of skin over breast tissue) and is reported on their website[1]. The suggestions regarded therein also do not provide a solution for this specific digital phantom. The solution to circumvent this problem was to select the elements whose nodes were within 2 mm to the surface and assign them skin optical properties. This selection is the reason why the skin-breast interface in figure 4.8 is wiggly. On the other hand, COMSOL Multiphysics® numerical models do not converge when using this mesh due to self-intersecting face elements. Thus, an additional mesh was considered in heat diffusion along with the compressed breast one. The latter digital phantom has only one domain with thermal breast properties and a *slab* phantom, which includes one 1.5 mm skin layer on top, a 26.5 mm thick breast and another 1.5 mm skin-layer. This last digital phantom is presented in figure 4.9. The same volumetric heat is considered for computing the heat diffusion on both meshes.

This information is conveniently displayed as a schematic diagram in figure 4.9.

The photothermal therapy's goal is to achieve an increase in temperature of 8 K. As discussed in section 2.2, this thermal regime does not produce drastic variations in optical properties due to conformal tissue changes at temperatures above 60 ^{o}C. Additionally,

[1] http://iso2mesh.sourceforge.net/cgi-bin/index.cgi?Doc/FAQ - 1^{st} topic

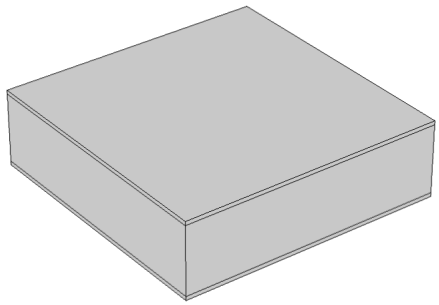

Figure 4.9: *Slab* digital phantom. This mesh was used only on the heat diffusion part to simulate the skin temperature. It serves as a replacement for the *breast* phantom used until now, having the same thickness (29.5 mm) and 100 x 100 mm. It comprises three layers, two 1.5 mm thickness skin layers and one 26.5 mm breast layer.

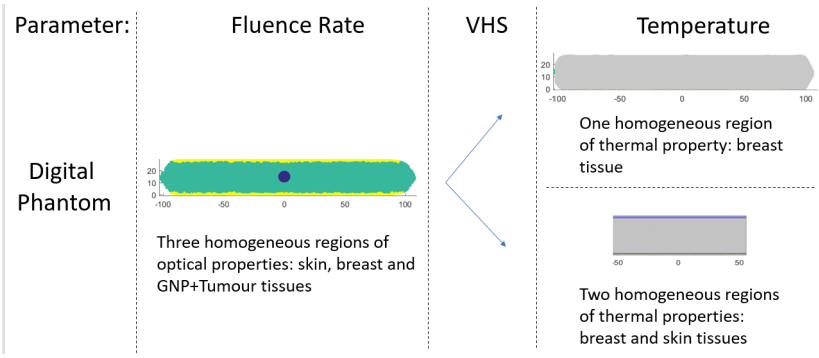

Figure 4.10: Schematic diagram of the different digital phantoms and their properties applied in different phases of the numerical protocol. The row *Parameter* defines the variable that is determined at each specific step. One digital phantom was considered with three homogeneous regions of interest to determine the fluence rate, shown in blue, green and yellow, representing the GNP-region, the breast region and skin, respectively. With the fluence rate, the volumetric heat was determined. The temperature was determined with two in two different meshes, one with a homogeneous medium (top) and another with two homogeneous properties shown in blue and grey, representing the skin and breast tissue, respectively (bottom). These digital phantoms and their properties can be seen in figures 4.8, 4.9 and table 4.2.

Table 4.2: The optical and thermal properties used to characterise the compressed *breast* and the *slab* phantoms in the simulations are presented. The labels for each variable are superscripted, *Breast* is meant for breast tissue properties, *GNP* for tumour and GNP tissue, *Skin* for skin tissue, *b* stands for blood. The variables are: μ_a is the absorption coefficient, μ_s' is the reduced scattering coefficient, g the scattering anisotropy, C_p is the specific heat at constant pressure, k is the heat diffusion coefficient and ρ the density, ΔE the activation energy and A the frequency factor. The remaining parameters are: RI the refractive index, $LaserOn$ the time when the laser was irradiating the sample, T^{ini} is the initial and assumed body temperature, T^{amb} the room temperature, Q^{met} is the metabolic heat coefficient, and h^{Body} is the convective heat transfer coefficient of the body, $T_{d,h}$ is the hyperthermia damage temperature and $t_{d,h}$ the time to reach heat damage.

Optical Properties			Thermal Properties		
μ_a^{Breast}	0.018	mm^{-1}	T^b	37	K
μ_a^{GNP}	0.151	mm^{-1}	C_p^b	3651	$J\ kg^{-1}K^{-1}$
μ_a^{Skin}	0.029	mm^{-1}	ω^b	1.8E-4	s^{-1}
$\mu_s'^{Breast}$	1.03	mm^{-1}	ρ^b	1046	$kg\ m^{-3}$
$\mu_s'^{GNP}$	2.3	mm^{-1}	T^{ini}	37	^oC
$\mu_s'^{Skin}$	2.33	mm^{-1}	T^{amb}	23	^oC
g^{Breast}	0.95		Q^{met}	1522	$W\ m^{-3}$
g^{GNP}	0.95		C_p^{Breast}	2348	$J\ kg^{-1}K^{-1}$
g^{Skin}	0.6		C_p^{Skin}	3391	$J\ kg^{-1}K^{-1}$
RI	1.4		κ^{Breast}	0.21	$W\ m^{-1}K^{-1}$
LaserOn	120	s	κ^{Skin}	0.37	$kg\ m^{-3}$
Thermal Properties					
h^{Body}	3.4	$W\ K^{-1}\ m^{-2}$	ρ^{Breast}	911	$kg\ m^{-3}$
$T_{d,h}$	45	^oC	ρ^{Skin}	1109	$kg\ m^{-3}$
$t_{d,h}$	50	s	-	-	-

the non-linear absorption of light in matter happens at higher fluence rate values than those planned to attain in this simulation. Hence, in this simulation, the optical and thermal properties are maintained constant as other authors do so (Cheong *et al.* 2008; Elliott *et al.* 2007; Jaunich *et al.* 2008; Reynoso *et al.* 2013).

The optical and thermal properties used on these meshes are shown in table 4.2. The tissues' optical properties were taken from the review article of Jacques (2013), where the authors compiled data from several sources and determine the mean breast and skin tissue, whereas the properties for the gold nanoparticles and concentration were determined considering Qin and Bischof (2012). All of the thermal tissue properties used were the *fat*, and *skin* materials listed by the COMSOL Multiphysics® software suite and the references for those values are presented in Hasgall *et al.* (2015) database.

Irradiation Conditions In chapter 2 is shown that a laser with a flat-top profile of size larger than 5 mm should be enough to maximise the radiance in-depth in the beam axis (1D). However, as already discussed, using a small beam width does not evenly distribute

the temperature increase at the same depth in the whole region of interest. Five different laser beam profiles are considered, four flat-top (square-shaped) beam profiles of 5 mm, 10 mm, 20 mm and 40 mm placed outside the breast and an additional pencil beam placed after the skin region. This last addition to the different irradiation configurations had the objective to decrease the distance between the laser source and the tumour by perforating the skin region, and bypassing the melanin absorption. For a fairer comparison in a thermal perspective, the five laser beams were set to produce approximately the same irradiance as the 5 mm beam profile. The simulation output intensity was set to 5% of the so-called unitary source (Fang and Boas 2009b) to maximise the energy deposition in-depth and minimise the skin damage.

Additionally, to ensure approximately the same irradiance at the surface independently of the beam radius considered, the irradiance sum of the beam area of the 5mm laser was computed, and the remaining laser configurations had their irradiance sum of the beam area's increased to match it. *i.e.*, whereas the pencil and 5 mm size flat-top light intensities were set to the same 5% of unitary output, the 10 mm flat-top irradiance was set to 2 times higher, the 20 mm flat-top irradiance was set to 6 times higher and the last 4 cm flat-top irradiance was set to 24 times higher. Estimations for the laser powers simulated are 500 mW, 1.5 W, 5.5 W and 26 W for the 5 mm, 10 mm, 20 mm, and 40 mm laser configurations.

Since this is purely a Monte Carlo simulation method, the irradiation considers the tracking of individual packet photons generated with a given direction and random position. The choice of a flat-top beam allows an evener distribution of the incident irradiance within the beam spot. The beam axis points directly to the centre of the spheroid tumour, and its centre is also placed at the same point in the XY projection plane. The z-axis zero is set at one of the breastplates. Two laser sources were considered on the top and bottom of the breast to increase the tumour's energy absorption further. Each one of the laser sources simulated 10 million photons.

Thermal Conditions Apart from the different irradiation schemes, all the simulations shared common properties for solving the bioheat diffusion equation. These are presented on the right-side and bottom of table 4.2. The time of exposure is set to 120 seconds. The room temperature was set to 23 ^{o}C, and all surfaces transferred convective heat to air using the Newton cooling law with the respective coefficient at 3.4 W $K^{-1}m^{-2}$ (Dear *et al.* 1997). The hyperthermia damage temperature was set to 45 ^{o}C and the time-period to reach necrosis was set to 50 seconds to estimate the tissue damage parameter. These parameters were set to measure the duration of time at which the tissue was exposed to a 45 ^{o}C temperature or higher.

4.3.3 Results

The optical simulation results will first be presented, studying the volumetric heat source (VHS) parameter and the thermal results to present the results and discussion on this case study. Hence, the discussion will be more detailed on what contributed most to the success of the therapy or what can contribute to further the effectiveness of the therapy. For a better visualization and differentiation, the volumetric heat source, the temperature and the damaged tissue indicator parameters will be presented and discussed thoroughly, and will have associated their colour palette.

4.3.3.1 Flat-Top Beam Profiles

The optical simulations of the flat-top beam profiles of radius 5 mm, 10 mm, 20 mm, and 40 mm follow. Figures 4.11 and 4.12 present a close-up view of the decimal logarithm of the volumetric heat source parameter for different beam widths for the lasers located at the bottom (figure 4.11) and top (figure 4.12). All plots show the y=0 plane view, which contains the centre of the GNP sphere and the beam axis.

As expected, the decimal logarithm of the volumetric heat source parameter, shown in figures 4.11 and 4.12, seem symmetrical when comparing equivalent laser irradiation profiles. Independent of the irradiation scheme, the skin region has the highest volumetric heat source parameter (VHS) values at 10^6 W m^{-3}. The spheroid region seems to have a temperature increase at its surface due to the presence of gold nanoparticles, although not higher than the temperature increase at the skin. Additionally, there is a lack of VHS present in the centre of the spheroid compared to the same deepness outside the GNP region, which indicates that most of the light that reaches the sphere is absorbed in the GNP surface. This result can lead to less temperature increase in the centre with increasing beam widths.

When comparing the VHS of the different irradiation configurations, one sees that the larger the beamwidth, the larger the VHS increase in the sphere. The volumetric heat generated by a single source of 5 mm in radius can be considered roughly the same as the light out of an optical fibre. From the first plots of figures 4.11 and 4.12, one can see that the volumetric heat as a function of depth is two orders of magnitude lower when comparing the skin surface from the GNP-filled tumour at the surface, distanced by 1 cm.

Figure 4.13 presents a close-up view at the y=0 plane of the sum of the decimal logarithm of the volumetric heat source parameter of the four beam widths, presented in figures 4.12 and 4.11. The increase in VHS with beam width is obvious, considering equal incident irradiances for all the different configurations.

Comparing all images shown in figures 4.11, 4.12 and 4.13, the one where the volumetric heat source parameter is the largest in the GNP region is the one that shows the 40 mm beam width laser configuration with the sum of the two sources top and bottom, even though the skin takes the largest VHS dosage, presented in the fourth image of figure

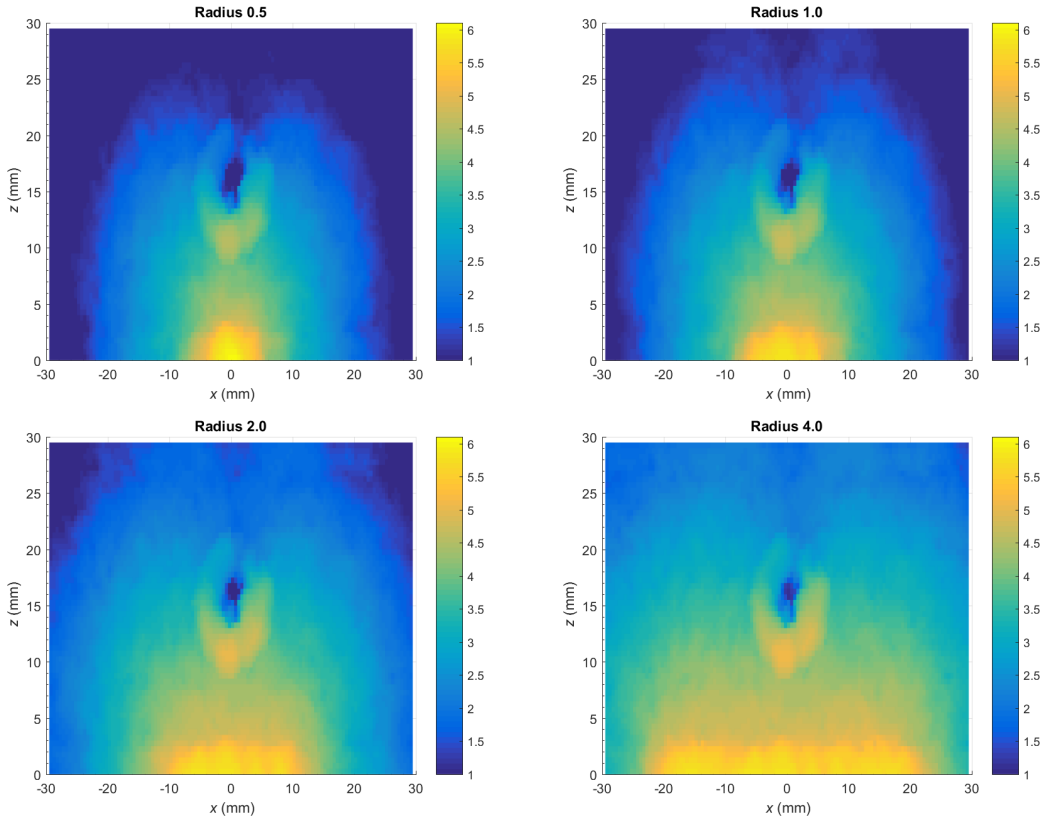

Figure 4.11: Decimal logarithm of the volumetric heat source (VHS) generated by one flat-top light source located at the bottom of the breast. The top-left image portrays the decimal logarithm of the VHS planar source of half the size of the GNP sphere (5 mm). The top-right, bottom-left and bottom-right present the same information considering a planar source of the same size, twice as large and fourth times as large as the GNP sphere. This figure portrays a zoom of the y=0 plane of the mesh presented in 4.8.

4.13. The VHS output of this configuration was used as input to solve the Pennes bioheat equation, and its output is discussed in the next paragraphs.

Temperature Determination In this subsection, the temperature increase recorded in two digital phantoms, with and without skin tissue thermal properties, labelled as *breast* and *slab* digital phantoms, respectively, is presented. Figure 4.14 shows the temperature change of the flat-top dual-laser configuration of 40 mm beamwidth. The *breast* mesh is on top, and the bottom, the *slab* mesh. Both images on this figure show a cross-sectional view at the y=0 plane, which contains the centre of the spheroid GNP-tumour region and beam axis the second before the lasers were turned off. The top image shows the temperature change results of the laser configuration when one considers the *breast* mesh with homogeneous breast thermal properties. Tthe bottom image shows the temperature change results of the same laser configuration where the *slab* mesh with three independent homogeneous regions is considered. Two of the three independent regions share the same

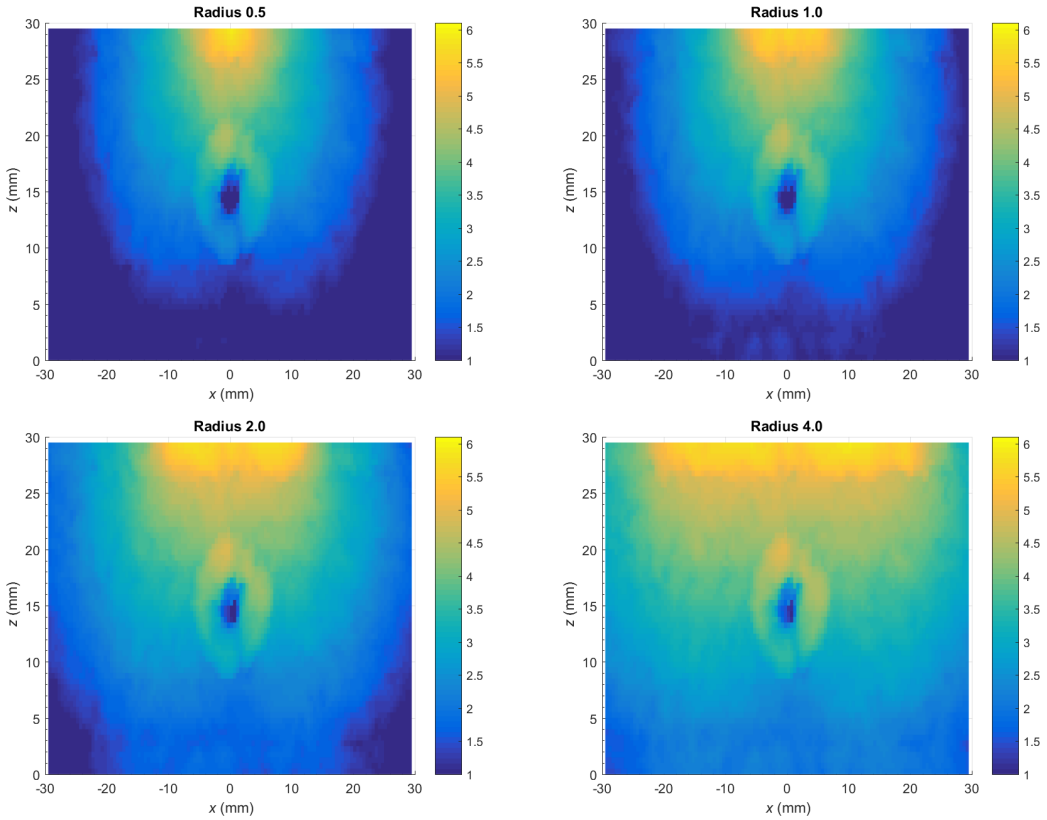

Figure 4.12: Decimal logarithm of the volumetric heat source (VHS) generated by one planar light source located at the top of the breast mesh. The top-left image portrays the decimal logarithm of the VHS planar source of half the size of the GNP sphere (5 mm). The top-right, bottom-left and bottom-right present the same information considering a planar source of the same size, twice as large and fourth times as large as the GNP sphere. This figure portrays a zoom of the y=0 plane of the digital phantom presented in 4.8.

skin thermal properties, as shown in figure 4.9. When one considers only the *breast* mesh, the temperature increase generated by light-absorbing nanoparticles is no more than 5 ^{o}C, and the temperature increase at the skin is at most 14 ^{o}C. When one considers the temperature change in the *slab* mesh at the skin region, its value is at most 5 ^{o}C, and in the spheroid's centre is at most 2 ^{o}C.

When comparing both plots in figure 4.14, one can conclude that skin addition decreases the temperature change of the impinging laser light and the GNP region.

Figure 4.15 is presented to predict temperature increase across some reference points inside the phantom if one considers extending the irradiation time. This figure shows the temperature change versus time for three separate points contained by the beam axis on both images. This figure shows the temperature change versus time for three separate points contained by the beam axis on both images, at z=0 mm on the skin surface, at z=10 mm on the spheroid GNP-tumour surface, and z=15 mm at the spheroid's centre. The top image of figure 4.15 presents the data of temperature increase versus time from

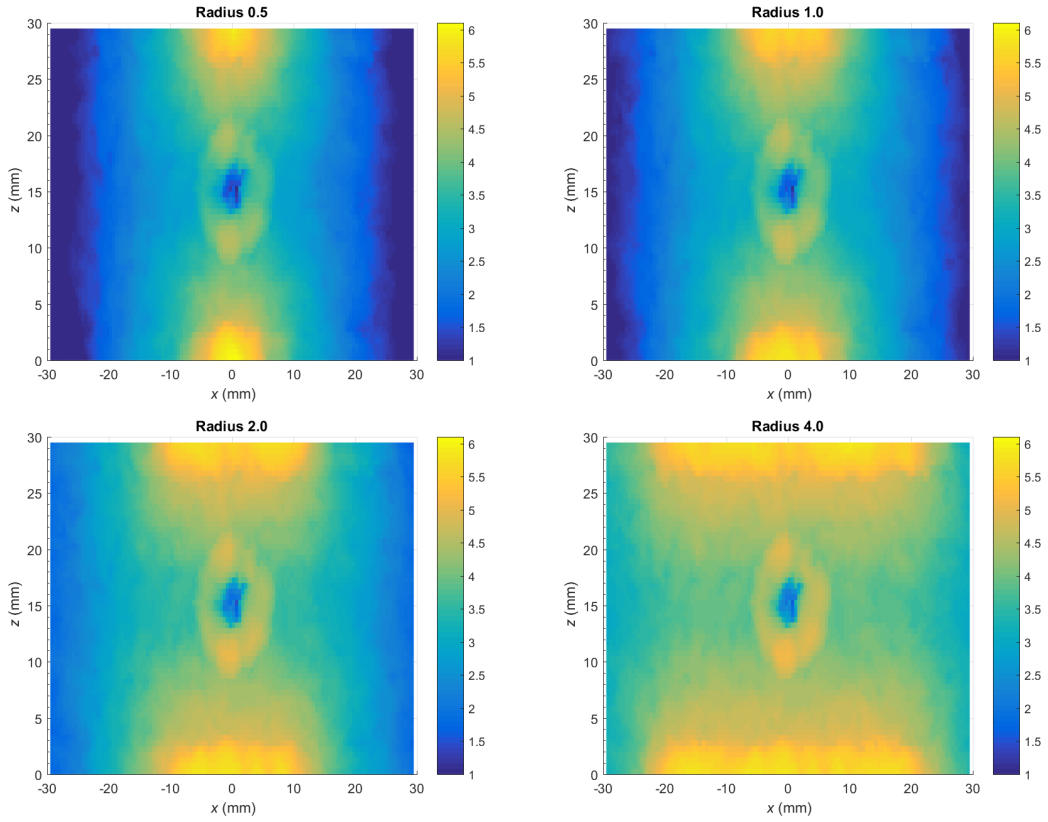

Figure 4.13: Decimal logarithm of the volumetric heat source (VHS) generated by the sum of two planar light sources located at the top and bottom of the *breast* mesh. The top-left image portrays the decimal logarithm of the VHS planar source of half the size of the GNP sphere (5 mm), the top-right, bottom-left and bottom-right present the same information considering a planar source of the same size, twice as large and fourth times as large as the GNP sphere, respectively. This figure portrays a cross-sectional view of the y=0 plane of the digital phantom presented in figure 4.8.

the *breast* mesh, while the bottom image presents the same data for the *slab* mesh. The temperature increase shown in these images suggests that given a more prolonged laser exposure, the skin would take more damage than the GNP breast tissue, while at the centre and surface of the tumour, the difference in temperature change would be almost insignificant comparatively.

Damage Estimation The damage caused by a temperature increase in both digital phantoms can be seen in figure 4.15. The top and bottom images present the damage tissue indicator for the *breast* and *slab* meshes. As one can expect, the top image's temperature damage is enough as the temperature increases to more than 50 ^{o}C. The damage tissue indicator presents some residual damage in the skin region in the bottom image because the hyperthermia damage temperature has just been reached at those sites.

From an optical irradiation and simulation perspective, the flat-top beam profile

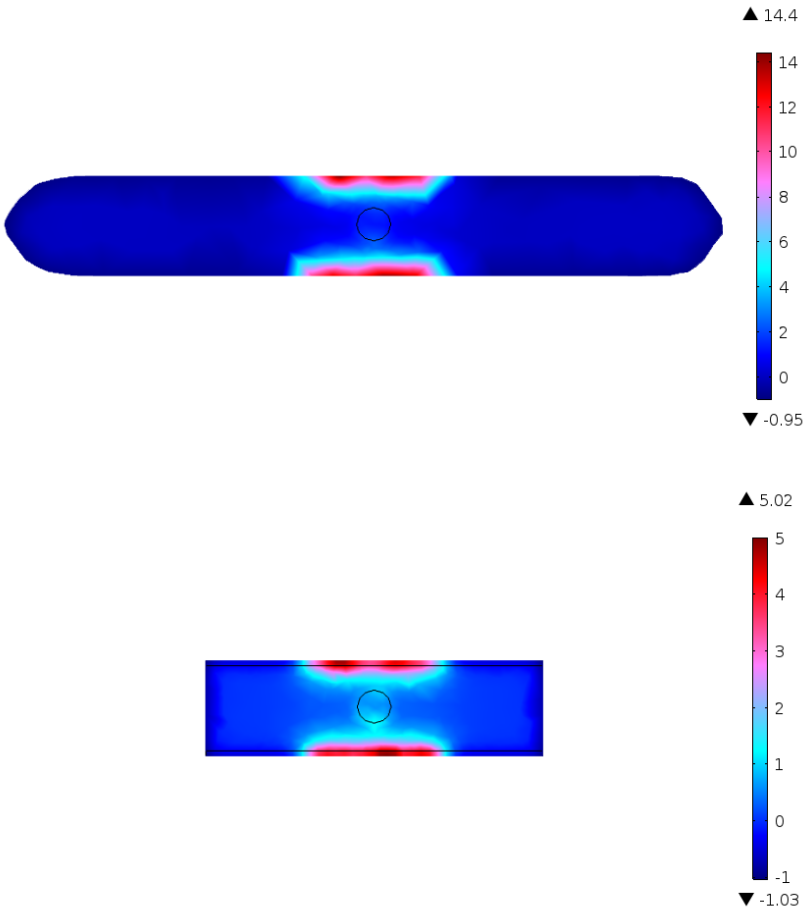

Figure 4.14: Top: temperature change of the *breast* mesh, composed only of breast thermal properties. Bottom: temperature change of the *slab* mesh, where the breast and the skin thermal properties are considered. These temperatures were determined using the planar light source, which was four times the size of the GNP sphere.

chosen is the better option to increase the temperature in a given region of interest deep inside the breast tissue. The results and conclusions presented from figures 4.14, 4.15 and 4.16 suggest that this laser source configuration is not enough to provide a therapeutic temperature increase in the tumour site 1 cm below the skin surface while at the same time maintaining healthy tissue free of thermal damage, even when considering extending the therapy's duration in time.

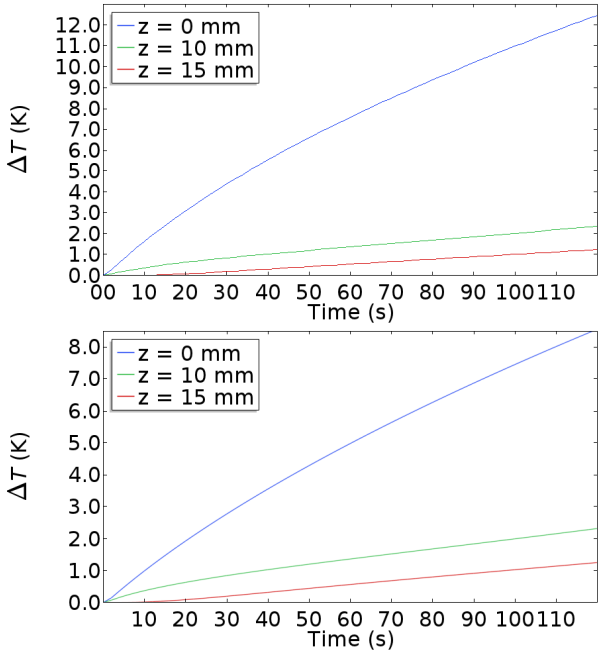

Figure 4.15: Temperature increase during the laser irradiation phase with a 4 cm flat-top beam profile at three different positions contained in the beam axis: (0, 0, 0) mm the skin surface, (0, 0, 10) mm at the spheroid's surface and (0, 0, 15) mm in its centre. The top image presents temperature change in time for the *breast* mesh, while the bottom image presents the same data for the *slab* mesh.

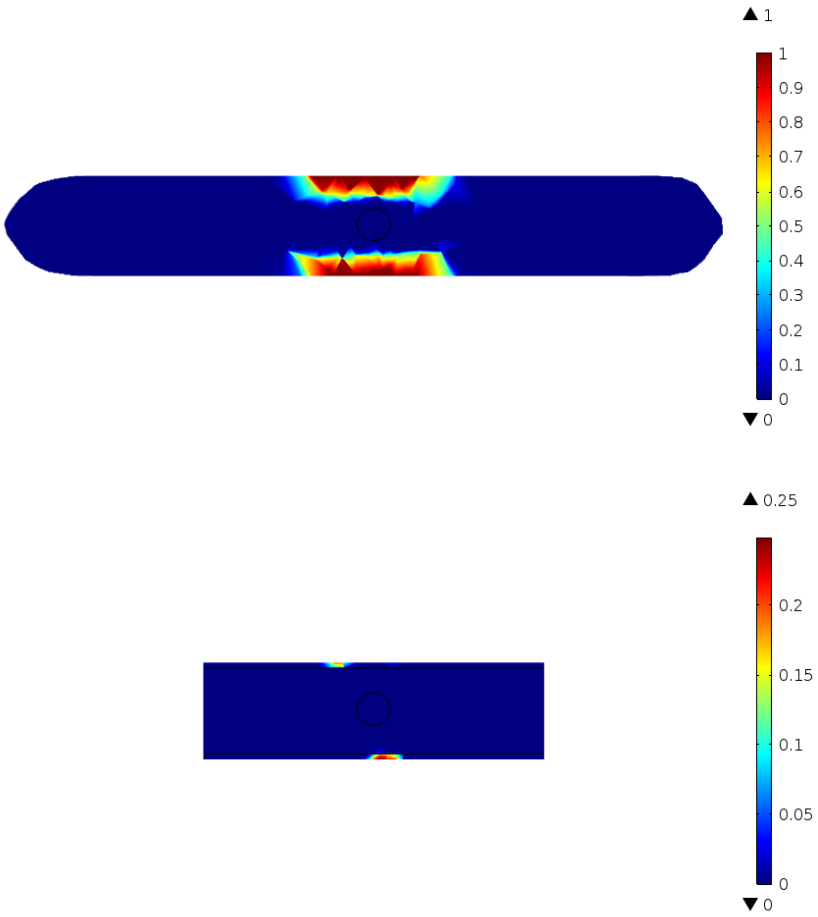

Figure 4.16: Damaged tissue indicator for the *breast* (top) and *slab* (bottom) digital phantoms considering the 40 mm flat-top beamwidth. These images present a zoomed view of the y=0 plane.

4.3.3.2 Pencil Light Sources

To further decrease the distance between the light source and the region of interest, it was supposed that the laser fibre could pierce through the skin, damaging it lightly but putting it closer to the tumour. The profile of the light sources was considered to be a pencil beam. The light source is placed at 2 mm after the breastplates, making the distance between the tumour and the sources 8 mm. The power of each light source is 50 mW. The same optical and thermal properties presented in table 4.2 are used and the same digital breast phantoms.

Figure 4.17 shows a close-up view at y=0 of the volumetric heat source parameter's decimal logarithm, generated by the sum of the two light sources placed at the top and bottom of the breast after the skin layer. These values of VHS are somewhat comparable to the ones presented in the fourth image of figure 4.13 when one considers the VHS in the spheroid, but at the same time reducing the light absorption in the healthy skin surface to a smaller area.

Temperature Determination Figure 4.18 presents the temperature change caused by the pencil laser irradiation that lasted 120 seconds. Here are shown cross-sectional views at the y=0 plane, where the centre of the tumour-GNP region and the beam axis is contained. The top image presents the temperature change results of the simulations in the *breast* mesh, while at the bottom is considered the *slab* mesh. Additionally, in figure 4.19 the temperature change as a function of time at three different positions in the beam axis is presented. z=0 mm, which is at the skin surface and behind the light source, z=10 mm at the spheroid's surface and z=15 mm, which is at the spheroid's centre. The top image presents temperature change in time for the *breast* mesh, while the bottom image presents the same data for the *slab* mesh.

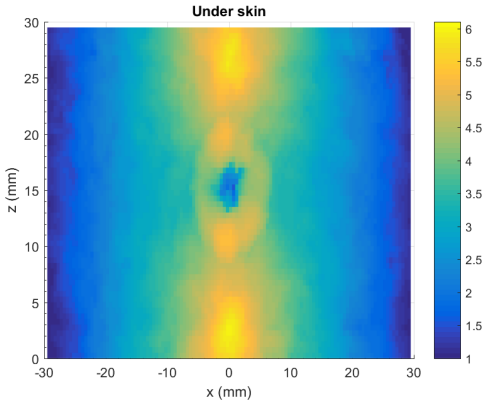

Figure 4.17: Decimal logarithm of the volumetric heat source (VHS) generated by the sum of two pencil beam light sources located at the top and bottom of the breast mesh, after the skin layer. This figure portrays a zoom of the y=0 plane of the digital phantom presented in 4.8.

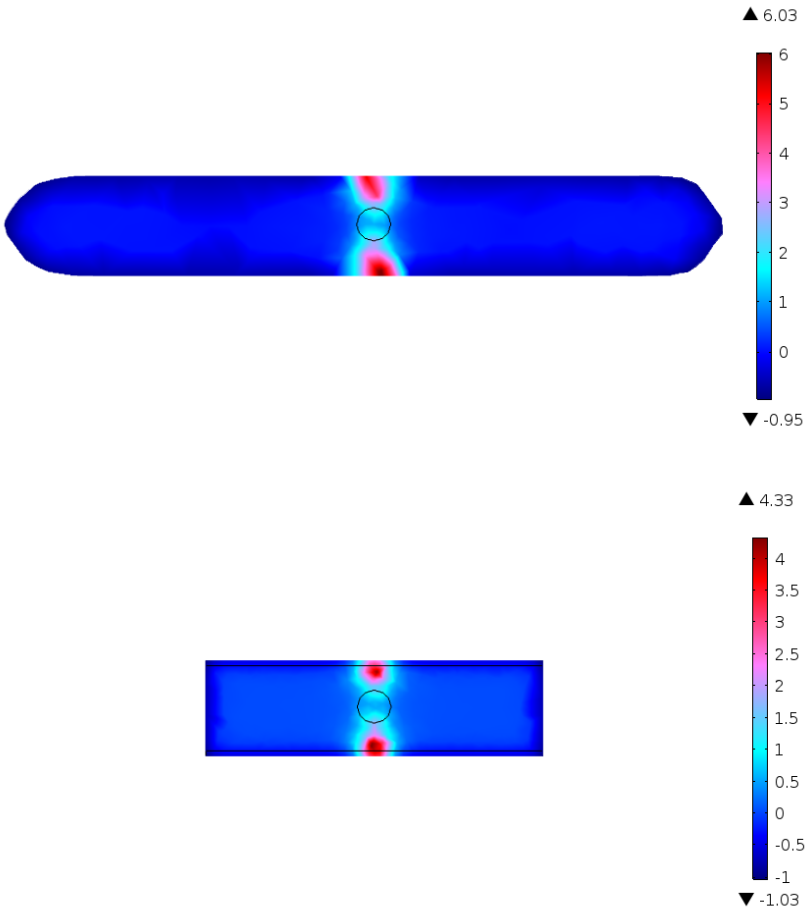

Figure 4.18: Top: temperature change of the breast mesh, composed only of *breast* thermal properties. Bottom: temperature change of the *slab* mesh, where the breast and the skin thermal properties are considered. These temperatures were determined using the light source positioned after the skin layer.

These results show that the temperature increase in the *breast* mesh is comparable to the ones presented in the *slab* mesh. By placing the laser source after the skin layer, its properties do not significantly increase in temperature as in the previous irradiation scheme. Additionally, the temperature change inside the spheroid is larger due to the proximity of the laser source. As one can see in the temperature increase over time shown in figure 4.19, if the laser exposure is longer than the current exposure, the skin would collect more heat rather than the region of interest.

Damage Estimation The damage tissue indicator parameter for the *breast* mesh and the *slab* mesh is presented in figure 4.20, on the top and bottom images, respectively. The temperature registered in the *slab* mesh did not reach the 45 ^{o}C (+8 ^{o}C). Thus, there is no recorded damage. On the other hand, the *breast* mesh does record some damage at the skin region behind the laser, but none recorded in the tumour region of interest.

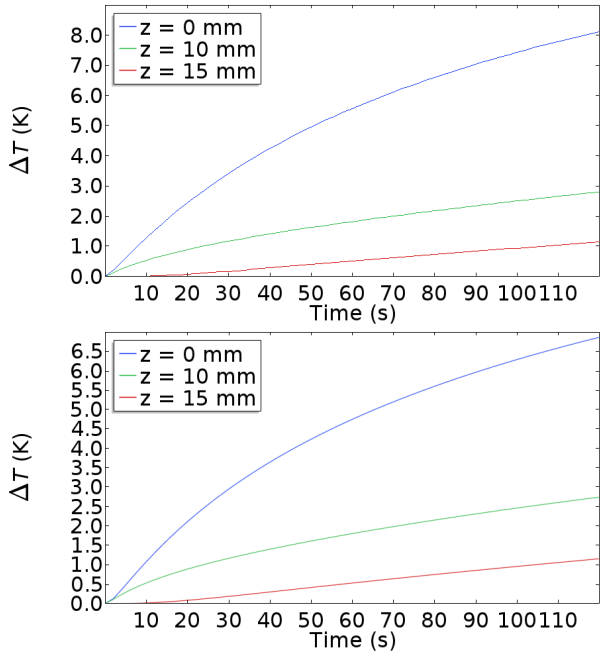

Figure 4.19: Temperature increase during the laser irradiation phase with the pencil beam at three different positions contained in the beam axis. The results for the temperature increase as a function of time at (0, 0, 0) mm the skin surface is shown in blue, (0, 0, 10) mm at the spheroid's surface shown in green and (0, 0, 15) mm in its centre shown in red, respectively. The top image presents temperature change in time for the *breast* mesh, while the bottom image presents the same data for the *slab* mesh.

Extending the therapy in time will achieve some damage in the region of interest, but first will damage healthy tissue, as one could predict from the temperature increase as a function of time shown in figure 4.19.

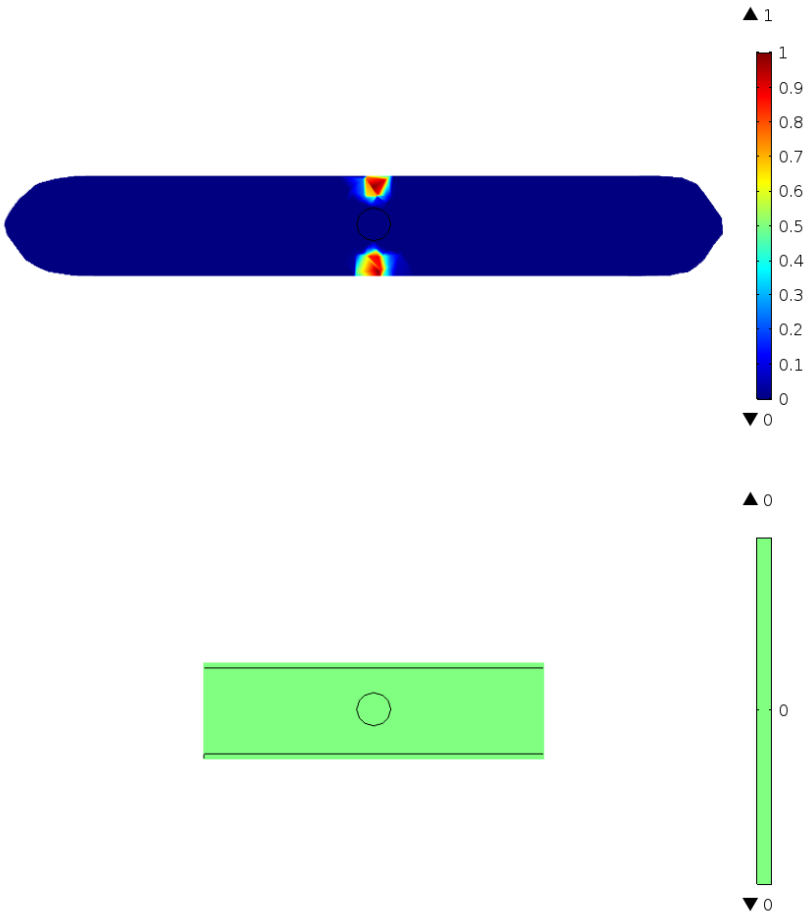

Figure 4.20: Damaged tissue indicator for the *breast* (top) and *slab* (bottom) meshes considering the irradiation pencil beam profile. These images present a zoomed view of the y=0 plane.

4.4 CHAPTER CONCLUSION

Photothermal numerical simulations allow within a reasonable degree of accuracy and precision to predict the therapy's success without performing experiments on tissue *in-vivo* or *ex-vivo*. This chapter presented the results and discussions on three protocols developed in the previous chapters. The three protocols are: to determine optical properties of highly scattering samples, to design and produce heterogeneous optical breast phantoms and a protocol to model the numerical simulation of photothermal therapy in biological tissue, from the irradiation phase until the damage phase, which included the use of several different software. An experiment was designed with optical properties similar to some studies already tackled by this community but considering an inclusion that is more realistic than the ones already reported by other authors. The produced phantom had two goals: validating a numerical model and compare results with previous authors. To numerically model this experiment, the diffusion approximation and Monte Carlo simulations were considered to determine the fluence rate inside the phantom, convert it to temperature with the appropriate numerical methods, and compare it to the measured experimental data. In contrast, Monte Carlo simulations have a better average percentage difference and a high Pearson correlation coefficient with experimental data. Monte Carlo simulations have fewer restrictions, which results in a better performance compared to the diffusion approximation. The results show that by defining a tumour up to 1 cm thick, instead of two regions without and with a cylinder region of 4 cm thick gold nanoparticles, the temperature increase is lower than those reported in those other studies.

Additional numerical simulations were performed on a 3 cm thick compressed breast digital phantom with a 1 cm spherical tumour at its centre. This phantom had assigned to the appropriate regions the optical properties of nanoparticles added to tumour breast tissue, skin tissue and homogeneous breast tissue with average optical properties. The simulation protocol determined the fluence rate, the volumetric heat source, the temperature and damage tissue indicator parameters. Some novel features can be considered when comparing this to other simulations performed by several authors, namely the inclusion of skin, using a compressed breast to minimise the distance between the surface and the tumour region, and irradiating the phantom with different beam profiles and positions. By including the skin tissue in the numerical analysis, the temperature and thermal damage at the surface is significantly reduced when considering the optical and thermal standpoints. When considering the same irradiance and different irradiation schemes, different but comparable light absorption rates can be seen at the desired site.

The results show a high dependence of the therapy's success on the tissues' optical properties and the tumour's distance. The highest concentration of gold nanoparticles that were reported in the community was considered homogeneously across the tumour. Most healthy skin tissue shows a higher temperature increase than the tumour region of interest, independent of the different irradiation schemes considered. Additionally, the

tumour region in any of these laser configurations did not have a temperature increase that was even throughout its volume.

The results presented in this chapter lead to the conclusion that, from only considering the optical standpoint, this version of photothermal therapy is not robust to the point that can be applied alone in any case with certain success. Other considerations must be regarded if one wants to successfully use this photothermal therapy to lower the temperature at the healthy skin tissue.

Chapter 5

Conclusions

In this thesis was studied the optical side of photothermal therapy in breast cancer using gold nanoparticles. The emphasis of this study was to report its effectiveness by controlling the optical side of the therapy, by changing the light delivery, and not so much on the thermal due to the known fact that this therapy is highly dependent on the optical properties of breast tissue. Four protocols were developed along with several experiments and simulation studies to tackle this issue, which will be detailed in the next paragraphs.

A first protocol was developed to measure the optical properties of biological tissue, namely the absorption and scattering coefficients. Previous works (Elliott *et al.* 2007; Elliott *et al.* 2009) measured the total attenuation of the tissue and calculated the resulting absorption and scattering properties using the Mie theory (Bohren and Huffman 1983). A INO® optical phantom was characterised by two different methods, the company's setup and the developed protocol. This validation provided a reasonable estimate for the scattering properties with an associated uncertainty of 7 %. The absorption uncertainty value, as expected, was comparable to the measurement value.

A second protocol was developed to determine the tissue damage numerically due to light exposure. This protocol determines the fluence rate of a non-uniform 3D biological sample explicitly using one of two possible models: the diffusion approximation method or the Monte Carlo method. The computed fluence rate is used to determine the local heat increase due to the absorption of light and the temperature at each space-time point. The temperature change obtained through the two different optical methods are compared. An additional step is considered to determine thermal damage using the accumulation of heat and time of exposure. A final protocol discussed the most appropriate components and production method to develop an optical phantom which would mimic most closely the breast tissue's optical properties. An optical phantom with an inclusion of 9 mm, 5 mm away from the surface was produced, and a photothermal experiment was conducted.

This phantom was irradiated for 12 minutes, and the temperature was measured close to the inclusion. The two numerical models assessed to study this case, Monte Carlo and the diffusion approximation, were coupled with the classical heat diffusion equation to estimate the temperature and compare with experimental data. Results show that the Monte Carlo simulations outperform the diffusion approximation in this case. The average percentage difference of the Monte Carlo and diffusion approximation compared to the experimental data was 4.5% and 61%, while the Pearson correlation coefficient between the same datasets was 0.98 and 0.95, respectively. Additionally, radial temperature distribution studies show that Monte Carlo simulations present an adequate profile to what is expected.

Additional numerical simulations were considered using a compressed breast geometry and several irradiating schemes to increase the energy absorption in a tumour. Average optical properties were considered for the skin and breast tissue. The tumour was placed at the centre of the breast and filled with nanoparticles, leading to an increase in the region's optical properties. The simulation protocol determined the volumetric heat, temperature and estimation of thermal damage. Some novel features were considered when comparing this to other studies, namely skin and the implementation of several different irradiation schemes, using a compressed breast to minimise the distance between the surface and the tumour region, and using the Pennes bioheat equation. The temperature increase registered at the surface was higher than in the tumour independently of the irradiation scheme considered. Concluding, there is a clear dependence of the success of the therapy to the optical properties, distance and size of the tumour. Other considerations must be included to increase the therapy's effectiveness.

5.1 Limitations

Three main limiting factors bind this research work. The results show that the skin tissue absorbs most of the light, and the nanoparticles absorb a small amount. This approach of photothermal therapy can only be applied in the treatment of a small number of cases where the optical tissue properties are favourable to this therapy.

The setup to measure the absorption coefficient needs further improvement to mitigate the laser fluence rate and inhomogeneous scattering of the integrating sphere, which due to the low absorption of the samples, increase their significance on the measurement.

Even though the used temperature measurement setup allowed the study of treatment viability, 2D thermometry information would help discuss these studies' results and provide more exciting conclusions.

5.2 Future work

When considering viable paths for future work based on the developments described in this thesis, incremental improvements should be considered for specific components.

- The tissue attenuation plays a significant role in the selective heating of tissue while maintaining healthy tissue free of thermal damage. By decreasing the distance between the source and the tumour by placing the laser in the tumour's vicinity, the therapy's effectiveness could be increased.
- Lower the temperature at the skin surface in order to increase the heat inside the digital phantom, possibly with the use of thermoregulator skin cold sprays, taking into account the work developed in (Diller 2010), or even by immersing the compressed breast in a cooling liquid with the same refractive index as the skin.
- Incorporate a 2D or 3D temperature measurement technique such as ultrasound thermometry or magnetic resonance temperature imaging to measure the temperature in-depth with less than 1 mm in spatial resolution. The importance of measuring the correct temperature inside the tissue, demands knowing the tissue structures and vascularisation to estimate the temperature correctly, especially in large blood vessels and tumours close to the surface.
- The use of bovine protein could help estimate internal thermal damage in the phantom's region of interest with histologic studies.
- Implementing a technique to measure optical tissue properties, such as quantitative photoacoustic tomography, could allow live measurements of the change in optical properties due to cell damage.

Bibliography

Abadeer, N. S. and C. J. Murphy (2016). "Recent Progress in Cancer Thermal Therapy Using Gold Nanoparticles." In: *Journal of Physical Chemistry C* 120.9, pp. 4691–4716. DOI: 10.1021/acs.jpcc.5b11232.

Alerstam, E (2011). "Optical spectroscopy of turbid media: time-domain measurements and accelerated Monte Carlo modelling." Thesis. ISBN: 9789174732030. DOI: 978-91-7473-203-0.

Alphandéry, E. (2014). "Perspectives of Breast Cancer Thermotherapies." In: *Journal of Cancer* 5.6, pp. 472–479. DOI: 10.7150/jca.8693.

Arridge, S. R. (1999). "Optical tomography in medical imaging Inverse Problems." In: *Inverse Problems* 15.2, R41–R93. DOI: 10.1088/0266-5611/15/2/022.

Arridge, S. R. and J. C. Schotland (2009). "Optical tomography: Forward and inverse problems." In: *Inverse Problems* 25.12. DOI: 10.1088/0266-5611/25/12/123010.

Aydin, E. D., C. R. de Oliveira, and A. J. Goddard (2004). "A finite element-spherical harmonics radiation transport model for photon migration in turbid media." In: *Journal of Quantitative Spectroscopy and Radiative Transfer*. DOI: 10.1016/S0022-4073(03)00180-8.

Baetke, S. C., T. Lammers, and F. Kiessling (2015). "Applications of nanoparticles for diagnosis and therapy of cancer." In: *British Journal of Radiology* 88.1054. DOI: 10.1259/bjr.20150207. arXiv: arXiv:1011.1669v3.

Beer (1852). "Bestimmung der Absorption des rothen Lichts in farbigen Flüssigkeiten." In: *Annalen der Physik und Chemie* 162.5, pp. 78–88. DOI: 10.1002/andp.18521620505.

Bhowmik, A., R. Singh, R. Repaka, and S. C. Mishra (2013). "Conventional and newly developed bioheat transport models in vascularized tissues: A review." In: *Journal of Thermal Biology* 38.3, pp. 107–125. DOI: 10.1016/j.jtherbio.2012.12.003.

Binzoni, T, T. S. Leung, A. H. Gandjbakhche, D Rüfenacht, and D. T. Delpy (2006). "The use of the Henyey–Greenstein phase function in Monte Carlo simulations in biomedical optics." In: *Physics in Medicine and Biology* 51.17, N313–N322. DOI: 10.1088/0031-9155/51/17/N04.

Bohren, C. F. and D. R. Huffman (1983). *Absorption and scattering of light by small particles*. Ed. by C. F. Bohren and D. R. Huffman. Weinheim, Germany: Wiley Science Paperback Series. ISBN: 9783527406647. DOI: 10.1088/0031-9112/35/3/025.

Bouchard, J.-P., I. Veilleux, R. Jedidi, I. Noiseux, M. Fortin, and O. Mermut (2010). "Reference optical phantoms for diffuse optical spectroscopy Part 1 – Error analysis of a time resolved transmittance characterization method." In: *Optics Express* 18.11, p. 11495. DOI: 10.1364/OE.18.011495.

Brunetaud, J. M., S. Mordon, V. Maunoury, and C. Beacco (1995). "Non-PDT Uses of lasers in oncology." In: *Lasers In Medical Science* 10.1, pp. 3–8.

Cain, C. P. and A. J. Welch (1974). "Thin-Film Temperature Sensors for Biological Measurements." In: *IEEE Transactions on Biomedical Engineering* BME-21.5, pp. 421–423. DOI: 10.1109/TBME.1974.324415.

Caplan, L. (2014). *Delay in breast cancer: Implications for stage at diagnosis and survival*. DOI: 10.3389/fpubh.2014.00087.

Chandrasekhar, S (1960). *The Equation of Transfer*. ISBN: 0486605906.

Chanmugam, A., R. Hatwar, and C. Herman (2012). "Thermal Analysis of Cancerous Breast Model." In: *Volume 2: Biomedical and Biotechnology*. Vol. 71. 11. American Society of Mechanical Engineers, pp. 135–143. DOI: 10.1115/IMECE2012-88244. arXiv: NIHMS150003.

Chen, J., Q. Fang, and X. Intes (2012). "Mesh-based Monte Carlo method in time-domain widefield fluorescence molecular tomography." In: *Journal of Biomedical Optics* 17.10, p. 1060091. DOI: 10.1117/1.JBO.17.10.106009.

Cheong, S. S.-K., S. Krishnan, and S. H. Cho (2008). "Modeling of Plasmonic Heating From Individual Gold Nanoshells for Near-Infrared Laser-Induced Thermal Therapy." In: *Medical Physics* 35.6, pp. 4664–4671. DOI: 10.1118/1.2961677.

Cheong, W., S. Prahl, and A. Welch (1990). "A review of the optical properties of biological tissues." In: *IEEE Journal of Quantum Electronics* 26.12, pp. 2166–2185. DOI: 10.1109/3.64354.

Cho, S., A. Siddiqi, and N. Manohar (2010). "Induction of Plasmonic Heating Inside Breast Tumor Phantom Using Gold Nanorods and Near-Infrared Laser." In: *Medical Physics* 37.6Part11, pp. 3172–3172. DOI: 10.1118/1.3468343.

Dabbagh, A., B. J. J. Abdullah, C. Ramasindarum, and N. H. Abu Kasim (2014). "Tissue-mimicking gel phantoms for thermal therapy studies." In: *Ultrasonic Imaging* 36.4, pp. 291–316. DOI: 10.1177/0161734614526372.

Dai, X., T. Li, Z. Bai, Y. Yang, X. Liu, J. Zhan, and B. Shi (2015). "Breast cancer intrinsic subtype classification, clinical use and future trends." In: *American journal of cancer research* 5.10, pp. 2929–43.

Das, K. and S. C. Mishra (2013). "Estimation of tumor characteristics in a breast tissue with known skin surface temperature." In: *Journal of Thermal Biology* 38.6, pp. 311–317. DOI: 10.1016/j.jtherbio.2013.04.001.

Dear, R. J. de, E. Arens, Z. Hui, and M. Oguro (1997). "Convective and radiative heat transfer coefficients for individual human body segments." In: *International Journal of Biometeorology* 40.3, pp. 141–156. DOI: 10.1007/s004840050035.

Deng, B., D. H. Brooks, D. A. Boas, M. Lundqvist, and Q. Fang (2015). "Characterization of structural-prior guided optical tomography using realistic breast models derived from dual-energy x-ray mammography." In: 6.7, pp. 2366–2379. DOI: 10.1364/BOE.6.002366.

Di Ninni, P., F. Martelli, and G. Zaccanti (2010). "The use of India ink in tissue-simulating phantoms." In: *Optics Express* 18.26, p. 26854. DOI: 10.1364/OE.18.026854.

Diller, K. R. (2010). "Laser Generated Heat Transfer." In: *Optical-Thermal Response of Laser-Irradiated Tissue*. Dordrecht: Springer Netherlands, pp. 353–397. DOI: 10.1007/978-90-481-8831-4_10.

ECIS (2019). *Cancer burden statistics and trends across Europe*. URL: https://ecis.jrc.ec.europa.eu/ (visited on 05/31/2019).

Elliott, A. M., R. J. Stafford, J. Schwartz, J. Wang, A. M. Shetty, C. Bourgoyne, P. O'Neal, and J. D. Hazle (2007). "Laser-induced thermal response and characterization of nanoparticles for cancer treatment using magnetic resonance thermal imaging." In: *Medical Physics* 34.7, pp. 3102–3108. DOI: 10.1118/1.2733801.

Elliott, A. M., J. Schwartz, J. Wang, A. M. Shetty, C. Bourgoyne, D. P. O'neal, J. D. Hazle, R. J. Stafford, D. P. O. Neal, D John, R. J. Stafford, J. Schwartz, J. Wang, D. P. O'neal, J. D. Hazle, and R. J. Stafford (2009). "Quantitative comparison of delta P1 versus optical diffusion approximations for modeling near-infrared gold nanoshell heating." In: *Medical Physics* 36.4, pp. 1351–1358. DOI: 10.1118/1.3056456.

Fang, Q. (2010). "Mesh-based Monte Carlo method using fast ray-tracing in Plücker coordinates." In: *Biomedical Optics Express* 1.1, p. 165. DOI: 10.1364/BOE.1.000165.

Fang, Q. and D. a. Boas (2009a). "Monte Carlo simulation of photon migration in 3D turbid media accelerated by graphics processing units." In: *Optics express* 17.22, pp. 20178–20190. DOI: 10.1364/OE.17.020178.

— (2009b). "Monte Carlo simulation of photon migration in 3D turbid media accelerated by graphics processing units." In: *Optics express* 17.22, pp. 20178–20190. DOI: 10.1364/OE.17.020178.

Fang, Q. and D. A. Boas (2009c). "Tetrahedral mesh generation from volumetric binary and grayscale images." In: *Proceedings - 2009 IEEE International Symposium on Biomedical Imaging: From Nano to Macro, ISBI 2009* Isbi, pp. 1142–1145. DOI: 10.1109/ISBI.2009.5193259.

Fang, Q. and D. R. Kaeli (2012). "Accelerating mesh-based Monte Carlo method on modern CPU architectures." In: *Biomedical Optics Express* 3.12, p. 3223. DOI: 10.1364/BOE.3.003223.

Fang, Q. *MMC slab problem report*. URL: http://iso2mesh.sourceforge.net/cgi-bin/index.cgi?Doc/FAQ (visited on 03/17/2020).

Ferlay, J, E Steliarova-foucher, J Lortet-tieulent, and S Rosso (2013). "Cancer incidence and mortality patterns in Europe : Estimates for 40 countries in 2012." In: *European Journal of Cancer* 49.6, pp. 1374–1403. DOI: 10.1016/j.ejca.2012.12.027.

Ferlay, J., M. Colombet, I. Soerjomataram, T. Dyba, G. Randi, M. Bettio, A. Gavin, O. Visser, and F. Bray (2018). "Cancer incidence and mortality patterns in Europe: Estimates for 40 countries and 25 major cancers in 2018." In: *European Journal of Cancer* 103, pp. 356–387. DOI: 10.1016/J.EJCA.2018.07.005.

Geuzaine, C. and J.-F. Remacle (2009). "Gmsh: a three-dimensional finite element mesh generator with built-in pre-and post-processing facilities." In: *International Journal for Numerical Methods in Engineering 79(11)* 0, pp. 1309–1331. DOI: 10.1002/nme.2579. arXiv: 1010.1724.

Giacometti, P. and S. G. Diamond (2013). "Diffuse Optical Tomography for Brain Imaging: Continuous Wave Instrumentation and Linear Analysis Methods." In: *Optical Methods and Instrumentation in Brain Imaging and Therapy*. New York, NY: Springer New York, pp. 57–85. DOI: 10.1007/978-1-4614-4978-2_3.

Gibson, A. P., J. C. Hebden, and S. R. Arridge (2005). "Recent advances in diffuse optical imaging." In: *Physics in medicine and biology* 50.4, R1–R43. DOI: 10.1088/0031-9155/50/4/R01.

Glaser, A. K., S. C. Kanick, R. Zhang, P. Arce, and B. W. Pogue (2013). "A GAMOS plug-in for GEANT4 based Monte Carlo simulation of radiation-induced light transport in biological media." In: *Biomedical optics express* 4.5, pp. 741–59. DOI: 10.1364/BOE.4.000741.

Gratton, E. and S. Fantini (2007). "Reflectance and transmittance spectroscopy." In: DOI: 10.1039/9781847551207-00211.

Guo, Z. and S. Kumar (2002). "Three-Dimensional Discrete Ordinates Method in Transient Radiative Transfer." In: *Journal of Thermophysics and Heat Transfer* 16.3, pp. 289–296. DOI: 10.2514/2.6689.

Haemmerich, D., D. J. Schutt, I. Dos Santos, J. G. Webster, and D. M. Mahvi (2005). "Measurement of temperature-dependent specific heat of biological tissues." In: *Physiological Measurement* 26.1, pp. 59–67. DOI: 10.1088/0967-3334/26/1/006.

Hasgall, P. A., E Neufeld, M. C. Gosselin, A Klingenböck, and N Kuster (2015). "IT'IS Database for thermal and electromagnetic parameters of biological tissues." In: *Version*.

Haskell, R. C., L. O. Svaasand, T.-T. Tsay, T.-C. Feng, B. J. Tromberg, and M. S. McAdams (1994). "Boundary conditions for the diffusion equation in radiative transfer." In: *Journal of the Optical Society of America A* 11.10, p. 2727. DOI: 10.1364/JOSAA.11.002727.

Henyey, L. C. and J. L. Greenstein (1941). "Diffuse radiation in the Galaxy." In: *The Astrophysical Journal* 93, p. 70. DOI: 10.1086/144246.

Hesthaven, J. S. and T. Warburton (2008). *Nodal Discontinuous Galerkin Methods*. Vol. 54. 2, pp. 127–41. DOI: 10.1007/978-0-387-72067-8. arXiv: arXiv:0901.1024v3.

Hirsch, L. R., R. J. Stafford, J. A. Bankson, S. R. Sershen, B. Rivera, R. E. Price, J. D. Hazle, N. J. Halas, and J. L. West (2003). "Nanoshell-mediated near-infrared thermal therapy of tumors under magnetic resonance guidance." In: *Proceedings of the National*

Academy of Sciences 100.23, pp. 13549–13554. DOI: 10.1073/pnas.2232479100. arXiv: 0008204 [cond-mat].

Huppert, T. J. (2013). "History of Diffuse Optical Spectroscopy of Human Tissue." In: *Optical Methods and Instrumentation in Brain Imaging and Therapy*. New York, NY: Springer New York, pp. 23–56. DOI: 10.1007/978-1-4614-4978-2_2.

INO (2019). *BIOMIMIC OPTICAL PHANTOMS*. URL: https://inostorage.blob.core.windows.net/media/1870/fichetechnique-mkt-2019-bio-01.pdf (visited on 05/31/2019).

Jacques, S. L. (1992). "How tissue optics affect dosimetry for photochemical, photothermal, and photomechanical mechanisms of laser-tissue interaction." In: *Recent Advances in the Uses of Light in Physics, Chemistry, Engineering, and Medicine*. Ed. by D. L. Akins and R. R. Alfano, p. 316. ISBN: 0819407305. DOI: 10.1117/12.56713.

— (1993). "Role of tissue optics and pulse duration on tissue effects during high-power laser irradiation." In: *Applied Optics* 32.13, p. 2447. DOI: 10.1364/AO.32.002447.

Jacques, S. L. (1996). "Origins of tissue optical properties in the UVA, visible, and NIR regions." In: *OSA TOPS on Advances in Optical Imaging and Photon Migration* January 1996.

Jacques, S. L. (2013). "Optical properties of biological tissues: a review." In: *Physics in Medicine and Biology* 58.11, R37–R61. DOI: 10.1088/0031-9155/58/11/R37.

Jacques Steven L. *Biomedical optics: irradiance versus fluence rate*. URL: https://omlc.org/news/sep05/irradiancemovie.html (visited on 11/03/2021).

Jakub, M., K. Kamil, J. Mesicek, and K. Kuca (2018). "Summary of numerical analyses for therapeutic uses of laser-activated gold nanoparticles." In: *International Journal of Hyperthermia* 34.8, pp. 1255–1264. DOI: 10.1080/02656736.2018.1440016.

Jaque, D., L. Martínez Maestro, B. Del Rosal, P. Haro-Gonzalez, A. Benayas, J. L. Plaza, E. Martín Rodríguez, and J. García Solé (2014). "Nanoparticles for photothermal therapies." In: *Nanoscale* 6.16, pp. 9494–9530. DOI: 10.1039/c4nr00708e. arXiv: arXiv:1503.01668v2.

Jaunich, M., S. Raje, K. Kim, K. Mitra, and Z. Guo (2008). "Bio-heat transfer analysis during short pulse laser irradiation of tissues." In: *International Journal of Heat and Mass Transfer* 51.23-24, pp. 5511–5521. DOI: 10.1016/j.ijheatmasstransfer.2008.04.033.

Jaywant, S. M., B. C. Wilson, M. S. Patterson, L. D. Lilge, T. J. Flotte, J. Woolsey, and C. McCulloch (1993). "Temperature-dependent changes in the optical absorption and scattering spectra of tissues: correlation with ultrastructure." In: *Laser-Tissue Interaction IV* 1882.July 2015, p. 218. DOI: 10.1117/12.148080.

Jiang, H., N. V. Iftimia, Y. Xu, J. A. Eggert, L. L. Fajardo, and K. L. Klove (2002). "Near-infrared optical imaging of the breast with model-based reconstruction." In: *Academic Radiology* 9.2, pp. 186–194. DOI: 10.1016/S1076-6332(03)80169-1.

Kim, A. and B. C. Wilson (2010). "Measurement of Ex Vivo and In Vivo Tissue Optical Properties: Methods and Theories." In: *Optical-Thermal Response of Laser-Irradiated*

Tissue. Dordrecht: Springer Netherlands, pp. 267–319. DOI: 10.1007/978-90-481-8831-4_8.

Lai, P., X. Xu, and L. V. Wang (2014). "Dependence of optical scattering from Intralipid in gelatin-gel based tissue-mimicking phantoms on mixing temperature and time." In: *Journal of Biomedical Optics* 19.3, p. 035002. DOI: 10.1117/1.jbo.19.3.035002. arXiv: arXiv:1011.1669v3.

Lamien, B. (2015). "Problema de Estimativa de Estado no Tratamento de Câncer Por Hipertermia Com Aquecimento Por Laser Diodo na Faixa do infravermelho Próximo." Doctoral dissertation. UFRJ.

Liu, G., Z. Chen, and C. Zhongping (2013). *Optical Methods and Instrumentation in Brain Imaging and Therapy*. Chapter 7, pp. 157–172. ISBN: 978-1-4614-4977-5. DOI: 10.1007/978-1-4614-4978-2.

Lopes, A., A. Gabriel, J. Machado, P. Ribeiro, R. Gomes, J. J.M. P. Coelho, C. O. Silva, C. P. Reis, J. P. Santos, and P. Vieira (2016). "Multiple source phototherapy in breast cancer: A viability study." In: *BIODEVICES 2016 - 9th International Conference on Biomedical Electronics and Devices, Proceedings; Part of 9th International Joint Conference on Biomedical Engineering Systems and Technologies, BIOSTEC 2016* 1.Biostec, pp. 247–250. DOI: 10.5220/0005794902470250.

Lopes, A., R. Gomes, M. Castiñeras, J. M. P. Coelho, J. P. Santos, P. Vieira, P. Santos, R. Gomes, and M. Casti (2019). "Probing deep tissues with laser-induced thermotherapy using near-infrared light." In: *Lasers in Medical Science*. DOI: 10.1007/s10103-019-02768-7.

Malhotra, G. K., X. Zhao, H. Band, and V. Band (2010). "Histological, molecular and functional subtypes of breast cancers." In: *Cancer Biology & Therapy* 10.10, pp. 955–960. DOI: 10.4161/cbt.10.10.13879.

Manns, F., P. J. Milne, X. Gonzalez-Cirre, D. B. Denham, J.-M. Parel, and D. S. Robinson (1998). "In Situ temperature measurements with thermocouple probes during laser interstitial thermotherapy (LITT): Quantification and correction of a measurement artifact." In: *Lasers in Surgery and Medicine* 23.2, pp. 94–103. DOI: 10.1002/(SICI)1096-9101(1998)23:2<94::AID-LSM7>3.0.CO;2-Q.

Marchesini, R, A Bertoni, S Andreola, E Melloni, and a. E. Sichirollo (1989). "Extinction and absorption coefficients and scattering phase functions of human tissues in vitro." In: *Applied optics* 28.12, pp. 2318–24. DOI: 10.1364/AO.28.002318.

McKenzie, A. L. (1990). "Physics of thermal processes in laser-tissue interaction." In: *Physics in Medicine and Biology* 35.9, pp. 1175–1210. DOI: 10.1088/0031-9155/35/9/001.

Metwally, M. K., S. H. El-Gohary, S. M. Han, K. M. Byun, and T. S. Kim (2015). "Influence of the anisotropic mechanical properties of the breast cancer on photoacoustic imaging." In: *Proceedings of the 7th Cairo International Biomedical Engineering Conference, CIBEC 2014* September, pp. 34–38. DOI: 10.1109/CIBEC.2014.7020958.

Miaskowski, A. and M. Subramanian (2019). "Numerical model for magnetic fluid hyperthermia in a realistic breast phantom: Calorimetric calibration and treatment planning." In: *International Journal of Molecular Sciences* 20.18. DOI: 10.3390/ijms20184644.

Minkowycz, W., EM.Sparrow, and J.P.Abraham (2009). *Advances in numerical heat transfer Volume 3*. Vol. 3, p. 379. ISBN: 9781420095210.

Mukundakrishnan, K, P Ayyaswamy, and J Baish (2009). "Numerical Models of Blood Flow Effects in Biological Tissues." In: pp. 29–74. DOI: 10.1201/9781420095227.ch2.

Murbach, M., E. Neufeld, M. Capstick, W. Kainz, D. O. Brunner, T. Samaras, K. P. Pruessmann, and N. Kuster (2014). "Thermal Tissue Damage Model Analyzed for Different Whole-Body SAR and Scan Durations for Standard MR Body Coils." In: *Magnetic Resonance in Medicine* 71.1, pp. 421–431. DOI: 10.1002/mrm.24671.

Niemz, M. H. (1996). *Laser-Tissue Interactions*. Cham: Springer International Publishing. ISBN: 978-3-030-11916-4. DOI: 10.1007/978-3-030-11917-1.

Nikishkov, G. P. (2004). *Lecture notes on the "Introduction to the Finite Element Method"*. Tech. rep.

Organization, W. H. (2015). *Women's health*. URL: https://www.who.int/cancer/prevention/diagnosis-screening/breast-cancer/en/ (visited on 05/02/2019).

Paschotta, R. (2008). *Encyclopedia of Laser Physics and Technology*. URL: https://www.rp-photonics.com/encyclopedia.html (visited on 12/01/2019).

Patterson, M. S., B. C. Wilson, and D. R. Wyman (1991a). "The Propagation of Optical Radiation in Tissue I. Models of Radiation Transport and their Application." In: *Lasers in Medical Science* 6.2, pp. 155–168. DOI: 10.1007/BF02032543.

Patterson, M. S., B. C. Wilson, and D. R. Wyman (1991b). "The propagation of optical radiation in tissue. II: Optical properties of tissues and resulting fluence distributions." In: *Lasers in Medical Science* 6.4, pp. 379–390. DOI: 10.1007/BF02042460.

Pennes, H. H. (1998). "Analysis of tissue and arterial blood temperatures in the resting human forearm. 1948." In: *Journal of applied physiology (Bethesda, Md. : 1985)* 85, pp. 5–34. DOI: 9714612. arXiv: arXiv:1011.1669v3.

Pogue, B. W. and M. S. Patterson (2006). "Review of tissue simulating phantoms for optical spectroscopy, imaging and dosimetry." In: *Journal of Biomedical Optics* 11.4, p. 041102. DOI: 10.1117/1.2335429. arXiv: arXiv:1011.1669v3.

Prahl, S. A. (1988). "Light transport in tissue." In: *Applied optics* 28.12, pp. 2216–2222. DOI: 10.1364/AO.28.002216.

Qin, Z. and J. C. Bischof (2012). "Thermophysical and biological responses of gold nanoparticle laser heating." In: *Chemical Society Reviews* 41.3, pp. 1191–1217. DOI: 10.1039/c1cs15184c.

Reynoso, F. J. (2011). "Modelling of near infrared laser-mediaed plasmonic heating with optically tunable gold nanoparticles for thermal therapy." Doctoral dissertation.

Reynoso, F. J., C.-d. D. Lee, S.-k. K. Cheong, and S. H. Cho (2013). "Implementation of a multisource model for gold nanoparticle-mediated plasmonic heating with near-infrared laser by the finite element method." In: *Medical Physics* 40.7, p. 073301. DOI: 10.1118/1.4808361.

Rowe, P. I., R. Künnemeyer, A. McGlone, S. Talele, P. Martinsen, and R. Oliver (2013). "Thermal stability of intralipid optical phantoms." In: *Applied Spectroscopy* 67.8, pp. 993–996. DOI: 10.1366/12-06971.

Sajjadi, A. Y., K. Mitra, and Z. Guo (2013). "THERMAL ANALYSIS AND EXPERIMENTS OF LASER–TISSUE INTERACTIONS: A REVIEW." In: *Heat Transfer Research* 44.3-4, pp. 345–388. DOI: 10.1615/HeatTransRes.2012006425.

Schweiger, M., S. R. Arridge, and D. T. Delpy (1993). "Application of the finite-element method for the forward and inverse models in optical tomography." In: *Journal of Mathematical Imaging and Vision*. DOI: 10.1007/BF01248356.

Schweiger, M., S. Arridge, M. Schweiger, and S. Arridge (2014). "The Toast++ software suite for forward and inverse modeling in optical tomography." In: *Journal of biomedical optics* 19.4, p. 040801. DOI: 10.1117/1.JBO.19.4.040801.

Sheng, W., S. He, W. J. Seare, and A. Almutairi (2017). "Review of the progress toward achieving heat confinement—the holy grail of photothermal therapy." In: *Journal of Biomedical Optics* 22.8, p. 080901. DOI: 10.1117/1.JBO.22.8.080901.

Silva, C. O., P. Rijo, J. Molpeceres, L. Ascensão, A. Roberto, A. S. Fernandes, R. Gomes, J. M. Pinto Coelho, A. Gabriel, P. Vieira, and C. P. Reis (2016). "Bioproduction of gold nanoparticles for photothermal therapy." In: *Therapeutic delivery* 7.5, pp. 287–304. DOI: 10.4155/tde-2015-0011.

Soni, S., H. Tyagi, R. a. Taylor, and A. Kumar (2013). "Role of optical coefficients and healthy tissue-sparing characteristics in gold nanorod-assisted thermal therapy." In: *International journal of hyperthermia : the official journal of European Society for Hyperthermic Oncology, North American Hyperthermia Group* 29.1, pp. 87–97. DOI: 10.3109/02656736.2012.753162.

Sturesson, C. (1998). *Medical Laser-Induced Thermotherapy*. Vol. thesis. October, pp. 1–84. ISBN: 9162831348.

Thomsen, S. and J. A. Pearce (2010). "Thermal damage and rate processes in biologic tissues." In: *Optical-Thermal Response of Laser-Irradiated Tissue*. Dordrecht: Springer Netherlands, pp. 487–549. ISBN: 9789048188307. DOI: 10.1007/978-90-481-8831-4_13.

Valvano, J. W. (2010). "Tissue Thermal Properties and Perfusion." In: *Optical-Thermal Response of Laser-Irradiated Tissue*. Dordrecht: Springer Netherlands, pp. 455–485. DOI: 10.1007/978-90-481-8831-4_12.

Walsh, J. T. (2010). "Basic Interactions of Light with Tissue." In: *Optical-Thermal Response of Laser-Irradiated Tissue*. Dordrecht: Springer Netherlands, pp. 13–26. DOI: 10.1007/978-90-481-8831-4_2.

Wang, L., S. L. Jacques, and L. Zheng (1995). "MCML—Monte Carlo modeling of light transport in multi-layered tissues." In: *Computer Methods and Programs in Biomedicine* 47.2, pp. 131–146. DOI: 10.1016/0169-2607(95)01640-F.

Welch, A. J. (1984). "The Thermal Response of Laser Irradiated Tissue." In: *IEEE Journal of Quantum Electronics* 20.12, pp. 1471–1481. DOI: 10.1109/JQE.1984.1072339.

Welch, A. J. and M. J. van Gemert (2010). "Overview of Optical and Thermal Laser-Tissue Interaction and Nomenclature." In: *Optical-Thermal Response of Laser-Irradiated Tissue*. Dordrecht: Springer Netherlands, pp. 3–11. DOI: 10.1007/978-90-481-8831-4_1.

Welch, A. J. and M. J. Van Gemert (2011). *Optical-thermal response of laser-irradiated tissue*. Vol. 2. Dordrecht: Springer, pp. 1–958. ISBN: 9789048188307. DOI: 10.1007/978-90-481-8831-4.

Welch, A. J., M. J. van Gemert, and W. M. Star (2010). "Definitions and Overview of Tissue Optics." In: *Optical-Thermal Response of Laser-Irradiated Tissue*. Dordrecht: Springer Netherlands, pp. 27–64. DOI: 10.1007/978-90-481-8831-4_3.

Xia, J., J. Yao, and L. H. V. Wang (2014). "PHOTOACOUSTIC TOMOGRAPHY: PRINCIPLES AND ADVANCES (Invited Review)." In: *Progress In Electromagnetics Research* 147, pp. 1–22. DOI: 10.2528/PIER14032303.

Yao, R., X. Intes, and Q. Fang (2016). "Generalized mesh-based Monte Carlo for wide-field illumination and detection via mesh retessellation." In: *Biomedical Optics Express* 7.1, p. 171. DOI: 10.1364/BOE.7.000171.

You, J. S., C. K. Hayakawa, and V. Venugopalan (2005). "Frequency domain photon migration in the δ-P1 approximation: Analysis of ballistic, transport, and diffuse regimes." In: *Physical Review E - Statistical, Nonlinear, and Soft Matter Physics*. DOI: 10.1103/PhysRevE.72.021903.

Zhang, M., Z. Che, J. Chen, H. Zhao, L. Yang, Z. Zhong, and J. Lu (2011). "Experimental determination of thermal conductivity of water-agar gel at different concentrations and temperatures." In: *Journal of Chemical and Engineering Data* 56.4, pp. 859–864. DOI: 10.1021/je100570h.

Zhang, X. (2014). "Instrumentation in Diffuse Optical Imaging." In: *Photonics* 1.1, pp. 9–32. DOI: 10.3390/photonics1010009. arXiv: NIHMS150003.

Appendix 1 - Instrumentation

A.1 Laser Characterisation

The laser diode considered in all of the experiments is a JDSU L4-2495-003. The vendor's software controlled this laser, and it fed the laser electrical current from a minimum threshold current of 1 A up to 5.5 A. The relation between current and laser power is shown in figure A.1.

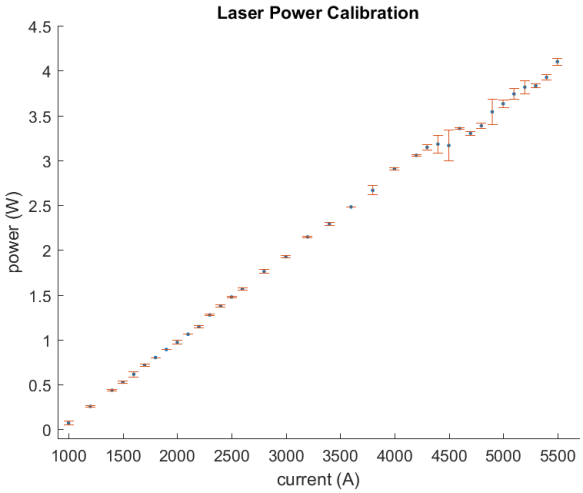

Figure A.1: Laser diode power as a function of current.

The laser power values were taken from a digital laser power meter. The error bars represent maximum and minimum values in a 30-second acquisition and the points their mean value. The photothermal experiments done in this work used laser powers between 1∼2 W.

The laser beam profile is shown in figure A.2. The laser intensity was set at 1W, coupled with the collimating lens, and several neutral density filters were used not to saturate the device. The full width at half a maximum of 7.2 mm was determined by the laser beam analyser's software (Spiricon, LBA-700).

Light inside a multimode fibre can be separated into many rays dependent on the angles and positions when entering the fibre[1,2]. During light propagation in the fibre, different rays will reflect at different positions at the core/cladding interface and will consequently exit a plane-cut fibre at different positions. With a uniform refractive index of the fibre's core, the spatial distribution at the fibre exit will also be uniform. However, at distances much greater than the fibre diameter, the intensity distribution will be Gaussian[3,4] (Sturesson 1998, p. 35). Keep in mind that an FWHM beam diameter is approximately 1.18 times the Gaussian beam radius (1/e2 value).

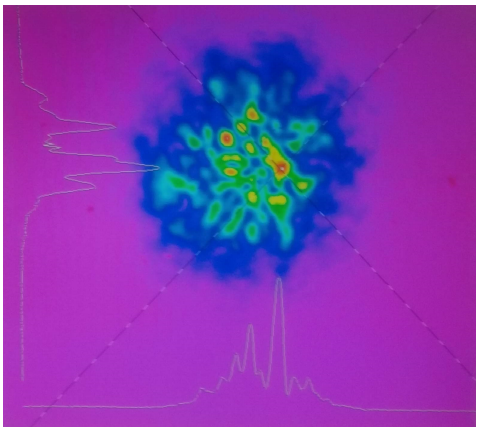

Figure A.2: Laser beam profile at 1W of laser power.

The laser line shape is presented in figure A.3. The measured values are shown using a spectrometer (Avantes, Avaspec 2048) coupled with a collimating lens (Avantes, COL-UV/VIS) at 1W of laser power. The maximum value of this distribution is at λ_{max} = 808.5 nm.

A.2 Thermocouple Characterisation

In all of the photothermal experiments, it was used a type K thermocouple (Labfacility, Z2-T-1M) and a thermocouple converter (Seneca K109TC) connected to a LabVIEW® interface.

The LabVIEW code is shown in figure A.4. The temperature readout considered the DAQmx assistant, which showed the already translated by the thermocouple converter

[1] https://www.rp-photonics.com/beam_profilers.html
[2] https://www.rp-photonics.com/multimode_beams.html
[3] https://www.ophiropt.com/laser–measurement/power-density-calculator
[4] https://www.rp-photonics.com/beam_radius.html

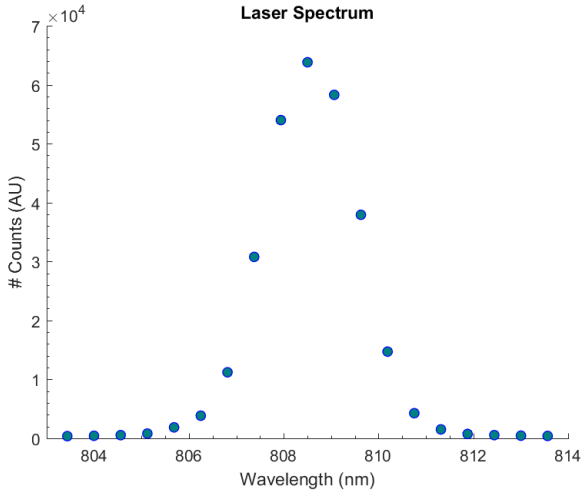

Figure A.3: Laser diode spectrum. In points are presented the measured values.

from the typical small electrical signal to one between 0 and 10V, where 0 and 10 represented a linear relationship between the maximum and minimum values that the thermocouple could handle. The rate readout was set to the maximum of the thermocouple capacity.

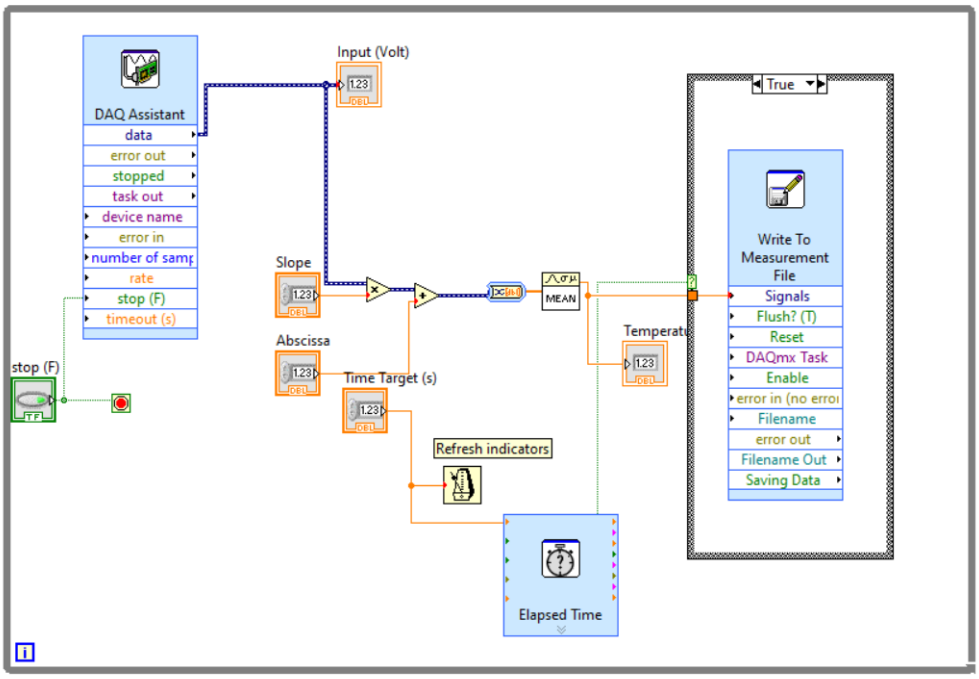

Figure A.4: This image shows the LabVIEW vi developed to measure the temperature with type K thermocouple.

A calibrated thermocouple (Fluke 52[5]) was used to calibrate the Labfacility thermocouple and a glass of boiling water. The two thermocouples were than immersed in the water glued with duct tape. Some cold water was added to the hot water to hurry the cooling down process. These two temperatures from both thermocouples are presented in figure A.5 as a function of time.

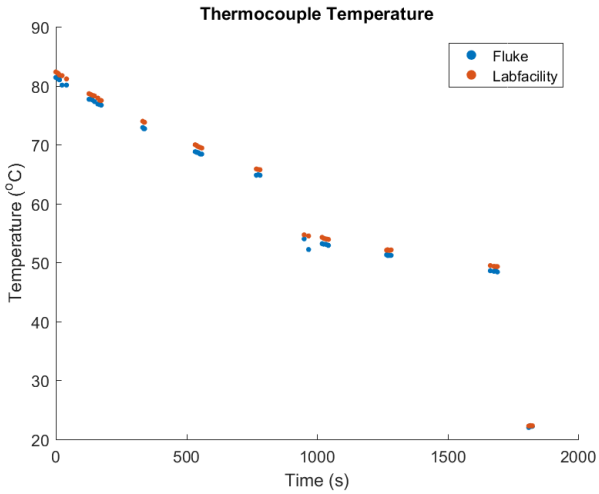

Figure A.5: Temperature values taken from two type K thermocouple converters, a Fluke 52 (calibrated) and the Labfacility Z2-T-1M (uncalibrated).

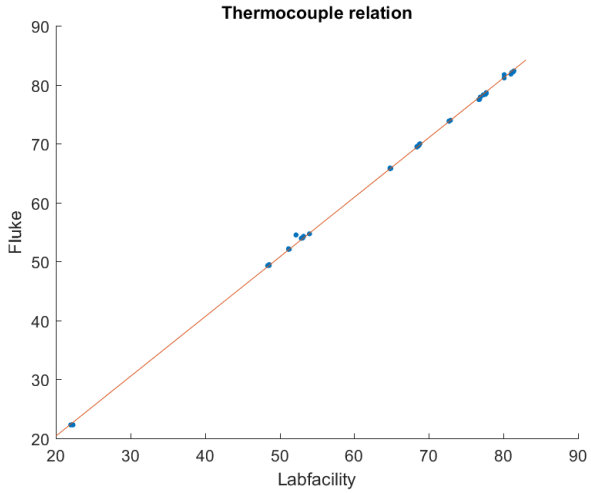

Figure A.6: Relation between the temperature from the two thermocouples shown in points. The line represents a linear fit between the two, which was added to the LabVIEW vi.

Both temperatures were plotted in figure A.6, and a linear fit was performed to the two $\hat{T_{Labfacility}} = 1.03x + 0.106$, with $R^2 = 0.9997$. This relation was then considered as

[5]This is a digital thermocouple and cannot be connected to a personal computer and save data to a file.

input in the vi in the 'slope' and 'abscissa' parameters, as shown in figure A.4. The time target represents the rate of output which was 1 second.

Appendix B

Appendix 2 - Code

This appendix shows the code used in chapter 4, based on the numerical protocol shown in figure 3.3 and discussed in section 3.3. The files to perform all of these studies can be found here.

B.1 Gmsh

To build a meshed sample, first one needs to start to define its geometry by specifying starting points, then contours, areas and volumes.

```
1
2  sec=60;  //half the width of the cube
3  len=40;  //half of the height of the cube
4  size1=4; //Number of nodes in the irradiated cube face
5  size2=1; //Number of nodes in the other cube faces
6  r=8;  //radius of GNP cylinder
7
8  // Defining cube vertices with higher density of nodes
9  // in the irradiated cube's face
10 Point(1) = {-sec/2,-sec/2,-len/2,size1};
11 Point(2) = { sec/2,-sec/2,-len/2,size1};
12 Point(3) = {-sec/2, sec/2,-len/2,size1};
13 Point(4) = { sec/2, sec/2,-len/2,size1};
14 Point(5) = {-sec/2,-sec/2, len/2,size2};
15 Point(6) = { sec/2,-sec/2, len/2,size2};
16 Point(7) = {-sec/2, sec/2, len/2,size2};
17 Point(8) = { sec/2, sec/2, len/2,size2};
18
19 // Defining high absorption cylinder points at 4mm from
20 // the cubes irradiated surface
```

```
Point(9) = {0, 0, len/2-5, size2};
Point(10) = {r, 0, len/2-5, size2};
Point(11) = {0, r, len/2-5, size2};
Point(12) ={-r, 0, len/2-5, size2};
Point(13) ={ 0,-r, len/2-5, size2};
Point(14) = {0, 0, len/2-10, size2};
Point(15) = {r, 0, len/2-10, size2};
Point(16) = {0, r, len/2-10, size2};
Point(17) ={-r, 0, len/2-10, size2};
Point(18) = {0,-r, len/2-10, size2};

// Defining cube's edges
Line(1) = {6, 8};
Line(2) = {8, 4};
Line(3) = {4, 2};
Line(4) = {2, 6};
Line(5) = {6, 5};
Line(6) = {5, 1};
Line(7) = {1, 2};
Line(8) = {1, 3};
Line(9) = {3, 4};
Line(10) = {5, 7};
Line(11) = {7, 8};
Line(12) = {7, 3};

// Defining cylinder's circled contours
Circle(13) = {16, 14, 15};
Circle(14) = {15, 14, 18};
Circle(15) = {18, 14, 17};
Circle(16) = {17, 14, 16};
Circle(17) = {11, 9, 10};
Circle(18) = {10, 9, 13};
Circle(19) = {13, 9, 12};
Circle(20) = {12, 9, 11};

// Defining cylinder's line contours
Line(21) = {14, 9};
Line(22) = {13, 18};
Line(23) = {17, 12};
Line(24) = {16, 11};
Line(25) = {15, 10};

// Defining cube's partial areas from segmented lines
Line Loop(1) = {19, 20, 17, 18};
Line Loop(2) = {16, 13, 14, 15};
Line Loop(3) = {15, 23, -19, 22};
Line Loop(4) = {22, -14, 25, 18};
Line Loop(5) = {17, -25, -13, 24};
Line Loop(6) = {16, 24, -20, -23};

```

```
71 // Defining cylinder's partial areas from segmented lines and arcs
72 Line Loop(7) = {1, -11, -10, -5};
73 Line Loop(8) = {9, 3, -7, 8};
74 Line Loop(9) = {7, 4, 5, 6};
75 Line Loop(10) = {11, 2, -9, -12};
76 Line Loop(11) = {2, 3, 4, 1};
77 Line Loop(12) = {6, 8, -12, -10};
78
79 // Defining cubes surfaces from the element areas
80 Plane Surface(1) = {1};
81 Plane Surface(2) = {2};
82 Surface(3) = {3};
83 Surface(4) = {4};
84 Surface(5) = {5};
85 Surface(6) = {6};
86
87 // Defining cylinders surfaces from the element areas
88 Plane Surface(7) = {7};
89 Plane Surface(8) = {8};
90 Plane Surface(9) = {9};
91 Plane Surface(10) = {10};
92 Plane Surface(11) = {11};
93 Plane Surface(12) = {12};
94
95 // Defining cylinder and cube as separate volumes
96 Surface Loop(1) = {2, 6, 5, 1, 3, 4};
97 Surface Loop(2) = {7, 11, 10, 8, 9, 12};
98 Volume(1) = {1};
99 Volume(2) = {1, 2};
```

run these commands in the terminal to get the mesh files:

`gmsh -3 Het-cube.geo -o Het-cube.msh`

`gmsh -3 Het-cube.geo -o Het-cube.stl`

The first file will be used as an input in MATLAB, while the second file will be used as input in COMSOL Multiphysics®.

B.2 TOAST++ & Meshed-Monte Carlo

```

% clear all;

mesh = toastMesh('Cubo-het.msh','gmsh');
[node,elem] = mesh.Data;

%mesh.Display;

%% Identify and label the different geometric volumes

ne = mesh.ElementCount;
nn = mesh.NodeCount;
regidx = mesh.Region;
regno = unique(regidx);
GNP = find(regidx == regno(1));
cubo = find(regidx == regno(2));

%% Define targets optical properties

% Agar gel properties
refind = 1.33; % refractive index
mua_Gel = 0.002; % background absorption [1/mm]
musp_Gel = 0.03; % background reduced scattering [1/mm]
g_Gel = 0.9;
mus_Gel = musp_Gel/(1-g_Gel);

% Gold nanoparticles properties
mua_GNP = 0.031; % background absorption [1/mm]
musp_GNP = 0.029;
mus_GNP = musp_GNP/(1-g_Gel);

sigma=3.07;

refe = ones(ne,1)*refind;
muae = ones(ne,1)*mua_Gel;
muspe = ones(ne,1)*musp_Gel;
muae(GNP) = mua_GNP;
muspe(GNP) = musp_GNP;

m_calc;
refn = ones(nn,1)*refind;
muan = ones(nn,1)*mua_Gel;
muspn = ones(nn,1)*musp_Gel;
muan(cylz)= mua_GNP;
muspn(cylz)=musp_GNP;


%% Define source and measurement geometry
```

```
49
50 mesh.SetQM(sourcepos,detectorpos);
51 qvec = mesh.Qvec('Neumann','Gaussian',sigma);
52 mvec = mesh.Mvec('Gaussian',7,0);
53
54 K = dotSysmat(mesh,muae,muspe,refe,0,'EL');
55 Phi = K\qvec;
56
57 vhs_toast = Phi .* muan;
58
59 figure;
60 plotmesh([node,full(Phi)],elem,'y=0','linestyle','none');
61 hold on;
62 view(0,0);
63 xlabel('X␣[mm]'); ylabel('Y␣[mm]');
64
65
66 %%%%%%%%%%%%%%%%%%%%%%%%%%%%%%%
67 %%%%%%%%%%%%%%%%%%%%%%%%%%%%%%%
68
69 %% Loading the Mesh and MMC variables
70
71 % Source related properties
72 %cfg.srctype='pencil';
73 cfg.srctype='gaussian';
74 cfg.srcpos=[0,0,25];
75 cfg.srcdir=[0,0,-1];
76 cfg.srcparam1=[sigma 0 0 0];
77 cfg.srcparam2=[0 0 0 0];
78
79
80 % cfg options
81 cfg.prop=[0 0 1 1;
82 mua_Gel mus_Gel g_Gel refind;
83 mua_GNP mus_GNP g_Gel refind];
84 cfg.nphoton=1e6;
85 cfg.tstart=0;
86 cfg.tstep=1e-9;
87 cfg.tend=1e-8;
88 cfg.debuglevel='TP';
89 %cfg.seed=27182818;
90 cfg.outputtype='flux';
91 cfg.isnormalized=1;
92
93 %% SOURCE PROPERTIES
94
95 elemprop = mesh.Region;
96
97 srcdef=struct('srctype',cfg.srctype,'srcpos',cfg.srcpos,'srcdir',...
98 cfg.srcdir,'srcparam1',cfg.srcparam1,'srcparam2',cfg.srcparam2);
```

```
99  [cfg.node,cfg.elem] = mmcaddsrc(node,[elem elemprop],...
100 mmcsrcdomain(srcdef,[min(node);max(node)]));
101
102 cfg.elemprop=cfg.elem(:,5);
103 cfg.elem=cfg.elem(:,1:4);
104
105 newcfg=mmclab(cfg,'prep');
106 % preprocessing of the mesh to get the missing fields
107 flux=mmclab(newcfg); % initial simulation
108
109 phi=sum(flux.data,2)*cfg.tstep;
110
111 VHS_mmc = phi(1:nn,:).*muan(1:nn,:);
112 figure;
113 plotmesh([node,phi(1:nn,:)],elem,'y=0','linestyle','none');
114 hold on;
115 view(0,0);
116
117 %%%%%%%%%%%%%%%%%%%%%%%%%%%%%%%%
118 %%%%%%%%%%%%%%%%%%%%%%%%%%%%%%%%
119
120 %% Save to file
121
122
123 file_tmp = sprintf('./Exp2_toast.txt');
124 fileID = fopen(file_tmp,'w');
125
126 fprintf(fileID,'%%Coordinates\n');
127 for i = 1:nn
128 tmp = node(i,:);
129 fprintf(fileID,'%f\t%f\t%f\n',tmp(1), tmp(2), tmp(3));
130 end
131
132 fprintf(fileID,'%%Elements\n');
133 for i = 1:ne
134 fprintf(fileID,'%d\t%d\t%d\t%d\n',elem(i,1),elem(i,2),...
135 elem(i,3),elem(i,4));
136 end
137
138 fprintf(fileID,'%%Data (Abs)\n');
139 for i = 1:nn
140 fprintf(fileID,'%e\n',full(vhs_toast(i)));
141 end
142 fclose(fileID);
143
144 %%%%%%%
145
146 file_tmp = sprintf('./Exp2_mmc.txt');
147 fileID = fopen(file_tmp,'w');
148
```

```
fprintf(fileID,'%%Coordinates\n');
for i = 1:nn
tmp = node(i,:);
fprintf(fileID,'%f\t%f\t%f\n',tmp(1), tmp(2), tmp(3));
end

fprintf(fileID,'%%Elements\n');
for i = 1:ne
fprintf(fileID,'%d\t%d\t%d\t%d\n',elem(i,1),elem(i,2),...
elem(i,3),elem(i,4));
end

fprintf(fileID,'%%Data (Abs)\n');
for i = 1:nn
fprintf(fileID,'%e\n',full(VHS_mmc(i)));
end
fclose(fileID);
```